USGS
science for a changing world

Field-Trip Guide to Mount St. Helens, Washington—An Overview of the Eruptive History and Petrology, Tephra Deposits, 1980 Pyroclastic Density Current Deposits, and the Crater

Scientific Investigations Report 2017–5022–D

U.S. Department of the Interior
U.S. Geological Survey

Cover: Oblique aerial photograph of the north flank of Mount St. Helens, taken on June 29, 2005. White massif in center of crater is a lava spine from the ongoing eruption. Mount Hood is visible in distance to the south-southeast. Photograph by John Pallister.

Field-Trip Guide to Mount St. Helens, Washington—An Overview of the Eruptive History and Petrology, Tephra Deposits, 1980 Pyroclastic Density Current Deposits, and the Crater

By John S. Pallister, Michael A. Clynne, Heather M. Wright, Alexa R. Van Eaton, James W. Vallance, David R. Sherrod, and B. Peter Kokelaar

Scientific Investigations Report 2017–5022–D

U.S. Department of the Interior
U.S. Geological Survey

U.S. Department of the Interior
RYAN K. ZINKE, Secretary

U.S. Geological Survey
William H. Werkheiser, Acting Director

U.S. Geological Survey, Reston, Virginia: 2017

Suggested citation:
Pallister, J.S., Clynne, M.A., Wright, H.M., Van Eaton, A.R., Vallance, J.W., Sherrod, D.R., and Kokelaar, B.P., 2017, Field-trip guide to Mount St. Helens, Washington—An overview of the eruptive history and petrology, tephra deposits, 1980 pyroclastic density current deposits, and the crater: U.S. Geological Survey Scientific Investigations Report 2017–5022–D, 65 p., https://doi.org/10.3133/sir20175022D.

ISSN 2328-0328 (online)

Preface

The North American Cordillera is home to a greater diversity of volcanic provinces than any comparably sized region in the world. The interplay between changing plate-margin interactions, tectonic complexity, intra-crustal magma differentiation, and mantle melting have resulted in a wealth of volcanic landscapes. Field trips in this series visit many of these landscapes, including (1) active subduction-related arc volcanoes in the Cascade Range; (2) flood basalts of the Columbia Plateau; (3) bimodal volcanism of the Snake River Plain-Yellowstone volcanic system; (4) some of the world's largest known ignimbrites from southern Utah, central Colorado, and northern Nevada; (5) extension-related volcanism in the Rio Grande Rift and Basin and Range Province; and (6) the spectacular eastern Sierra Nevada featuring Long Valley Caldera and the iconic Bishop Tuff. Some of the field trips focus on volcanic eruptive and emplacement processes, calling attention to the fact that the western United States provides opportunities to examine a wide range of volcanological phenomena at many scales.

The 2017 Scientific Assembly of the International Association of Volcanology and Chemistry of the Earth's Interior (IAVCEI) in Portland, Oregon, marks the first time that the U.S. volcanological community has hosted this quadrennial meeting since 1989, when it was held in Santa Fe, New Mexico. The 1989 field-trip guides are still widely used by students and professionals alike. This new set of field guides is similarly a legacy collection that summarizes decades of advances in our understanding of magmatic and tectonic processes of volcanic western North America.

The field of volcanology has flourished since the 1989 IAVCEI meeting, and it has profited from detailed field investigations coupled with emerging new analytical methods. Mapping has been enhanced by plentiful major- and trace-element whole-rock and mineral data, technical advances in radiometric dating and collection of isotopic data, GPS (Global Positioning System) advances, and the availability of lidar (light detection and ranging) imagery. Spectacularly effective microbeam instruments, geodetic and geophysical data collection and processing, paleomagnetic determinations, and modeling capabilities have combined with mapping to provide new information and insights over the past 30 years. The collective works of the international community have made it possible to prepare wholly new guides to areas across the western United States. These comprehensive field guides are available, in large part, because of enormous contributions from many experienced geologists who have devoted entire careers to their field areas. Early career scientists are carrying forward and refining their foundational work with impressive results.

Our hope is that future generations of scientists as well as the general public will use these field guides as introductions to these fascinating areas and will be enticed toward further exploration and field-based research.

Michael Dungan, University of Oregon
Judy Fierstein, U.S. Geological Survey
Cynthia Gardner, U.S. Geological Survey
Dennis Geist, National Science Foundation
Anita Grunder, Oregon State University
John Wolff, Washington State University

Field-trip committee, IAVCEI 2017

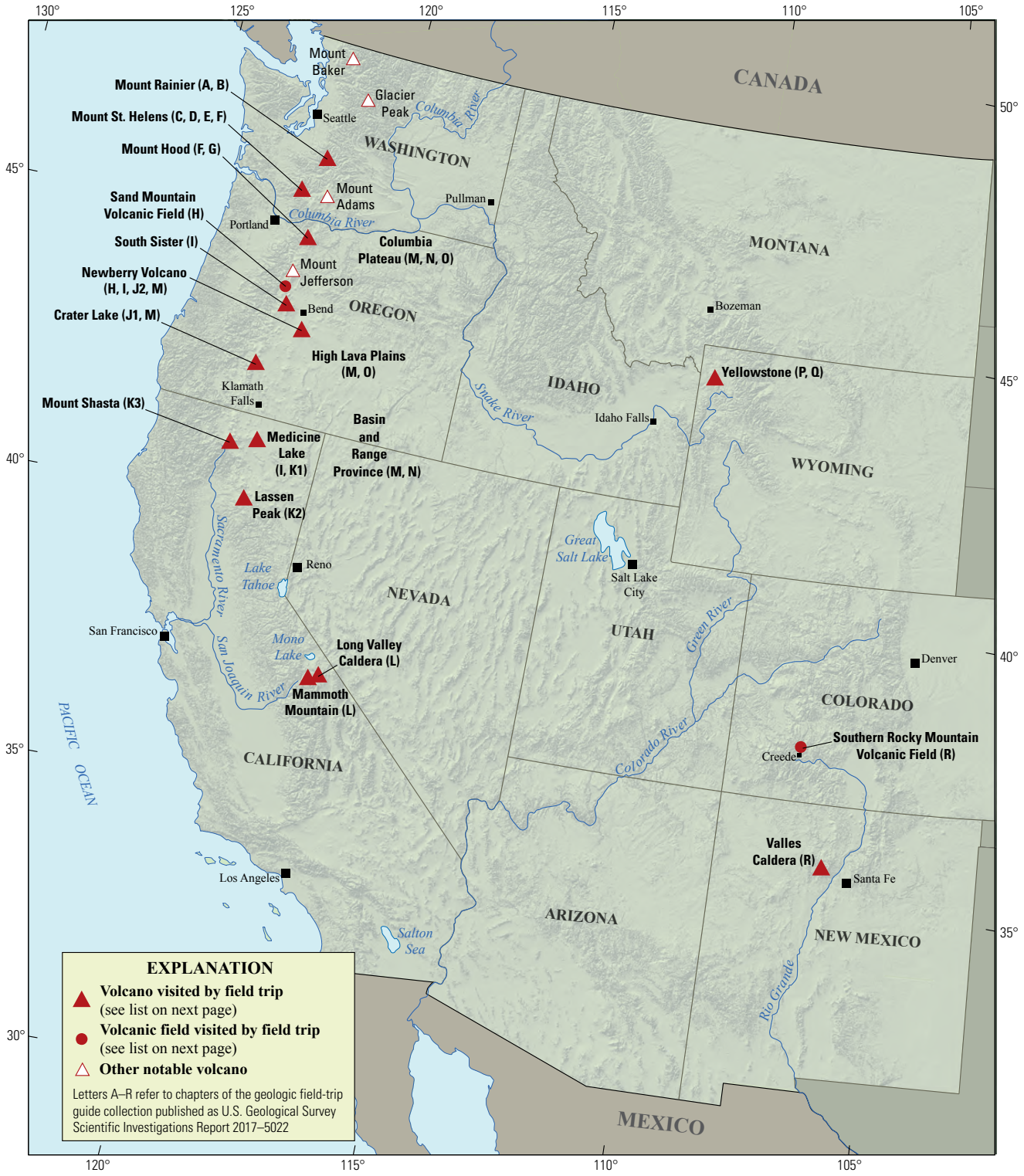

Map of the western United States showing volcanoes and volcanic fields visited by geologic field trips scheduled in conjunction with the 2017 meeting of the International Association of Volcanology and Chemistry of the Earth's Interior (IAVCEI) in Portland, Oregon, and available as chapters in U.S. Geological Survey Scientific Investigations Report 2017–5022. Shaded-relief base from U.S. Geological Survey National Elevation Dataset 30-meter digital elevation model data.

Chapter letter	Title
A	Field-Trip Guide to Volcanism and Its Interaction with Snow and Ice at Mount Rainier, Washington
B	Field-Trip Guide to Subaqueous Volcaniclastic Facies in the Ancestral Cascades Arc in Southern Washington State—The Ohanapecosh Formation and Wildcat Creek Beds
C	Field-Trip Guide for Exploring Pyroclastic Density Current Deposits from the May 18, 1980, Eruption of Mount St. Helens, Washington
D	Field-Trip Guide to Mount St. Helens, Washington—An overview of the Eruptive History and Petrology, Tephra Deposits, 1980 Pyroclastic Density Current Deposits, and the Crater
E	Field-Trip Guide to Mount St. Helens, Washington—Recent and Ancient Volcaniclastic Processes and Deposits
F	Geologic Field-Trip Guide of Volcaniclastic Sediments from Snow- and Ice-Capped Volcanoes—Mount St. Helens, Washington, and Mount Hood, Oregon
G	Field-Trip Guide to Mount Hood, Oregon, Highlighting Eruptive History and Hazards
H	Field-Trip Guide to Mafic Volcanism of the Cascade Range in Central Oregon—A Volcanic, Tectonic, Hydrologic, and Geomorphic Journey
I	Field-Trip Guide to Holocene Silicic Lava Flows and Domes at Newberry Volcano, Oregon, South Sister Volcano, Oregon, and Medicine Lake Volcano, California
J	Overview for Geologic Field-Trip Guides to Mount Mazama, Crater Lake Caldera, and Newberry Volcano, Oregon
J1	Geologic Field-Trip Guide to Mount Mazama and Crater Lake Caldera, Oregon
J2	Field-Trip Guide to the Geologic Highlights of Newberry Volcano, Oregon
K	Overview for Geologic Field-Trip Guides to Volcanoes of the Cascades Arc in northern California
K1	Geologic Field-Trip Guide to Medicine Lake Volcano, northern California, including Lava Beds National Monument
K2	Geologic Field-Trip Guide to the Lassen Segment of the Cascades Arc, northern California
K3	Geologic Field-Trip Guide to Mount Shasta Volcano, northern California
L	Geologic Field-Trip Guide to Long Valley Caldera, California
M	Field-Trip Guide to a Volcanic Transect of the Pacific Northwest
N	Field-Trip Guide to the Vents, Dikes, Stratigraphy, and Structure of the Columbia River Basalt Group, Eastern Oregon and Southeastern Washington
O	Field-Trip Guide to Flood Basalts, Associated Rhyolites, and Diverse Post-Plume Volcanism in Eastern Oregon
P	Field-Trip Guide to the Volcanic and Hydrothermal Landscape of Yellowstone Plateau, Montana and Wyoming
Q	Field-Trip Guide to the Petrology of Quaternary Volcanism on the Yellowstone Plateau, Idaho and Wyoming
R	Field-Trip Guide to Continental Arc to Rift Volcanism of the Southern Rocky Mountains—Southern Rocky Mountain, Taos Plateau, and Jemez Volcanic Fields of Southern Colorado and Northern New Mexico

Contributing Authors

Boise State University
Brittany D. Brand
Nicholas Pollock

Colgate University
Karen Harpp
Alison Koleszar

Durham University
Richard J. Brown

Eastern Oregon University
Mark L. Ferns

ETH Zurich
Olivier Bachmann

Georgia Institute of Technology
Josef Dufek

GNS Science, New Zealand
Natalia I. Deligne

Hamilton College
Richard M. Conrey

Massachusetts Institute of Technology
Timothy Grove

National Science Foundation
Dennis Geist (also with Colgate University and University of Idaho)

New Mexico Bureau of Geology and Mineral Resources
Paul W. Bauer
William C. McIntosh
Matthew J. Zimmerer

New Mexico State University
Emily R. Johnson

Northeastern University
Martin E. Ross

Oregon Department of Geology and Mineral Industries
William J. Burns
Lina Ma
Ian P. Madin
Jason D. McClaughry

Oregon State University
Adam J.R. Kent

Portland State University
Jonathan H. Fink (also with University of British Columbia)
Martin J. Streck
Ashley R. Streig

San Diego State University
Victor E. Camp

Smithsonian Institution
Lee Siebert

Universidad Nacional Autónoma de San Luis Potosi
Damiano Sarocchi

University of California, Davis
Kari M. Cooper

University of Liverpool
Peter B. Kokelaar

University of Northern Colorado
Steven W. Anderson

University of Oregon
Ilya N. Binderman
Michael A. Dungan
Daniele McKay (also with Oregon State University and Oregon State University, Cascades)

University of Portland
Kristin Sweeney

University of Tasmania
Martin Jutzeler
Jocelyn McPhie

University of Utah
Jamie Farrell

U.S. Army Corps of Engineers
Keith I. Kelson

U.S. Forest Service
Gordon E. Grant (also with Oregon State University

U.S. Geological Survey
Charles R. Bacon
Andrew T. Calvert
Christine F. Chan
Robert L. Christiansen
Michael A. Clynne
Michael A. Cosca
Julie M. Donnelly-Nolan
Benjamin J. Drenth
William C. Evans
Judy Fierstein
Cynthia A. Gardner
V.J.S. Grauch
Christopher J. Harpel
Wes Hildreth
Richard P. Hoblitt
Robert A. Jensen
Peter W. Lipman
Jacob B. Lowenstern
Jon J. Major
Seth C. Moran
Lisa A. Morgan
Leah E. Morgan
L.J. Patrick Muffler
James E. O'Connor
John S. Pallister
Thomas C. Pierson
Joel E. Robinson
Juliet Ryan-Davis
Kevin M. Scott
William E. Scott
Wayne (Pat) Shanks
David R. Sherrod
Thomas W. Sisson
Mark Evan Stelten
Weston Thelen
Ren A. Thompson
Kenzie J. Turner
James W. Vallance
Alexa R. Van Eaton
Jorge A. Vazquez
Richard B. Waitt
Heather M. Wright

U.S. Nuclear Regulatory Commission
Stephen Self (also with University of California, Berkeley)

Washington State University
Joseph R. Boro
Owen K. Neill
Stephen P. Reidel
John A. Wolff

Acknowledgments
Juliet Ryan-Davis and Kate Sullivan created the overview map, and Vivian Nguyen created the cover design for this collection of field-trip guide books. The field trip committee is grateful for their contributions.

Contents

Preface ... iii
Contributing Authors ... vi
Introduction ... 1
Tectonic and Physical Setting of Mount St. Helens ... 1
Eruptive History ... 4
Summary of 1980–1986 Eruptions ... 4
Volcanologic and Petrologic Insights from the 1980–1986 and 2004–2008 Lava Domes ... 7
Pre-1980 Eruptive History ... 9
Ape Canyon Stage ... 10
Cougar Stage ... 10
Swift Creek Stage ... 10
Spirit Lake Stage ... 11
Smith Creek Period ... 11
Pine Creek Period ... 11
Castle Creek Period ... 12
Sugar Bowl Period ... 12
Kalama Period ... 12
Goat Rocks Period ... 13
Modern Period ... 13
1980–1986 ... 13
1986–2004 ... 13
2004–2008 ... 14
Geochemistry and Petrology ... 16
Mineralogy ... 16
Inclusions ... 17
Major Element Composition ... 17
Trace-Element Composition ... 18
Basalts ... 19
Dacites ... 19
Andesites ... 19
Petrogenesis ... 19
Summary of Eruptive History, Geochemistry, and Petrology ... 23
Field Log ... 25
Day 0: Drive from Portland/Vancouver to Castle Rock, Washington ... 25
Day 1: 1980 Pyroclastic-Flow Deposits ... 25
Stops 4–8 Summary ... 28
Day 2: Blast, Tephra, and Stratigraphy ... 43
Sugar Bowl-Period Pyroclastic Density Current at Stop 12 ... 49
Petrologic Discussion Concerning the Stratigraphy at Stop 12 (Kalama-Period Magma Mixing) ... 49
Castle Creek Stratigraphy—A Discussion at Stop 13 ... 50
Composition and Petrology of the Late Castle Creek Period ... 51
Day 3: Crater Hike ... 55
References Cited ... 59

Figures

1. Index map showing the position of Mount St. Helens relative to the plate tectonic configuration of the northwestern United States and Canada 2
2. Map showing local tectonic setting of Mount St. Helens in an inferred pull-apart basin 3
3. Cross sections and photos of Mount St. Helens showing positions of Slide Blocks I, II, and III on May 18, 1980, and relative displacement of key compositional features 4
4. Diagram showing timeline of events and deposits from the May 18, 1980, eruption of Mount St. Helens 5
5. Photograph showing a vertical eruption column and pyroclastic density currents at 2:44 p.m. on May 18, 1980 6
6. Schematic cross sections of a stratovolcano, crustal magma reservoir, and conduit illustrating the effect of rapid versus slow ascent and gas loss on eruption explosivity 8
7. Plot of dated Ape Canyon-stage deposits 10
8. Plot of dated Cougar-stage deposits 11
9. Plot of dated Swift Creek-stage eruptions and deposits 11
10. Plot of dated Spirit Lake-stage eruptions and deposits 12
11. Aerial photograph of Mount St. Helens crater looking south toward the newly formed glacier at the base of the amphitheater wall 14
12. Oblique aerial photograph of Mount St. Helens crater showing remnants of spines 4 and 5 in southeast sector of crater and disintegrating mound of debris 14
13. Photographs of spine 4 taken on February 22 and January 14, 2005, showing the slickenside-decorated ultra-cataclasite and fault-gouge carapace of the spine 15
14. Plots of all major element analyses for rocks of Mount St. Helens by stage and period 18
15. Spider diagrams for Mount St. Helens rocks 21
16. Schematic cross section of Mount St. Helens plumbing system, updated to include constraints from the 2004–2008 eruption 22
17. Shaded relief map of Mount St. Helens and terrane to the north and east 24
18. Geologic map showing deposits from the May 18, 1980, eruption and the following summer and fall 26
19. Photograph of lower part of Pumice Plain from Boundary Trail along Johnston Ridge 27
20. Photograph of section through secondary blast deposit, overlying pyroclastic density current deposit of May 18, 1980, and subsequent phreatic deposit 29
21. Photograph showing deposits near the entrance to Mathematicians' gully 29
22. Oblique aerial photograph of the Pumice Plain taken in August of 1980 showing the Mathematicians' gully area 29
23. Oblique aerial photograph from August 1980 of the Mathematicians' gully area 30
24. Photograph illustrating cross section of pyroclastic-flow deposits exposed along the east wall of Mathematicians' gully 31
25. Excerpt of geologic map near and photograph illustrating flow and deposit evolution in June 12, 1980, flows near the northeast termination of this deposit 32
26. Aerial photograph of June 12, 1980, pyroclastic-flow deposits taken shortly after June 12 33
27. Aerial photograph of the July 22, 1980, pyroclastic eruption taken shortly after the second eruptive event at 6:26 p.m 33

28. Excerpt of geologic map showing the July 22 pyroclastic flows in the Mathematicians' gully area 33
29. Panorama photographs from left to right showing continuous cross-sectional exposure of July 22 deposits in east wall of Mathematicians' gully 34
30. Photographs taken at Stops 4–7 showing detail from figure 29 35
31. Photograph showing detail of Mathematicians' gully section from outcrop of 1980 deposits along the east wall 35
32. Field map enlarged to illustrate features of the July 22 deposits near Mathematicians' gully 36
33. Diagram and photograph of debris flow 37
34. Diagram of "levee sharpening" 37
35. Schematic diagram and photographs illustrating the process of advance retro stacking 38
36. Photograph illustrating how breakaway from a retro-stacked sequence of flows crested at high angles owing to the slope of the retro-stack field 40
37. Photographs showing detail section of the MG 5–7 lobe on the west side of Mathematicians' gully 40
38. Photograph and sedimentological data from a single pumice lobe that has been sectioned a few meters above its terminus 41
39. Photograph showing breakaway headwall scarps and weakly leveed secondary-flow deposits of June 12 41
40. Photograph showing breakaway scarps and partial detachment steps of failed breakaways in June 12, 1980, deposits 42
41. Stratigraphic columns showing sections through the blast deposit on the crest of Windy Ridge 43
42. Photograph showing stratigraphic section at Stop 12 45
43. Harker diagrams for Kalama dacites and andesites compared to basalts from the Castle Creek period 49
44. Variation diagram of chromium versus SiO_2 for samples from the Kalama, Goat Rocks, 1980–1986, and 2004–2008 eruptive periods 50
45. Photograph of tephra section at Stop A-1 taken in 1990 54
46. Photograph showing section of 1980 blast deposit at the south end of the roadcut at Stop A-1 54
47. Photograph of common rock types exposed along the trail to the crater of Mount St. Helens 55
48. Photograph of Mount St. Helens from the trail to Loowit Falls showing distinctive rock units 55
49. Photograph taken in 2016 showing small canyon on trail to Loowit Falls that exposes basalt of the north flank overlain by basaltic andesite of Nelson Glacier 56
50. Photograph taken in 2016 showing Loowit Falls as seen from the Loowit Trail 56
51. Imagery of Mount St. Helens crater and steps area viewed from the north, showing our climbing route and prominent features 57
52. Photograph taken in 2016 looking south into Mount St. Helens crater from the northern breach 57
53. Imagery and plots of Crater Glacier advance 58
54. Panorama photograph showing stratigraphic section through 1980 pyroclastic density current deposits in the east wall of Loowit canyon 59

Tables

1. 1980 eruption observations and timing 6
2. Mount St. Helens eruptive history 9
3. Terminology of blast deposits by various authors 28
4. Distinctive characteristics of tephra units from Mount St. Helens erupted before 1980 46
5. Petrography and stratigraphy of lava flows of the late Castle Creek period 51

Field-Trip Guide to Mount St. Helens, Washington—An Overview of the Eruptive History and Petrology, Tephra Deposits, 1980 Pyroclastic Density Current Deposits, and the Crater

By John S. Pallister,[1] Michael A. Clynne,[1] Heather M. Wright,[1] Alexa R. Van Eaton,[1] James W. Vallance,[1] David R. Sherrod,[1] and B. Peter Kokelaar[2]

Introduction

This field trip will provide an introduction to several fascinating features of Mount St. Helens. The trip begins with a rigorous hike of about 15 kilometers (km) from the Johnston Ridge Observatory (9 km north-northeast of the crater vent), across the 1980 Pumice Plain, to Windy Ridge (3.6 km northeast of the crater vent) to examine features that document the dynamics and progressive emplacement of pyroclastic flows. The next day, we examine classic tephra outcrops of the past 3,900 years and observe changes in thickness and character of these deposits as we traverse their respective lobes. We examine clasts in the deposits and discuss how the petrology and geochemistry of Mount St. Helens deposits reveal the evolution of the magmatic system through time. We also investigate the stratigraphy of the 1980 blast deposit and review the chronology of this iconic eruption as we travel through the remains of the blown-down forest. The third day is another rigorous hike, about 13 km round trip, climbing from the base of Windy Ridge (elevation 1,240 meters [m]) to the front of the Crater Glacier (elevation 1,700 m). En route we examine basaltic andesite and basalt lava flows emplaced between 1,800 and 1,700 years before present (B.P.), a heterolithologic flow deposit produced as the 1980 blast and debris avalanche interacted, debris-avalanche hummocks that are stranded on the north flank and in the crater mouth, and shattered dacite lava domes that were emplaced between 3,900 and 2,600 years B.P. These domes underlie the northern part of the volcano. In addition, within the crater we traverse well-preserved pyroclastic-flow deposits that were emplaced on the crater floor during the summer of 1980, and a beautiful natural section through the 1980 deposits in the upper canyon of the Loowit River.

Before plunging into the field-trip log, we provide an overview of Mount St. Helens geology, geochemistry, petrology, and volcanology as background. The reader is also referred to two extensive compilations of papers on the 1980 and 2004–2008 eruptions (Lipman and Mullineaux, 1981; Sherrod and others, 2008) and to the many references cited in this guide. The volcano has been referred to as a "master teacher" (Newhall, 2000). The 1980 eruption and studies both before and after 1980 played a major role in the establishment of the modern U.S. Geological Survey (USGS) Volcano Hazards Program and our understanding of flank collapses, debris avalanches, cryptodomes, blasts, pyroclastic density currents, and lahars, as well as the dynamics of magma ascent and eruption.

In a short field trip, it is impossible to do justice to the field geology of Mount St. Helens; so we encourage you to return and explore the volcano and the Mount St. Helens Volcanic National Monument more thoroughly, which serves as a natural laboratory for the study of explosive volcanism.

Tectonic and Physical Setting of Mount St. Helens

Mount St. Helens is located about 75 km north-northeast of Portland International Airport and 135 km south of Seattle-Tacoma International Airport. It lies 50 km west of the main Cascades Arc trend, as defined by a line connecting Mount Adams, Mount Hood, Mount Jefferson, and Three Sisters volcanoes in Oregon, and only 75 km above the Wadati–Benioff seismic zone, which marks the location of the down-going Juan de Fuca oceanic plate beneath the North America margin (fig. 1).

The unusual position of Mount St. Helens west of the main arc trend is attributed to the Mount St. Helens seismic zone, which is interpreted as a northwest-trending, right-lateral strike-slip fault, one of several such dextral fault zones that accommodate movement of the Oregon fore-arc block, which is rotating clockwise owing to oblique subduction and compression by the northwestward translating Sierra Nevada block of California (Weaver and others, 1987; Wells, 1990; Wells and others, 1998). At a more local scale, Mount St. Helens lies along a tensional pull-apart basin that formed within the northeast-trending offset of the Mount St. Helens seismic zone. The offset and pull-apart basin are thought to result from the intersection of the Mount St. Helens seismic zone with older, northeast-trending basement faults, as illustrated in figure 2.

[1]U.S. Geological Survey.

[2]University of Liverpool.

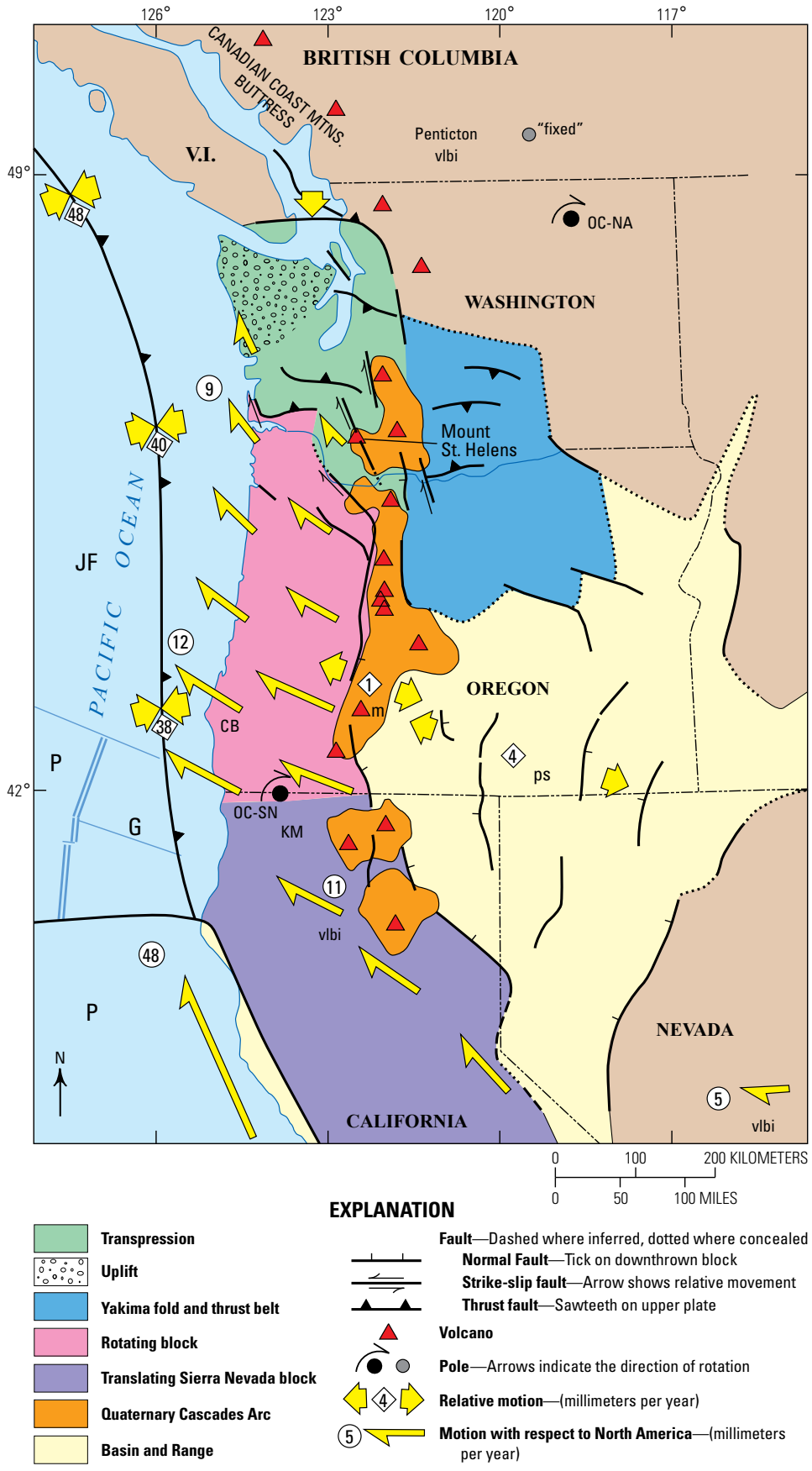

Figure 1. Index map showing the position of Mount St. Helens relative to the plate tectonic configuration of the northwestern United States and Canada. Figure modified from Wells and others (1998, fig. 4). Velocity fields from Oregon Coast-North America (OC-NA) and Oregon Coast-Sierra Nevada (OC-SN) poles with North America (NAM) fixed. Velocity rates (in millimeters per year) from very long baseline inteferometry (vlbi), paleoseismology (ps), Pacific-North America motion. Although shown in the transpressional area in this 1998 interpretation, Mount St. Helens lies within a northeast-trending trans-tensional basin along an offset of the the strike-slip Mount St. Helens seismic zone (strike-slip symbol adjacent to Mount St. Helens; shown in figure 2). JF, Juan de Fuca plate; P, Pacific plate; G, Gorda plate; CB, Cape Blanco; KM, Kalama Mountains; V.I., Vancouver Island. Additional symbols and numbers are defined in Wells and others (1998).

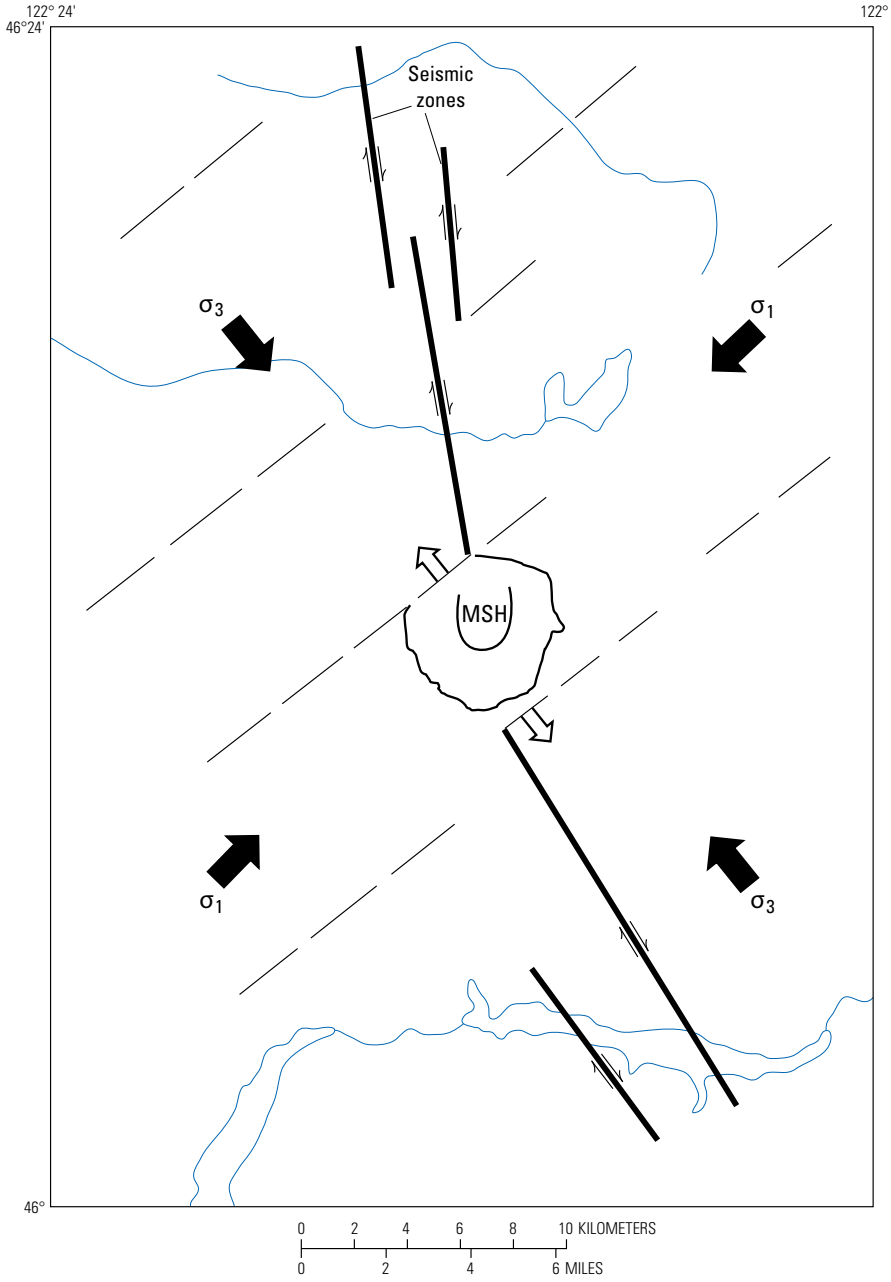

Figure 2. Map showing local tectonic setting of Mount St. Helens in an inferred pull-apart basin where an active, northwest-trending dextral fault (the Mount St. Helens seismic zone) intersects older, northeast-trending basement faults. Figure modified from Weaver and others (1987, fig. 6). MSH, Mount St. Helens. σ_1 and σ_3 indicate orientation of greatest and least compressional stresses.

In addition to its location west of the main arc trend, we believe that this tensional setting explains both the fact that Mount St. Helens is the most active volcano in the Cascades Arc (with five major explosive eruptions during the past 500 years) and the wide range in compositions of erupted products (Pallister and others, 1992). Magmas erupted at Mount St. Helens have ranged from basalt to rhyodacite with considerable range in basalt compositions, as described in subsequent sections of this guidebook. We suggest that the tensional setting enables ascent of basalts from the mantle wedge and dacites from the lower crust to reach a shallow crustal reservoir with little modification. In effect, Mount St. Helens lies along a "tear" in the crust, which facilitates magma ascent and subsequent magma mingling and mixing at shallow levels to produce intermediate (andesitic) compositions.

Eruptive History

We begin with a summary of the most recent, well-documented eruptions of Mount St. Helens and their deposits, then look back into the eruptive history of the past 3,900 years (the Spirit Lake eruptive stage).

Summary of 1980–1986 Eruptions

After a 123-year pause in eruptive activity, signs of reawakening at Mount St. Helens began with a small earthquake swarm on March 16, 1980. A few days later, a phreatic eruption blasted a crater through the volcano's summit ice cap (March 27). More phreatic and phreatomagmatic explosions continued through April 22 and then again from May 7 to 15 (Cashman and Hoblitt, 2004). At that time, a cryptodome was growing beneath the surface, deforming the north flank of the volcano. The intruding dacite magma bulged the edifice at a rate of 1.5–2.5 meters per day (m/d) (Lipman and Mullineaux, 1981).

On May 18, 1980, at 8:32 a.m. PDT, a *M* 5.2 earthquake accompanied the start of a catastrophic landslide. Most workers now associate the earthquake with the initial movement of the avalanche. As seen in the iconic photographs by Gary Rosenquist, the landslide took place in three stages (fig. 3). The initial Slide Block I was located above the cryptodome bulge. As the north flank failed, the headwall scarp of Slide Block I reached 600 m high, cutting into the bulge and exposing the cryptodome. Then Slide Block II, south of the original summit, failed almost immediately, removing about 1 km of overburden from the volcano. This sudden depressurization triggered a series of powerful explosions. The cryptodome and hydrothermal system blasted outward, creating a directed current known as the lateral blast.

Two minutes after the first earthquake, a second *M* 5 earthquake occurred (Endo and others, 1981). New explosions were observed above the crater rim as Slide Block III slipped away from the edifice (Waitt, 2015, p. 236). This second, laterally directed blast flowed outward and merged with the first, overtaking the debris avalanche and engulfing Mount St. Helens (Hoblitt, 2000). Snow and ice was stripped from the volcano, eroding about 6 m off Shoestring Glacier (Brugman and Post, 1981). Within 6 minutes of the first earthquake, the currents traveled as far as 28 km north and devastated 600 square kilometers (km^2) of rugged, densely forested terrain. The currents exhibited a range of behaviors from dense, granular to dilute and turbulent flow regimes (Hoblitt and Miller, 1984). The basal zone of the blast was slowed by the forest it consumed, reaching a

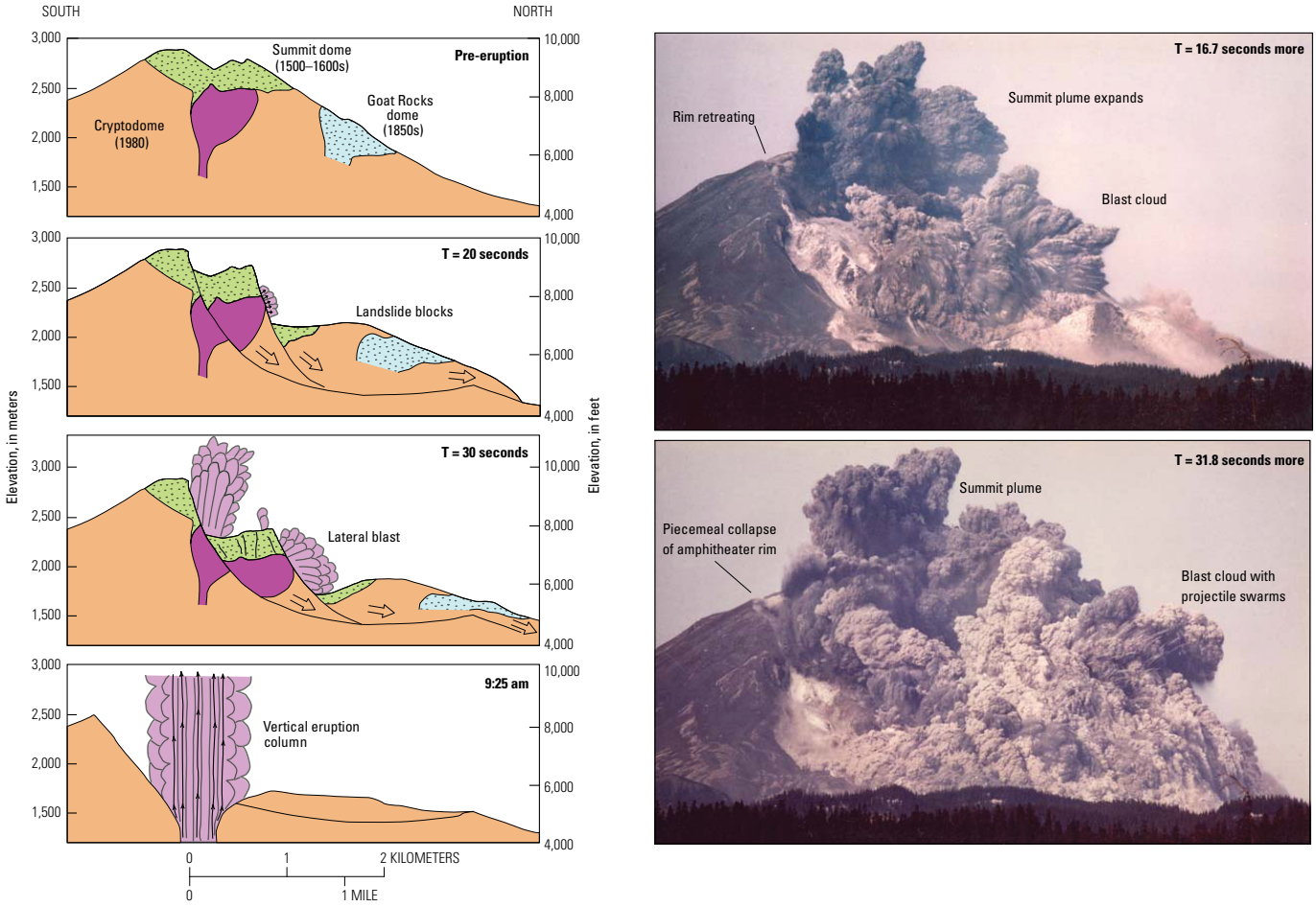

Figure 3. Cross sections and photos of Mount St. Helens showing positions of Slide Blocks I, II, and III on May 18, 1980, and relative displacement of key compositional features. Figure modified from Moore and Albee (1981); photographs by Gary Rosenquist.

velocity of about 100 meters per second (m/s) (350 km per hour [km/hr]). Velocities increased upward in the blast to reach 325 m/s (1,170 km/hr), just below the sonic velocity in the surrounding atmosphere. This near-sonic velocity and the strong attenuation of sound by suspended particles explain the fact that no preceding sound wave was heard by survivors. The temperature of the blast ranged from 327 degrees Celsius (°C) to just over 200 °C at the edge of the forest singe zone. Overall, the blast ejected about 0.12 cubic kilometers (km^3) dense rock equivalent (DRE) (about 20 percent of the volume of the cryptodome) (Moore and Sisson, 1981). The thermal energy flux was about 2.5 megawatts per cubic centimeter (MW/cm^3)—or about 2.5 times the energy of the Saturn Stage 1 engines that launched the Apollo astronauts to the moon—and the horizontal thrust was about 3.3×10^{12} newtons (Kieffer, 1981).

Meanwhile, beneath the lateral blast, the debris avalanche (2.5 km^3) flowed down the North Fork Toutle River and overtopped Johnston Ridge (Voight and others, 1981; Glicken, 1998). Its eastern margin ran into Spirit Lake (~7 km northeast), pushing the water as high as 265 m onto surrounding slopes (Waitt, 2015). Lahars accompanying this landslide flowed down the South Fork Toutle and Muddy Rivers, destroying roads and bridges (Pierson, 1985). However, the most destructive lahar, in the North Fork Toutle River, had an emergent onset, peaking 5–15 hours after the eruption (fig. 4). The lahar was generated by dewatering of the debris-avalanche deposit as it settled and the ice and snow within it melted (Janda and others, 1981).

As the lateral blast traveled outward, losing mass to sedimentation, its fine ash and hot gas began to rise buoyantly. By 8:42 a.m., a bent-over plume was observed issuing from the vent, intensifying to a dark-gray vertical column (Criswell, 1987). By 9:00 a.m., ash lofted into the stratosphere and spread out as a 30-km-high mushroom cloud (Sparks and others, 1986). This "co-blast" column was by far the tallest of the entire eruption (fig. 4). Pea-sized accretionary lapilli fell from the umbrella cloud for about the next half hour, covering areas as far as about 40 km north of the volcano (Sisson, 1995). After about 12:15 p.m., emissions changed to a lighter gray color, potentially reflecting increased fine-ash content. The column widened and became increasingly turbulent as pyroclastic density currents shed from its margins (Andrews and Gardner, 2009). Voluminous pyroclastic density currents

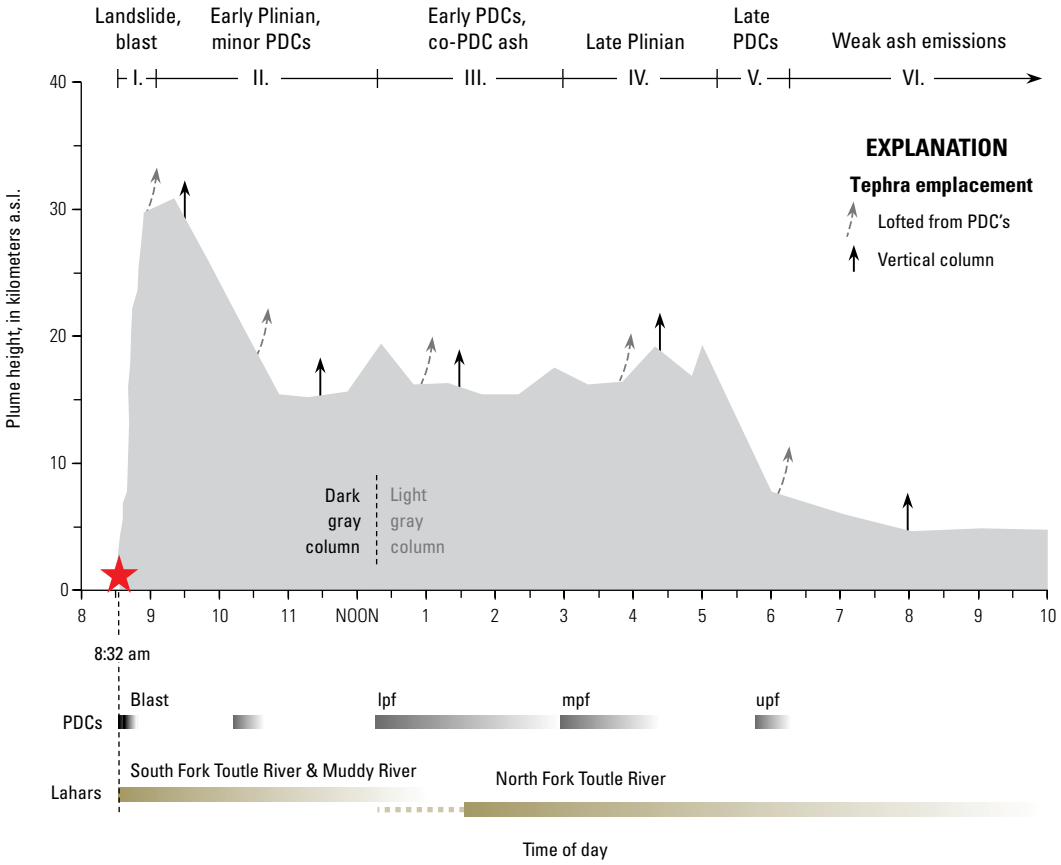

Figure 4. Diagram showing timeline of events and deposits from the May 18, 1980, eruption of Mount St. Helens. Times shown in Pacific Daylight Time (PDT). Plume heights show maximum heights detected by GOES satellite (Sparks and others, 1986; Holasek and Self, 1995) and radar (Harris and others, 1981). Eruptive phases I–VI are from Criswell (1987). Arrows indicate deposit origins, either from a vent-derived column or lofted from pyroclastic density currents (PDCs). Lower, middle, and upper pyroclastic-flow deposits are designated lpf, mpf, and upf, respectively; a.s.l., above sea level. Star indicates *M* 5.2 earthquake, coincident with onset of eruption at 8:32 a.m.

(fig. 5) filled a 5 by 8-km area north of the crater that would become known as the Pumice Plain. This sequence of vent-derived Plinian activity and intra-Plinian pyroclastic density currents continued into the evening. The column declined to 5–6 km after 6:00 p.m., producing ash emissions that lasted into the next day. Overall, the climactic phase of the May 18 eruption lasted for 9 hours and produced numerous pyroclastic flows and ash clouds that drifted downwind for hundreds of kilometers. Deposits from the May 18 eruptive events are summarized in tables 1 and 3.

Smaller, but substantial, explosive eruptions produced ash clouds and pyroclastic flows on May 25, June 12, July 22, August 7, and October 16–18, 1980 (table 1). Dome formation followed three of these explosions (June, August, and October), such that both the July and October eruptions destroyed domes. The October dome, in contrast, initiated a much longer period of episodic dome growth that ceased in 1986 (Swanson and Holcomb, 1990).

Figure 5. Photograph showing a vertical eruption column and pyroclastic density currents at 2:44 p.m. on May 18, 1980. View is from the southwest. Photograph by J.G. Rosenbaum, U.S. Geological Survey.

Table 1. 1980 eruption observations and timing.

[Two primary and one secondary pyroclastic-flow deposits crop out on the Pumice Plain; these probably occurred during the early, more energetic part of the eruption sequence. Less voluminous flows during the >5-hour eruption apparently were restricted to proximal areas and were not preserved in the stratigraphic record. Question marks in the "Time" column indicate exact timing of initial phase of these dome-forming eruptions is not known. Min, minutes; hr, hours; km, kilometers]

Date	Time	Flow unit	Duration	Plume height (km)	Runout (km)	Volume (km^3)	Area (km^2)
May 18	8:32 a.m.	Debris avalanche	<15 min	---	29	2.8	60
	8:32 a.m.	Lateral blast	4–5 min	grew to 30	27	0.19	600
	9:00 a.m.–12:00 p.m.	First Plinian and small pyroclastic flows		30–15	---	---	---
	12:17 p.m.	Pyroclastic flows (numerous)	~5 hr	19	8	0.12	15.5
May 25	2:32 a.m.	Pyroclastic flow (buried by June 12)		14	4	0.001	1.7
June 12	7:05 p.m.	No flow		11	---	---	---
	9:11 p.m.	Pyroclastic flows	Minutes to hours	15	7.5	0.01	8.3
	?	Dome					
July 22	5:14 p.m.	No flow	---	14	---		
	6:25 p.m.	Pyroclastic flow	5–10 min	18	6.5		
	7:01 p.m.	Pyroclastic flow	5–10 min	14	7.0		
		Total				0.006	4.8
August 7	4:23 p.m.	Pyroclastic flow	6.5 min	13	5.5	0.004	3.6
	?	Dome					
October 16	9:58 p.m.	Deposit not identified		13	?		
October 17	9:28 a.m.	Pyroclastic flow		14	4		
	9:12 p.m.	Pyroclastic flow		14	4	0.001	2.3
October 18	12:35 p.m.	Pyroclastic flow		8	small		
	2:32 p.m.	Dome		6			

Volcanologic and Petrologic Insights from the 1980–1986 and 2004–2008 Lava Domes

Several important field, experimental, and observational studies of the 1980–1986 dacites of Mount St. Helens have contributed to our understanding of shallow magmatic processes, their effects on eruption dynamics, and implications for volcanic hazards and eruption forecasting.

As detailed above, the eruptive sequence of Mount St. Helens in 1980 began months before the climactic eruption on May 18. At the time, it was unclear if magma had reached the surface during these early explosions. Initial reports suggested that they were steam-driven, but later analysis of the ash textures revealed a minor amount of juvenile material. Cashman and Hoblitt (2004) showed that 1–2 percent of ash erupted as early as March 28 was texturally identical to the later erupted cryptodome material, with high microlite crystallinities (45–55 percent) and abundant small plagioclase crystals, minor mafic microlites, rare cristobalite, and fresh unaltered glass. These fragments were texturally distinct from fragments from the old edifice. Furthermore, the proportion of juvenile grains increased through time before May 18. Although not detected at the time, these observations suggest that the magmatic system was becoming increasingly involved in the eruptions, pointing to the increasing explosive potential of the system. Cashman and Hoblitt also introduced the idea of using petrologic monitoring of ash as a forecasting tool for Mount St. Helens eruptions.

In addition to its presence in early erupted ash, cryptodome fragments also form most of the May 18 blast deposits (>50 weight percent) and include two distinct textural varieties—dark- and light-gray dacite (Hoblitt and Harmon, 1993). Both textural types are fresh and unaltered and have similar microlite populations (Cashman, 1988), but the dominant light-gray dacite (forming 72 percent of cryptodome-derived clasts) is more vesicular than subordinate dark-gray dacite (28 percent of cryptodome-derived clasts). The difference in color is due to different vesicularity and groundmass textures resulting from differences in degree of degassing and bubble collapse. The dark-gray dacite was already substantially degassed and vesicle-poor prior to eruption and did not vesiculate at all during eruption. In contrast, the light-gray dacite contained slightly higher dissolved water contents at the time of eruption, more than 0.2–0.4 weight percent (still degassed relative to initial water contents), and therefore underwent vesiculation during the May 18 eruption. Clasts with intermediate water contents (near the 0.2–0.4 weight-percent threshold) produced breadcrust bombs with outer rinds identical to the dark-gray dacite and interiors similar to the light-gray dacite (Hoblitt and Harmon, 1993).

The May 18, 1980, eruption also produced two varieties of pumice—white and gray—with slightly different bulk compositions. The white pumice is mafic dacite and the gray pumice is silicic andesite (Carey and others, 1990); however, the color variation is largely related to different crystal contents. The white pumice has a higher average vesicularity than the gray pumice (~86 percent versus 73 percent) but has no microlites (versus 7 percent in gray) and fewer phenocrysts (6 percent versus 15 percent, Klug and Cashman, 1994). The gray pumice forms a minor portion of the fall deposits erupted during the morning of May 18 but is comparatively more abundant in the pyroclastic density currents that began to form after 12:15 p.m. (Criswell 1987). Although the two pumice types are inferred to have similar eruptive paths resulting in their simultaneous eruption, the mafic gray pumice experienced more degassing and microlite crystallization. Criswell (1987) attributes the shift in eruption style at 12:15 p.m. to the increasing contribution of gas-poor magma.

Textural variation is also linked to changes in the post-May 18 eruptive behavior. Throughout the summer of 1980, the eruption style oscillated between effusive and explosive. Explosive eruptions produced deposits with varying proportions of several different textural types of clasts, with varying vesicularities and microlite contents (where microlites formed in response to decompression and degassing during shallow magma ascent; see, for example, Cashman, 1988; Geschwind and Rutherford, 1995; Blundy and Cashman, 2001, 2005). Clasts ranged widely from highly vesicular and microlite free to moderately vesicular and microlite rich. In some cases, clasts are juvenile with breadcrusted surfaces; others contain holocrystalline fragments of previously extruded domes.

Changes in the proportion of these textural types through time are inferred to represent changes in the conduit geometry and depth of magma storage in the eruption. Blundy and Cashman (2001, 2005) and Cashman and McConnell (2005) used melt-inclusion and textural data to show that the 1980–1986 dome-forming magma stalled during ascent from the vertically extensive magma storage area that has been envisioned in conceptual models of Mount St. Helens (for example, Lees, 1992, and subsequent parts of this guide). In particular, these studies showed that the June 12, 1980, deposits lack highly vesicular, microlite-free pyroclasts and also lack clasts typical of shallow dome material (there was no dome growth preceding the June eruption). Instead, the deposits contain abundant low-microlite-number-density clasts, implying that the deepest magma tapped during this eruption equilibrated at 3–4-km depth. In contrast, July and August eruptions produced the widest range in textural types, including microlite-free, highly vesicular clasts and dense holocrystalline dome material, suggesting that magma originated from a wide range of pre-eruptive depths (from shallow levels to depths as great as 6.6 km). Combined with eruptive volumes (table 1), they suggested an effective decrease in the conduit diameter through time. Cashman and McConnell (2005) calculated a decrease in cylindrical conduit diameter from about 40 to 45 m in May and June to about 10 m in July and August based on the source depths and erupted volumes. They proposed that the effective diameter was large in June, when intrusions into the shallow system filled a plexus of shallow dikes (based on seismicity); crystallization and degassing of remnant magma caused subsequent intrusions (in July and August) to be focused into a narrower area (or smaller number of dikes), decreasing the effective conduit diameter. Finally, Blundy and others (2006) proposed that latent heat of crystallization could increase the temperature of the conduit magma during decompression-induced

crystallization. The dacite spines at Mount St. Helens erupted during 2004–2008 provided strong evidence of such a process. Pallister and others (2008) found that the spines, which had undergone extensive decompression crystallization, had anomalously high oxide temperatures.

These studies have important implications for eruption forecasting, as relationships between gas loss and microlite growth during magma ascent impact magma viscosity, vesiculation, and ultimately, explosivity. Figure 6 illustrates two end members in explosivity resulting from different degrees of gas loss during magma ascent. If water and other volatile components are retained in the magma owing to either rapid ascent or lack of a permeable gas-escape pathway, an explosive eruption is produced. However, if these volatile components are lost owing to slow ascent and (or) a permeable pathway, the magma solidifies and stalls on its way to the surface or is extruded as a low-explosivity lava dome. We attribute such differences in eruptive behavior to gas loss and microlite crystallization during ascent through magmatic conduits, as documented at Mount St. Helens during the 1980–1986 and 2004–2008 dome eruptions (Blundy and others, 2006; Scandone and others, 2007).

In the extreme case, extensive gas loss through vertically permeable fault gouge surrounding a conduit can drive extensive decompression-induced crystallization (Gaunt and others, 2014). This process may solidify the upper 1 km of conduit magma into a cylindrical plug that is extruded as a spine, as occurred at Mount St. Helens in 2004–2008 (Pallister and others, 2013). In other cases, gas loss is less severe and thin microcrystalline caps form at the shallow tops of the magma columns in conduits. Such caps act as temporary plugs, allowing gas pressure to build in underlying magma. When this pressure exceeds the strength of the cap, an explosive eruption ensues,

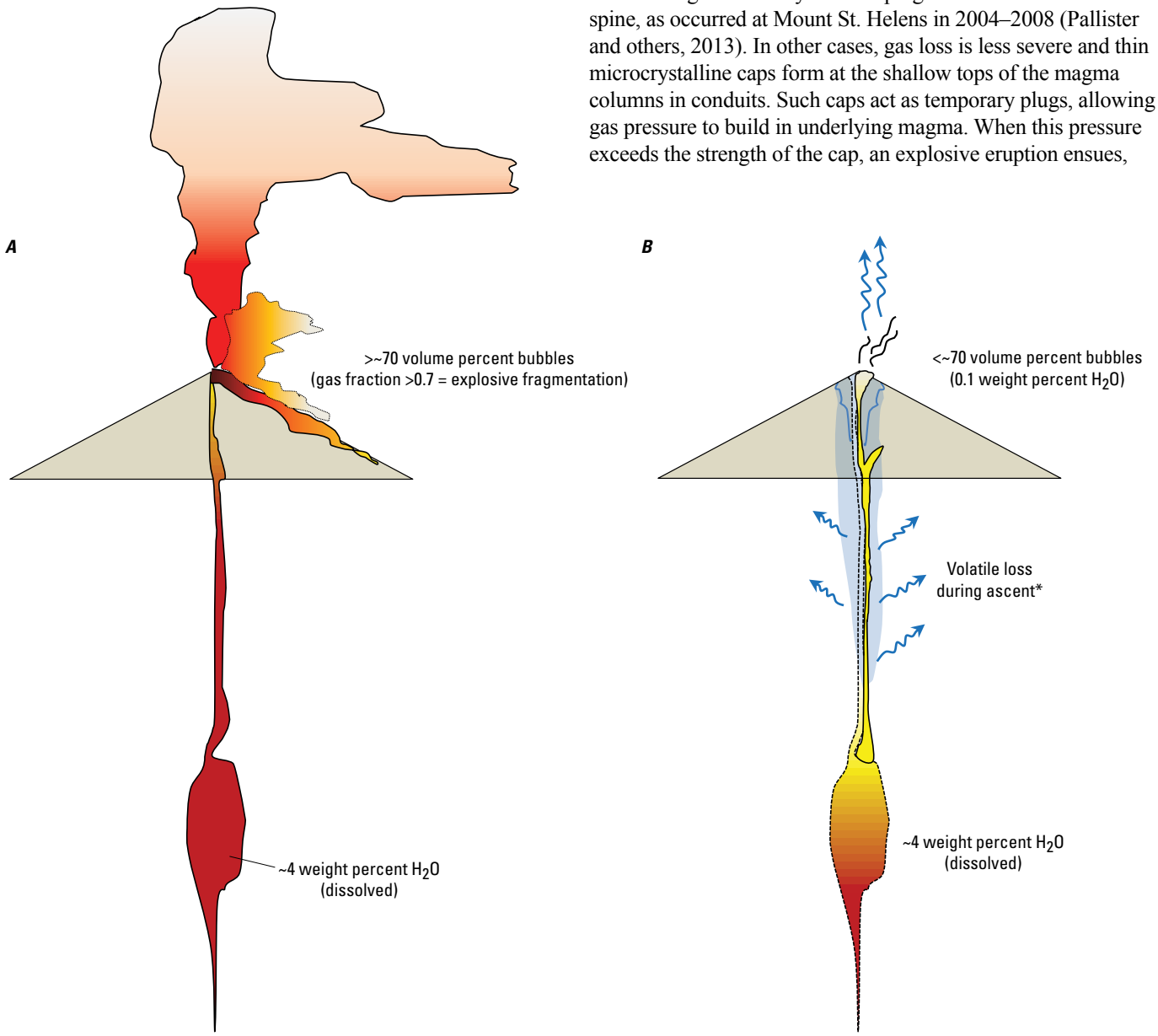

Figure 6. Schematic cross sections of a stratovolcano, its crustal magma reservoir, and conduit illustrating the effect of rapid (*A*) versus slow (*B*) ascent and related gas loss on eruption explosivity. Red indicates relatively gas-rich magma; yellow indicates partly degassed magma. Asterisk indicates multiple controls on volatile loss, including porosity and permeability of wall rocks and dynamics of volatile separation and transport from the magma.

destroying the cap along with overlying lava-dome material. The process produces microcrystalline tephra fragments that represent juvenile magma but are commonly mistaken as older lithics, as they may lack glassy cuspate bubble-wall textures (Gaunt and others, 2016). It is likely that repeated cycles of microcrystalline cap formation, conduit pressurization, and explosion are common in the early stages of magma ascent at long-dormant volcanoes, as well as at volcanoes that have repeated periods of modest lava-dome growth followed by explosive destruction, such as Popocatépetl, Mexico. Such a model of microcrystalline cap formation was proposed by Wright and others (2007) to explain the 1999 eruptions of Guagua Pichincha volcano in Ecuador.

Pre-1980 Eruptive History

Mount St. Helens has been the most active volcano in the Cascade Range during the past 3,900 years. However, it has a much longer eruptive history, much of it obscure. Work by D.R. Mullineaux and D.R. Crandell in the 1960s–1980s focused on the extensive tephra deposits found around the volcano to establish the general eruptive history. They recognized that the eruptive history of Mount St. Helens was episodic and grouped the tephras into sets of similar age and composition (Mullineaux, 1996 and references therein), which they described as a series of eruptive stages and periods, and correlated some of the lava flows, domes, and fragmental deposits with them (Crandell, 1987). Crandell divided the eruptive history of Mount St. Helens into four major eruptive stages, each lasting several thousand to a few tens of thousands of years (Ape Canyon, Cougar, Swift Creek, and Spirit Lake) (table 2). Consistent with greater preservation of deposits of the more recent past, Crandell further divided the most recent Spirit Lake stage into six periods (Smith Creek, Pine Creek, Castle Creek, Sugar Bowl, Kalama, and Goat Rocks). Mullineaux (1986, 1996) further divided the deposits of Mount St. Helens broadly into an old sequence (>2.5 ka [thousand years ago]) and a modern sequence wherein distinctly hotter and more mafic magmas (including basalts) were erupted. Radiocarbon dating provided some geochronologic control, but Crandell and Mullineaux's work was hindered by the lack of preserved tephras older than about 60 ka because these had been removed by glaciation. Thus, the

Table 2. Mount St. Helens eruptive history.

[Modified from Clynne and others (2008). Includes only major eruptive products of each period. Some geochronology is still unresolved, especially during the Swift Creek stage. Letter designations may refer to the period or stage of eruption (S, Swift Creek stage; P, Pine Creek period), distinguishing colors (W, white; Y, yellow), or composition (B, basaltic) (other letter designations do not represent specific features). This chronology takes into account reassignment of set-B tephras Bh and Bo (Mullineaux, 1996) from Castle Creek period to late Pine Creek period]

Eruptive stage	Eruptive period	Ash set	Major eruptive products
Spirit Lake 3,900–0 years B.P.	Modern period 1980–2008 C.E.	1980	Lateral blast and debris avalanche, pyroclastic flows, dacite domes, lahars
	Goat Rocks period 1800–1857 C.E.	layer T	Andesite flows, dacite dome, block-and-ash flows
	Kalama period 1479–1750 C.E.	layer z, set X, set W	Dacite domes, pyroclastic flows, block-and-ash flows, andesite flows, lahars
	Sugar Bowl period 1,050–1,000 years B.P.	layer D	Dacite domes, lateral blast
	Castle Creek period 2,025–1,700 years B.P.	set B	Dacite domes and flows, block-and-ash flows, basalt to andesite flows, lahars
	Pine Creek period 3,000–2,550 years B.P.	set B set P	Dacite domes, block-and-ash flows, andesite flows, debris avalanches, lahars
	Smith Creek period 3,900–3,300 years B.P.	set Y	Dacite domes, block-and-ash flows, pyroclastic flows, lahars
	Dormant interval 10–3.9 ka		
Swift Creek 16–10 ka		set J, set S	Dacite domes, block-and-ash flows, pyroclastic flows, lahars
	Dormant interval 18–16 ka		
Cougar 28–18 ka		set K, set M	Dacite domes, block-and-ash flows, debris avalanche and pyroclastic flows, andesite flows, lahars
	Dormant Interval 35–28 ka		
Ape Canyon >270–35 ka	Possible dormant interval 240–160 ka	set C	Dacite domes, block-and-ash flows, lahars

conventional wisdom developed that Mount St. Helens came into existence about 40–50 ka.

New geologic mapping aided by argon geochronology, paleomagnetic directional data, and additional radiocarbon chronology established that Mount St. Helens has a much longer eruptive history than recognized by Crandell and Mullineaux (Clynne and others, 2005; Clynne and others, 2008 and references therein). Deposits and rocks as old as 272 ka were discovered beneath younger deposits and in lahars. Table 2 summarizes the stratigraphic results of both Crandell and Mullineaux's seminal work and the refinements added by new mapping and chronology. Mount St. Helens lavas are particularly difficult to date by the Ar-Ar method. In addition to being young, they generally have low K_2O, and commonly contain excess argon in inherited crystals (Layer and Gardner, 2001; Clynne and others, 2008). In general, more dating has tended to extend the stages and close the gaps (dormant intervals) between them, and additional chronology is likely to continue to refine these intervals. The eruptive history reported by Crandell and Mullineaux emphasized the major Plinian eruptions of the volcano for which it is famous, but each major eruption of Mount St. Helens was followed by a substantial period of less explosive and effusive activity. Brief descriptions of each stage and period follow.

Ape Canyon Stage

During the Ape Canyon stage (the earliest time interval found so far), Mount St. Helens produced a variety of quartz-bearing biotite and (or) hornblende dacites and rhyodacites and set-C tephras. Figure 7 shows the extensive history of volcanism during this stage. These rocks are found as glaciated remnants beneath younger rocks on the southwest flank of the volcano. The oldest and most prominent of these is Goat Mountain (272±1 ka). However, most of the dated Ape Canyon rocks are found as clasts in lahar deposits in the Lewis River valley or in glacial deposits. Ape Canyon rocks are also found as lithic clasts in younger Plinian deposits, in an 84.2±21.9-ka dacite dome exposed in the crater floor, and in a blast deposit from the Sugar Bowl dome dated at 1,030±30 years B.P. The presence of these rocks indicates that Ape Canyon rocks underlie the present edifice. Zircon as old as about 500 ka found in gabbroic inclusions suggests that volcanism or intrusion at Mount St. Helens began well before 272 ka (Claiborne and others, 2010). Here, we are using the term "Ape Canyon" as both a stratigraphic stage for the set-C tephras and associated pyroclastic density current deposits that range from about 30–50 ka, as well as for all of the earliest rocks associated with the Mount St. Helens magmatic system, which we now know extend to as old as 500 ka.

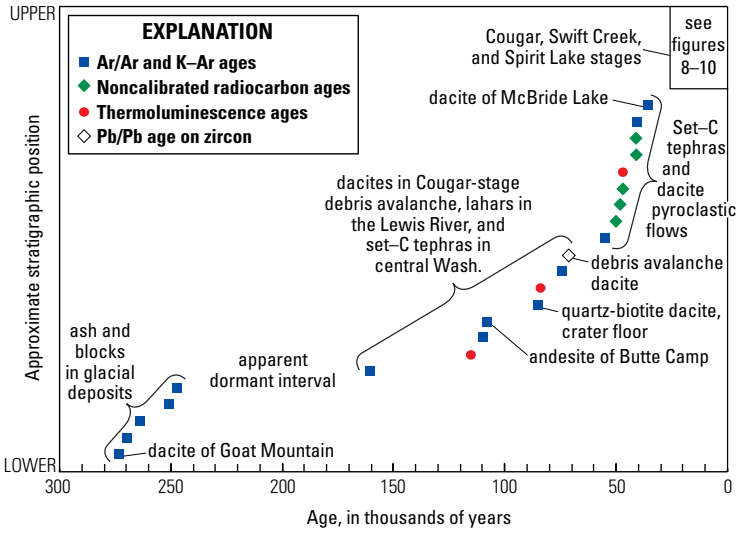

Figure 7. Plot of dated Ape Canyon-stage deposits. Uncertainties are relatively small compared to the time scale here and are not shown. Modified from Clynne and others (2008) with additional unpublished results.

Cougar Stage

During the Cougar stage, Mount St. Helens produced a variety of hypersthene-hornblende dacite domes, pumiceous pyroclastic flows, set-K and set-M tephras, and at least two andesite lava flows (fig. 8). A large debris avalanche at about 24.5 ka on the southwest flank of the volcano blocked the Lewis River. The debris avalanche was immediately followed by emplacement of several cubic kilometers of pumiceous pyroclastic flows. Breaching of the blockage released large breakout lahars down the Lewis River. The 0.75-km^3 Swift Creek andesite lava flow on the south flank was the largest such lava flow in Mount St. Helens history. Olivine-bearing magmatic inclusions in a Cougar-stage andesite lava flow found in Pine Creek mark the first appearance of an unambiguous mafic component in the Mount St. Helens magmatic system. This lava flow was assigned to the Cougar stage by Crandell (1987) based on presence of overlying set-J and set-Y tephra layers.

Swift Creek Stage

During the Swift Creek stage, the widespread set-S and set-J tephras were erupted, and three extensive fans of fragmental debris were emplaced on the flanks of Mount St. Helens from hypersthene-hornblende dacite domes. The Crescent Ridge fan on the west to northwest flank was derived from Crescent Dome, which is preserved high on the west flank. Swift Creek-stage domes exposed in the east crater wall may have been the source of the Cedar Flats fan on the northeast flank of the volcano and in the Lewis River valley. The source of the Swift Creek fan on the south flank is unknown, but probably buried. Most fan material originated as block-and-ash flows, but much material in the distal parts of the fans was remobilized as lahars. Details of the Swift Creek stage are still not well known, but subtle differences in the rock types suggest that the three fans represent three discrete periods of eruption between about 16 and 13.5 ka (fig. 9).

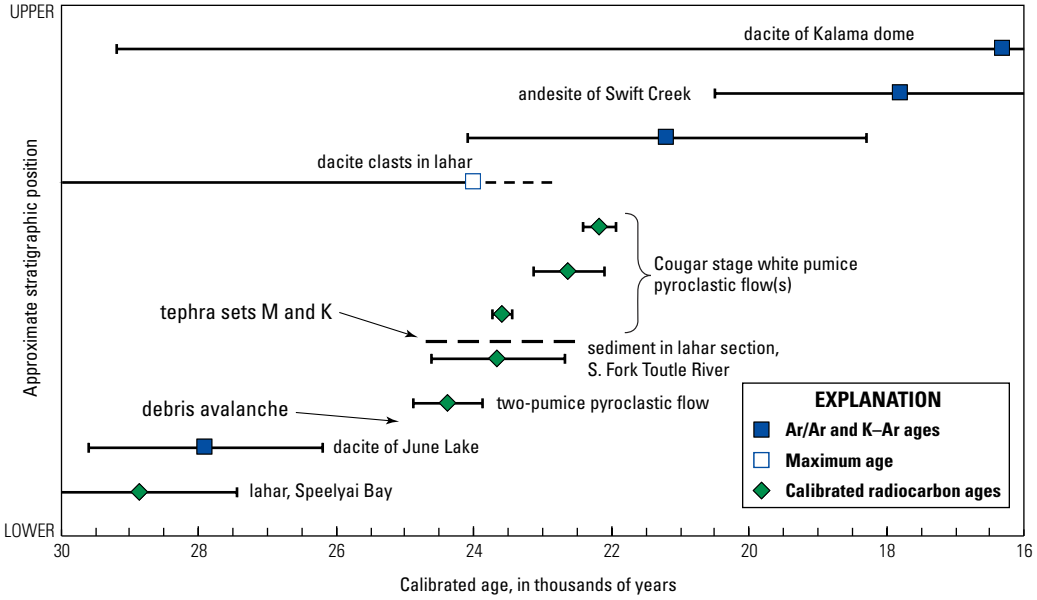

Figure 8. Plot of dated Cougar-stage deposits. Uncertainties are 1σ. From Clynne and others, 2008. Data from Crandell and others (1981), Major and Scott (1988), and Scott (1988b).

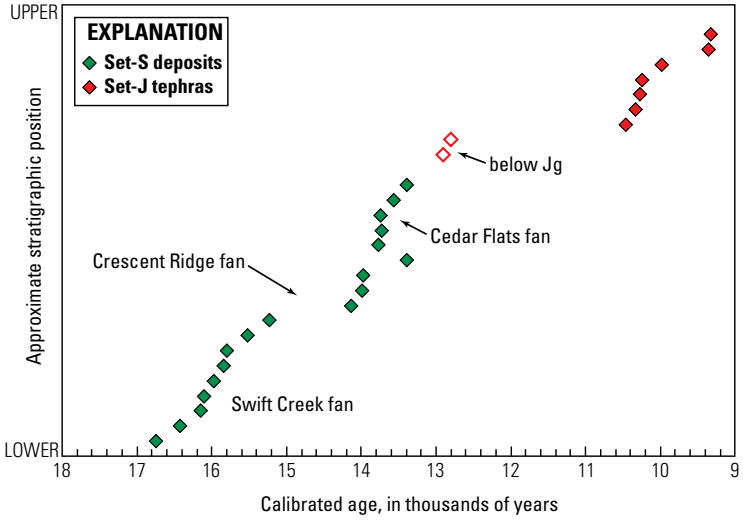

Figure 9. Plot of dated Swift Creek-stage eruptions and deposits. All ages are calibrated radiocarbon. Some ages are on glacial deposits enclosing set-S tephra or peat, lahar deposits, or sediment in the fans. Open red symbols are samples from below tephras (limiting ages). Uncertainties not shown, but are generally about 50–300 years. See Clynne and others (2008) for additional details and description of samples. There are no ages for the Crescent Ridge fan deposits; its approximate stratigraphic position is indicated. Data from Crandell and others (1981), Hyde (1975), Mullineaux (1996), Waitt (1985), Davis and others (1982), Baker and Bunker (1985), Clague and others (2003), Porter and others (1983), S.C. Porter and T.W. Swanson, written commun. (2006), and Micheal Clynne, U.S. Geological Survey (unpublished radiocarbon ages).

Spirit Lake Stage

The Spirit Lake stage is the youngest stage of Mount St. Helens, and is the best known interval of the eruptive history because it is the best exposed and dated. The Spirit Lake stage is divided into seven eruptive periods separated by short noneruptive intervals (table 2): (1) Smith Creek period, ~3,900–3,300 years B.P., (2) Pine Creek period, ~3,000–2,550 years B.P., (3) Castle Creek period, ~2,025–1,700 years B.P., (4) Sugar Bowl period, ~1,050–1,000 years B.P., (5) Kalama period, 1479–~1750 C.E., (6) Goat Rocks period, 1800–1857 C.E., and (7) modern period, 1980–2008 C.E. (fig. 10).

Smith Creek Period

During the Smith Creek period, Mount St. Helens erupted a series of pumiceous dacite tephras, set Y. The single largest eruption in the volcano's known history produced the Yn tephra layer (~4 km^3 DRE; Carey and others, 1995). The Yn tephra was followed in quick succession by the Ye tephra (~1 km^3 DRE) (Carey and others, 1995), which is dated at about 3,350 years B.P. Pyroclastic flows, lava domes, and lahars were emplaced after each of the major set-Y explosive events. A fan of fragmental material on the north flank dammed the North Fork Toutle River and formed ancestral Spirit Lake.

Pine Creek Period

During the early Pine Creek period, Mount St. Helens erupted an extensive series of dacite domes and the lithic-rich set-P tephra, followed by a later series of andesitic lava flows, pyroclastic flows, lahars, and tephras Bh and Bo (these set-B tephra layers were formerly assigned to the subsequent Castle Creek period, but are reassigned here to the Pine Creek period

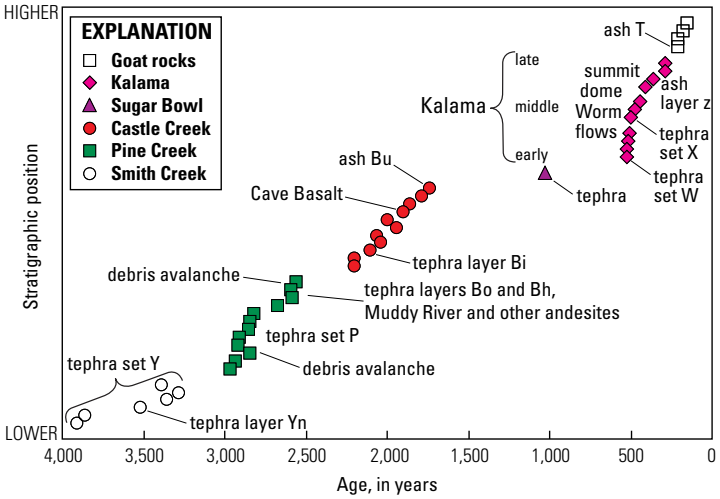

Figure 10. Plot of dated Spirit Lake-stage eruptions and deposits. Uncertainties not shown, but generally about the size of the symbols. Ash set P is undated but correlated with dated Pine Creek flowage deposits and ash layer z, which is thought to be a composite of ash-fall deposits that overlap with the extended time interval of summit-dome eruptions. Selected radiocarbon, dendrochronoloy, and historical ages from Greeley and Hyde (1972), Crandell and others (1981), Yamaguchi (1983, 1985), Crandell (1987), Scott (1988a), Yamaguchi and others (1990), Yamaguchi and Hoblitt (1995), Mullineaux (1996), Hausback (2000), Micheal Clynne, U.S. Geological Survey (unpublished radiocarbon ages), and James Vallance, U.S. Geological Survey (unpublished radiocarbon ages).

as a result of new geochronology). Pine Creek-period dacite domes are exposed in the 1980 crater walls and extensive fans of lithic pyroclastic material and associated lahars are present in Pine Creek and Castle Creek drainages. Two debris avalanches on the north flank resulted from collapses of Pine Creek-period domes (Hausback and Swanson, 1990; Hausback, 2000). Damming of Spirit Lake by one of these fans or avalanches resulted in huge lake-breakout lahars in the lower Toutle River valley (Scott, 1988b). Pine Creek dacitic activity took place during most of the interval between about 3,000 and 2,550 years B.P. About 2,550 years B.P., the dacitic activity was followed by tephra Bh and abundant andesite lava flows and then tephra Bo and more basaltic andesite to andesite lava flows and lahars. Much of the andesitic fragmental material seen in the 1980 crater walls was erupted during a short interval beginning about 2,550 years B.P.

Castle Creek Period

The Castle Creek period was the most complex and compositionally diverse period of the Spirit Lake stage. Compositions from dacite to basalt were erupted during a roughly 325-year-long period between about 2,025 and 1,700 years B.P., in three phases (early, middle, and late). The early phase was primarily dacitic and included the northwest dome and Dogs Head dacite domes and pumiceous and lithic pyroclastic flows, andesite-dacite lava flows (at Redrock Pass on the south flank and at the north rim), and tephra Bi, all probably in the interval from about 2,025 to 1,990 years B.P. Deposits of the middle Castle Creek period are confined to the south flank of Mount St. Helens. This period was initiated by eruption of basaltic tephra Bu1, and followed by three units of mafic lava flows: basalts and basaltic andesites of the south flank, pre-Cave Basalt and basaltic andesite, and Cave Basalt. These eruptions took place shortly before and at about 1,895 years B.P. During the late Castle Creek period, Mount St. Helens erupted eight (or possibly nine) units of basalt to andesite on the north and east flanks of the volcano. In order of eruption these are (1) andesite of section 26, (2) basaltic andesite of Truman Trail, (3) tephra Bu2 and basalt of the north flank, (4) andesite of the Plains of Abraham, (5) andesite of Sasquatch Steps, (6) tephra Bu3 and basalt of Castle Creek, (7) basaltic andesite of Nelson Glacier, and (8) Steps "S" andesite. The andesite of the Baguette lava flow, a pyroxene andesite of uncertain age on the southwest flank, is compositionally similar to the andesite of Sasquatch Steps and may be related to the late Castle Creek period. These eruptions took place between about 1,800 and 1,700 years B.P. Four radiocarbon ages for units 5 and 6, range from 1,795±30 to 1,730±35 years B.P., and paleomagnetic directional data suggest that this period of volcanism was short. Late Castle Creek-period lava flows form the uppermost units along parts of the post-1980 crater rim.

Sugar Bowl Period

During the Sugar Bowl period, at least three dacite lava domes were erupted, Sugar Bowl dome, East Dome, and West Dome. A small lateral blast, associated with emplacement of Sugar Bowl dome and tephra layer D, occurred 1,030±30 years B.P. As noted previously, the blast contains sparse lithic blocks of the Ape Canyon stage, demonstrating the presence of these much older rocks under the edifice. Paleomagnetic directional evidence indicates that the Sugar Bowl period was probably short lived, and all the activity probably occurred between about 1,050 and 1,000 years B.P.

Kalama Period

The Kalama period is described as three phases of activity (early, middle, and late) that are correlated with set-W, set-X, and layer-z tephras respectively (Hoblitt and others, 1980; Mullineaux, 1996). Ages of the tephras and flowage deposits are determined by tree-ring dating and paleomagnetism (Yamaguchi and Hoblitt, 1995). The early Kalama period began with a major dacitic tephra Plinian eruption, Wn tephra (2 km^3 DRE; Carey and others, 1995), in late 1479 C.E. Activity continued for several decades and included dacite dome growth, eruption

of another major dacite tephra, We tephra (0.4 km^3 DRE; Carey and others, 1995) in 1482 C.E., and several smaller tephra eruptions and pyroclastic flows. The middle Kalama began about 1505 C.E. and included several small explosive events (andesitic pyroclastic flows and set-X tephras), lava flows, and lahars. These were followed by eruption of an extensive set of andesite lava flows (Worm Complex and related lava flows) and small pyroclastic flows, probably about 1545–1550 C.E. The late Kalama period saw the growth of a large andesite-dacite summit dome that formed the upper part of Mount St. Helens prior to 1980. Growth of the summit dome probably began about 1650 C.E., and during its formation abundant lithic pyroclastic material and lahar deposits were emplaced on the flanks of the volcano. Magmatic growth continued to at least 1725–1750 C.E. and lahar activity continued on some flanks of the volcano as late as 1885 C.E. (Yamaguchi and Hoblitt, 1995; Hagstrum and others, 2002).

Goat Rocks Period

The Goat Rocks period included eruption of dacitic tephra layer T (0.4 km^3 DRE; Carey and others, 1995) in 1800 C.E., emplacement of the Floating Island andesite lava flow, also in 1800 C.E., and growth of the Goat Rocks dome from about 1830 to 1857 C.E. (Hoblitt and others, 1980; Yamaguchi and others, 1990). In conjunction with emplacement of the Goat Rocks dome, repeated small hot-collapse events built a large fan of lithic pyroclastic material (Goat Rocks fan).

Modern Period

The modern eruptive period includes precursory, pyroclastic, and dome-building events between 1980 and 1986 as well as an episode of spine-dominated dome growth that took place during 2004–2008. Extensive information on the chronology, volcanology, and petrology of the modern eruptive period can be found in two USGS Professional Papers (Lipman and Mullineaux, 1981; Sherrod and others, 2008) as well as in dozens of papers in the volcanological literature. It is beyond the scope of this field-trip guide to cover all of this material; instead we summarize key findings that are relevant to this field trip in the sections that follow.

1980–1986

The events leading to and following the 1980 eruption are well documented in the extensive collections of papers in Lipman and Mullineaux (1981). To recap, an earthquake swarm that began in late March 1980 was followed by a small crater-forming steam explosion on March 27 and similar explosions continued until mid-May. During this period a 0.11-km^3 cryptodome was emplaced, leading to dramatic bulging of the north flank of Mount St. Helens. On May 18 a *M* 5+ earthquake triggered a massive landslide of the north flank, which produced a debris avalanche; unloaded the cryptodome and the underlying magmatic system; and led, in rapid succession, to a laterally directed blast and then a Plinian eruption column. The lateral blast devastated a 600-km^2 area north of the volcano and produced a lithic-rich and fines-depleted blast deposit containing two types of juvenile dacite (glassy black and crystalline gray) from the margin and interior of the cryptodome respectively (Hoblitt and Harmon, 1993), as well as abundant lithic fragments derived from the older rocks of the volcano. Pumiceous dacite tephra from the Plinian eruption was carried downwind more than 1,500 km east and pyroclastic flows extended to the north base of the volcano, where their deposits overlie the debris-avalanche and blast deposits. Lahars and floods were generated from the rapid melting of snow and ice and from water within the landslide deposits. They extended down the North Fork Toutle River more than 100 km to the Columbia River. Smaller eruptions on May 25, June 12, July 22, August 7, and October 16–18, 1980, each produced pyroclastic flows and eruption columns to more than 10-km altitude, which deposited additional pumiceous tephra. Extrusions of dacite in the crater built small lava domes in May, June, and August that were destroyed by later explosions. A subsequent dome then appeared in October and continued to grow through at least 15 eruptive episodes between 1981 and October 1986 (Swanson and others, 1987; Swanson and Holcomb, 1990; Fink and others, 1990), eventually attaining an estimated volume between 77 and 91 million cubic meters (Mm^3).

1986–2004

Volcanic quiescence at Mount St. Helens was accompanied by substantial geomorphic change of the crater floor and walls during this period, resulting from nearly continuous rock fall and debris avalanches that occur each year between late spring and fall. Persistent dust clouds that emanate from the crater rim are a result of the daily rock falls, which are initiated high on the crater walls. Although materials eroded from the crater walls and deposited on the crater floor are a predictable response to the nearly instantaneous creation of the 700-m headwall resulting from the May 18, 1980, landslide, the most notable geomorphic response was the stabilization of permanent ice within the crater.

Elevated temperatures associated with the 1980–1986 dome eruptions inhibited buildup of substantial snow and ice on the crater floor. Small patches of snow and ice were present along the base of the deeply shaded south amphitheater walls in 1985 and 1986 and a large snowbank between the south wall and dome, extending around the east and west sides of the dome, is visible in aerial photographs from 1989 and 1990. Aerial photographs from 1996 reveal a small glacier in the southwest part of the amphitheater, containing several crevasses and a bergschrund-like feature at the head of the ice body (fig. 11). The small 1996 glacier (~0.1 km^2) grew to about 1 km^2 in aerial extent by 2001, with a maximum thickness of about 200 m.

Estimates of glacier volumes were determined by subtracting a 1980 post-eruption digital elevation model (DEM) surface from a high-resolution DEM determined from aerial photographs taken in September 2000 (Schilling and others, 2004). By late 2001, the volume of the glacier had grown to about 120 Mm^3, about one-third of which is thought to be rock debris derived mainly from rock avalanches from the surrounding amphitheater wall. Within less than a decade, the Crater Glacier had become the largest

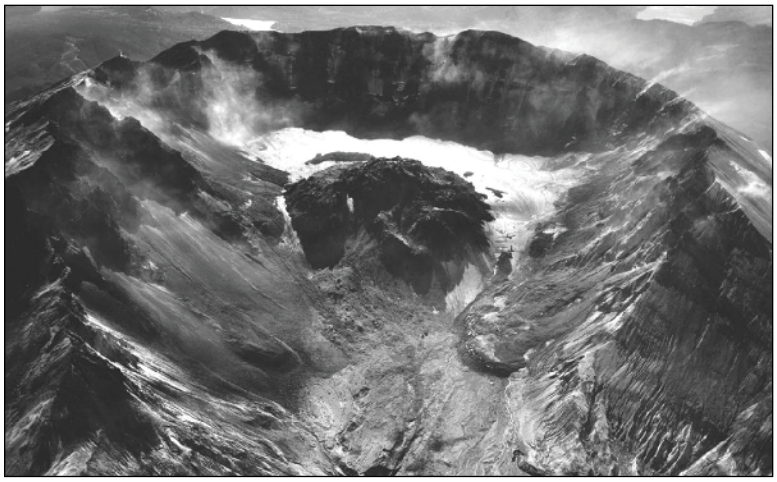

Figure 11. Aerial photograph of Mount St. Helens crater looking south toward the newly formed glacier at the base of the amphitheater wall. Note rock glaciers near the eastern and western margins of the glacier. Small crevasses and a bergschrund-like feature formed near the south crater wall (the latter obscured by shadow in this image). Photograph by Bergman Photographic Services (under contract to U.S. Geological Survey) taken on October 5, 2000. The glacier has grown and changed considerably since this the photograph was taken.

glacier on Mount St. Helens and had an areal extent of about 0.1 km^2, exceeding the area of all the other remaining glaciers on Mount St. Helens combined—all of which were beheaded, removing their snow accumulation areas.

2004–2008

Eighteen years after dome-forming eruptions ended in 1986, and with little warning, Mount St. Helens began to erupt again in October 2004. During the ensuing 4 years, the volcano extruded about 100 Mm^3 of gas-poor, crystal-rich dacite lava (Schilling and others, 2008; Diefenbach and others, 2012). An extensive database of geophysical and volcanological information exists for the 2004–2008 eruption. These data were described and relations between monitoring data and eruptive processes were published in an extensive series of papers (Sherrod and others, 2008). This volume includes a summary of the 2004–2008 eruption by Scott and others (2008).

The lava was erupted as seven dacite spines (Vallance and others, 2008). Each was extruded in succession from a single vent at the south margin of the 1980–1986 lava dome, and each brought the faulted conduit margin to the surface, which was formed in the preceding days to months (Scott and others, 2008). The third, fourth, and fifth spines were recumbent "whalebacks" with smooth fault-gouge-covered upper and lateral surfaces (fig. 12). During a period of weeks to months, each of the spines broke into slabs and then disintegrated to varying degrees. The spines were composed of chemically homogeneous dacite (65 percent SiO_2) that underwent decompression crystallization at shallow levels (<2 km) of the conduit. This process of shallow microlite crystallization increased the total crystal content to as much as 87 percent and solidified the magma prior to extrusion (Pallister and others, 2008; Cashman and others, 2008), forming the spines.

One of the most unusual and distinctive features of the eruption was the occurrence of swarms of repetitive, small, low-frequency earthquakes repeating at very regular intervals (for example, about 1 minute), termed "drumbeats" (Moran and others, 2008; Waite and others, 2008). These drumbeat earthquakes have been modeled physically as the result of periodic stick-slip motion along the margins of the conduit (and their low-frequency components have been attributed to low rupture velocities and path effects; Harrington and Brodsky, 2007).

The dacite spines were each mantled by cataclastic rocks, including slickensided ultra-cataclasite and fault gouge (fig. 13). As reviewed by Cashman and others (2008), similarities

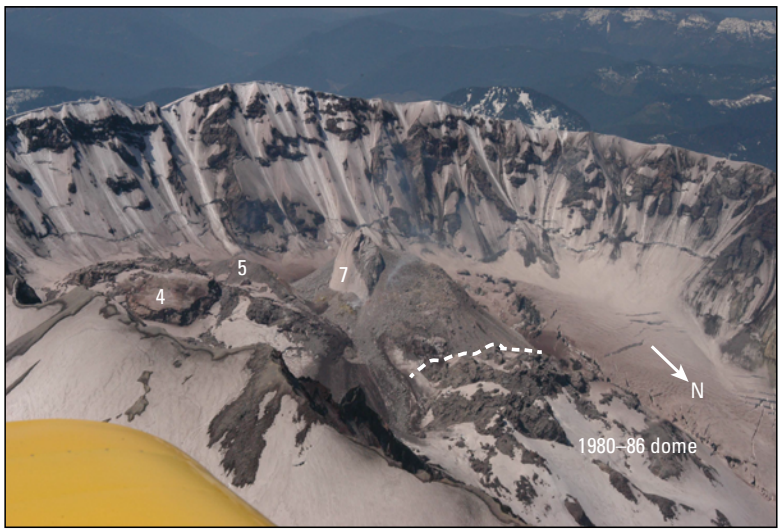

Figure 12. Oblique aerial photograph of Mount St. Helens crater on May 17, 2006, looking southwest and showing remnants of spines 4 and 5 in southeast sector of crater (4, 5) and disintegrating mound of debris surrounding spine 7, which is rising steeply from vent. Note the fume rising from the vent area at the northern margin of spine 7. The 1980–1986 dome (labeled) is the lower mass of rock with snow cover north of spine 7. Dashed line indicates contact between the 1980–1986 and 2004–2008 domes. Pink to gray ash on snow is from small ash clouds generated during repeated collapses of spine 7. Diameter of the Mount St. Helens crater is about 2 km.

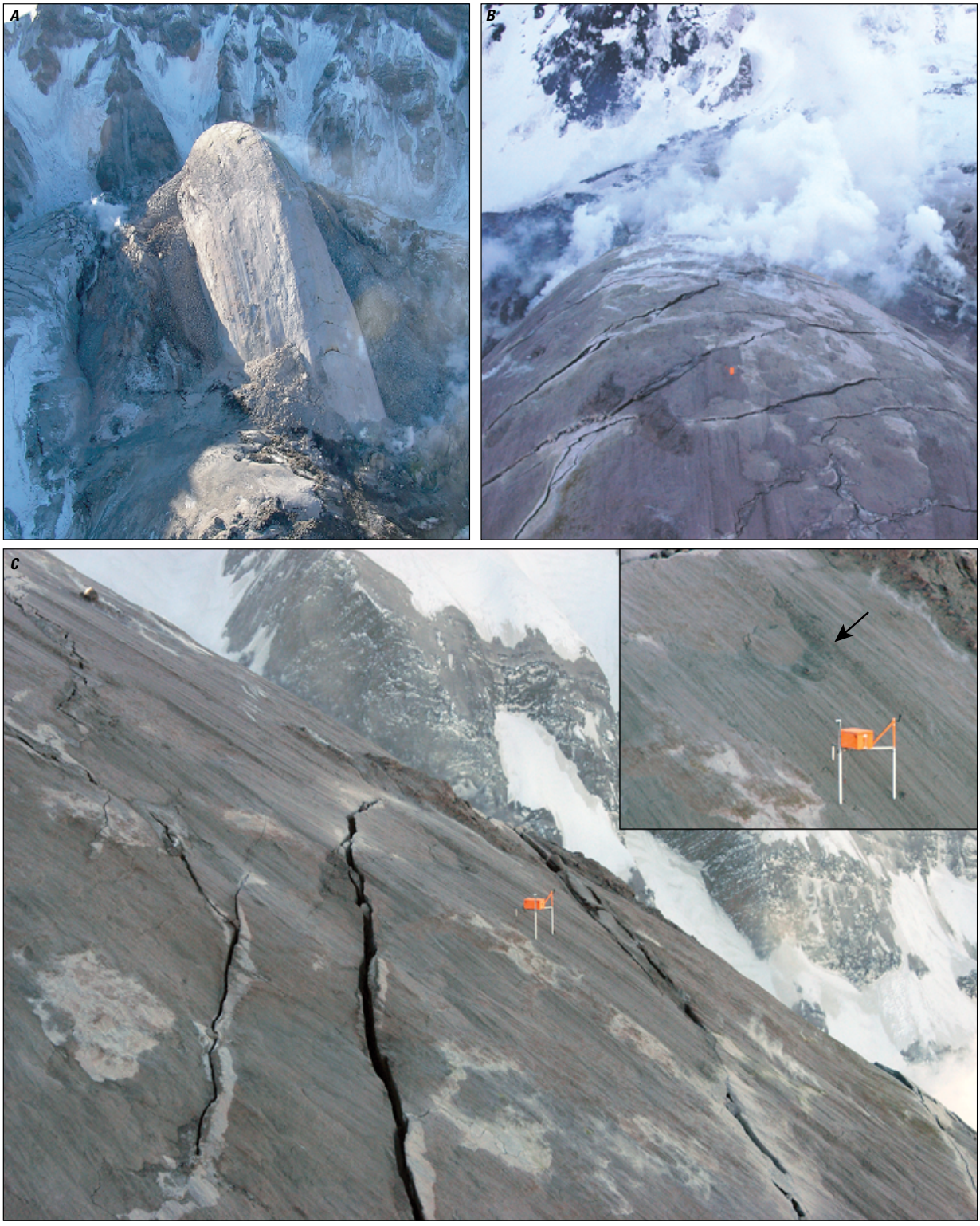

Figure 13. Photographs of spine 4 taken on February 22 (*A*) and January 14, 2005 (*B*, *C*), showing the slickenside-decorated ultra-cataclasite and fault-gouge carapace of the spine. *A*, View to south. Width of the spine is about 120 m. *B*, View looking down and to the north from above the summit of the spine. *C*, View to west across spine surface showing continuity of individual slickenside lineations (grooves) over tens to hundreds of meters. The orange device at center-frame is a portable "spider," a global positioning system and seismic instrument package that was positioned by helicopter on the dome surface. The spider instrument box is 0.7 m in length. Inset image is an enlargement of the area of *C* near the spider, showing an eroded surface (arrow) and multiple levels of slickensided gouge. Figure from Pallister and others (2013).

between the Mount St. Helens gouge zone and tectonic fault zones are remarkable and structural studies of the fault rocks surrounding the spines also favor a stick-slip mechanism (Pallister and others, 2013).

Geochemistry and Petrology

The eruption of Mount St. Helens in 1980 generated an abundance of interest in the geochemistry and petrology of the volcano. Much of the ensuing work was focused on the 1980 deposits or was very specialized. Any student of the volcano should be aware of several special publications on the geology, especially Lipman and Mullineaux (1981), Sherrod and others (2008), and Journal of Geophysical Research v. 92, no. B10. During the past 37 years our understanding of the geochemistry and petrology has advanced, but application of petrologic principles to Mount St. Helens rocks has been limited owing to lack of information of the detailed stratigraphy of various periods of the eruptive history. New geologic mapping is alleviating that shortcoming. Here we focus on generalities that contribute to understanding the broad aspects of Mount St. Helens geochemistry and petrology.

Summarizing work done before 1980, Hopson and Melson (1990) recognized a cyclic eruption pattern and compositional cycle in the Spirit Lake stage at Mount St. Helens. Cycles consist of a repose interval in which compositional and thermal gradients developed in the magmatic system followed by an eruptive interval, which progressively taps the zoned system. The cycle begins with a large explosive Plinian eruption of dacite to rhyodacite and is followed by progressive eruption of domes and lava flows punctuated by small pyroclastic eruptions. Mafic phenocryst assemblages evolve from being amphibole dominated to being pyroxene dominated and bulk compositions evolve from dacitic to andesitic. Hopson and Melson attributed this cyclic behavior to the development of zoned magma bodies that were intermittently replenished from below. Although generally valid, the more detailed eruptive history available today shows the Mount St. Helens magmatic system to be more diverse and complex than the Hopson and Melson model.

Mount St. Helens is fundamentally a bimodal volcano. It has two parental magma types—one basaltic and the other dacitic—with abundant evidence of magma mixing to produce intermediate composition andesites. The relative proportions of the two parental magmas and the composition of the dacitic component have evolved during the life of Mount St. Helens, probably in conjunction with the flux into and maturity of the magmatic system. These and other characteristics of Mount St. Helens magmas are described and discussed below. During the Ape Canyon stage, Mount St. Helens erupted hypersthene-hornblende and quartz-bearing hornblende or hornblende-biotite dacite to rhyodacite. Dacites dating from the Cougar stage and later generally contain hypersthene and hornblende (±sparse augite, ±cummingtonite) and quartz is rare. Input of basalt into the Mount St. Helens magmatic system and eruption of andesite is first recognized near the end of the Cougar stage. The abundance of basalt and andesite greatly increased in the late Pine Creek period and has dominated parts of the Castle Creek and Kalama periods.

Mineralogy

Mount St. Helens phenocryst assemblages display a range of characteristics. Calcic hornblende and hypersthene dominate dacite mineral assemblages; augite is sparse and a few rocks contain cummingtonite, commonly coexisting with hornblende. The most silicic rocks are quartz-bearing hornblende-biotite dacites to rhyodacites. Plagioclase is the dominant phase in all dacites; alkali feldspar is absent and quartz is sporadic. Basalts are generally olivine-bearing, commonly with inclusions of chromium spinel. Augite is sparsely present in some basalts, and plagioclase is generally the second most abundant phase. Basalts generally do not display disequilibrium mineral assemblages or textures. Basaltic andesites to andesites typically contain some combination of olivine, augite, and hypersthene with olivine-augite assemblages more common in basaltic andesite and augite-hypersthene assemblages in andesites. Hornblende is not an important phase in most andesites. Plagioclase dominates the phase assemblage of basaltic-andesite to andesite compositions.

Effusive dacites are generally finely to coarsely porphyritic. Coarsely porphyritic dacites typically contain plagioclase with a variety of complex zoning patterns that indicate crystallization in a variety of temperature, pressure, and pH_2O conditions. Sieved plagioclase is common, but typically does not dominate the assemblage of any particular rock, and indicates that mixing between felsic magmas of similar composition is common. Some effusive dacites and most pyroclastic dacites tend to contain plagioclase with less complex zoning patterns (for example, the Sugar Bowl-period dacite). Some effusive dacites (for example, the Kalama-period summit dome) contain sparse large phenocrysts but very abundant small plagioclase crystals that indicate forced crystallization during ascent and degassing.

Basaltic andesites and andesites have three fundamentally different textural types: (1) those that generally represent equilibrium conditions, (2) those that represent weak disequilibrium conditions, and (3) those that represent strong disequilibrium conditions. Equilibrium-condition andesites are generally coarsely porphyritic (olivine)-augite-hypersthene andesites with weakly zoned plagioclase-dominated assemblages (for example late Pine Creek-period andesites forming much of the modern cone). These commonly contain glomeroporphyritic clots of the same minerals. Strong-disequilibrium-condition andesites are characterized by multiple populations of plagioclase and disequilibrium assemblages of mafic minerals. These have a range of phenocryst abundances from a few to 30–40 percent. Those with sparse phenocrysts contain ragged remnants of mostly resorbed crystals (for example the Castle Creek-period dacite of Redrock Pass), and generally have silicic andesite to dacite compositions. More porphyritic examples commonly contain partially reacted olivine and augite phenocrysts, coexisting hypersthene and hornblende phenocrysts that are not stable in

the bulk composition, and coexisting calcic plagioclase and strongly sieved sodic plagioclase (for example middle-Kalama-period andesites correlative in age with the set-X tephras). Weak-disequilibrium-condition andesites also have assemblages composed of combinations of olivine, augite, and hypersthene, but, the crystals are small (<1 mm) and do not have strong-disequilibrium textures. Plagioclase is dominant and has a variety of textural populations. These rocks have basaltic andesite to andesite bulk compositions. Some rocks that straddle the andesite–dacite boundary contain assemblages of augite and hypersthene with or without hornblende that represent equilibrium conditions (for example early-Castle Creek andesites or dacites).

The wide variety of mineral and textural assemblages in these rocks is controlled by (1) the relative proportions of mixing between felsic and mafic parental magmas and (2) the length of time the magmas undergo re-equilibration. Porphyritic and strong-disequilibrium rocks erupted shortly after mixing took place, and nearly aphyric rocks were erupted after most phenocrysts were resorbed but before crystallization of a new mineral assemblage was advanced. Weak-disequilibrium rocks erupted after most old phenocrysts were resorbed and a new mineral assemblage began to replace them, but before they grew large. Equilibrium rocks did not erupt until the evidence for mixing was nearly to completely eliminated by recrystallization.

Dacites like the late-Kalama-period summit dome are most likely to represent the composition of the modern primitive felsic component at Mount St. Helens, and dacites like Goat Mountain probably represent the older primitive component. A range of basalt types most likely represent the mafic components. Most, if not all, andesites are probably derived by mixing and re-equilibration of dacite and basaltic components.

Inclusions

A variety of types of inclusions are present in Mount St. Helens deposits. The most abundant inclusions (90 percent, Heliker, 1984) have cumulus (many laminated or layered) and hypidiomorphic granular textures and are (augite)-hornblende-hypersthene gabbro or diorite in mineral assemblage. These first appear in dacites erupted during the Cougar stage and are especially abundant in Swift Creek, Kalama, and 1980–1986 and 2004–2008 dacite dome rocks. They generally are angular with joint-bounded margins and display reaction and partial melting textures. They are sparse to rare in Plinian deposits, but become abundant in subsequent effusive dacites. These contain 25–20 Ma zircon (U-Pb ion-probe ages on zircon grains, John Pallister, USGS, written commun.), and they are probably from the wall rock of the shallow magmatic system. As the shallow system inflates, magma interacts with the wall rocks, stressing and partially melting them. After major Plinian eruptions, the magma chamber deflates, relaxing stress, and the walls spall joint blocks into the remaining magma (Pallister and others, 1991, 1992).

Olivine-bearing and non-olivine-bearing quench-textured mafic inclusions first appear in Cougar stage rocks and are common in Pine Creek and early-Kalama dacites. These represent basalt intruded into and quenched by the dacitic magma chamber. Coarse-grained cumulus-textured inclusions with broadly gabbroic compositions first appear in Castle Creek period and are found thereafter. These typically have olivine-augite (±hypersthene) assemblages dominated by plagioclase and contain a residual liquid component. Wanke and others (2016) showed that some of these contain zircon with ages in the range of 350–5 ka and thus overlap with the age range of the Mount St. Helens magmatic system. Mineral equilibria suggest that they crystallized at depths of 10–23 km, and thus represent intrusion of basalt into the base of the Mount St. Helens magmatic system (Wanke and others, 2016)—a hypothesis proposed earlier for the mafic inclusions by Heliker (1984, 1995) and Pallister and others (1991).

Coarse- to medium-grained hypersthene-hornblende inclusions with substantial amounts of residual liquid (the same phenocryst assemblage as their host) and compositions only 2–4-percent-SiO_2 more mafic than their host are common in some Pine Creek dacites and sparse in younger dacites. These probably represent mush crystallized on the sidewalls of the magmatic system (Wanke and others, 2016). Hornfels-textured inclusions derived from crustal volcanic rocks and other types of crustal inclusions are rare (Heliker, 1995).

Major Element Composition

Compilation of literature and USGS data includes 1,076 samples (not including 1980–1986, 1991, or 2004–2008 dacites). These probably represent the bulk of the geochemical diversity in Mount St. Helens, although there is considerable redundancy and the dataset may not be completely representative of the eruptive volumes of stages and periods. Although a variety of compositions from basalt to rhyodacite have erupted, for most of its history Mount St. Helens has been a fundamentally dacitic volcano and all other compositions are subordinate (fig. 14).

Overall, Mount St. Helens rocks of all ages form a compositional continuum. SiO_2 ranges continuously from 49 to 70 weight percent, although there are fewer samples in the 54–56 percent and 59–61 percent SiO_2 intervals. Major oxides plot as thin to thick bands versus SiO_2. K_2O ranges from 0.5 to 2.0 weight percent, and there is considerable spread at the mafic end of the array (fig. 14*A*). Two trends in the K_2O variability merge at high SiO_2. The lower K_2O trend consists mostly of Ape Canyon-, Cougar-, and Swift Creek-stage and Smith Creek-period rocks, whereas the upper K_2O trend consists mostly of Pine Creek-, Castle Creek-, Sugar Bowl-, and Kalama-period rocks. Some Pine Creek-, Kalama-, and Goat Rocks-period samples are intermediate between the two trends. MgO ranges from 0.7 to 7.4 weight percent, in a fairly tight array (fig. 14*B*), except for a group of Pine Creek andesites that have lower MgO, and a few, probably altered, set-C tephras (Ape Canyon stage).

At the mafic end of the arrays there are two clearly different parental magmas, one with minimal K_2O (Cave Basalt) and one with greater, but variable, K_2O (Castle Creek basalts). Other

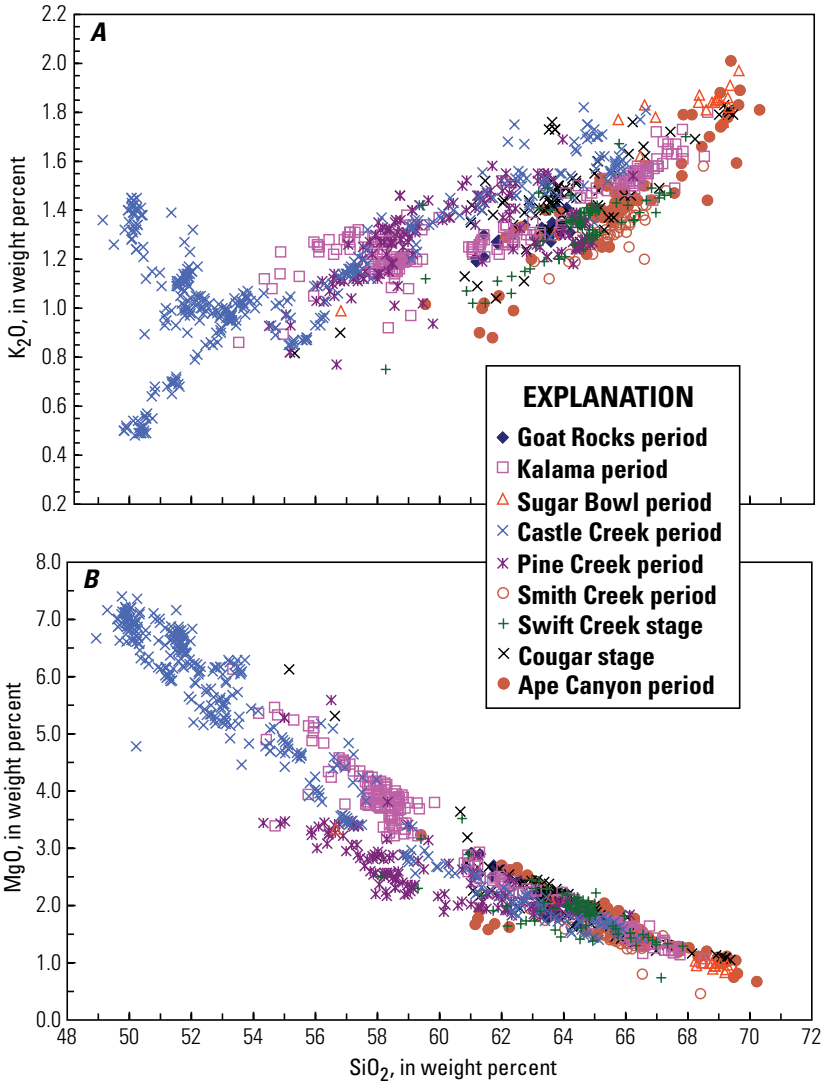

Figure 14. Plots of all major element analyses for rocks of Mount St. Helens available from the literature and the U.S. Geological Survey (except 1980–1986 and 2004–2008 samples) by stage and period. *A*, SiO_2 versus K_2O. The data form a broad array of increasing K_2O with increasing SiO_2. In detail, the data form several arrays correlated with stage or eruptive period. Most of the older rocks from the Cougar and Ape Canyon stages tend to have lower K_2O at equivalent SiO_2 than Spirit Lake-stage rocks (except Smith Creek- and some Kalama-period rocks). Calc-alkaline basalts from the Castle Creek period are enriched in K_2O compared to the Cave Basalt and related rocks. *B*, SiO_2 versus MgO. The data form a coherent array of decreasing MgO with increasing SiO_2, except for some andesites erupted during the Pine Creek period and a few set-C tephras from the Ape Canyon stage (which are likely to be altered).

oxides behave as expected for arc volcanic rocks: FeO ranges from 2.5 to 10.5 weight percent, decreases steadily with SiO_2, and forms a fairly tight array except for a group of Pine Creek andesites and Castle Creek dacites that have higher FeO (not shown). The two arrays merge at about 65 percent SiO_2. TiO_2 and P_2O_5 display considerable variability (not shown) that correlates with K_2O content. Pine Creek andesites are especially high in TiO_2. Al_2O_3 ranges from 16 to 19 weight percent and the compositional array displays a hump shape, typical for arc rocks. Na_2O ranges from 3.3 to 5.1 weight percent and increases steadily with SiO_2 forming a thick band. FeO*/MgO ranges from about 1.25 to 3.5; no more primitive mafic rocks are present. FeO*/MgO in rocks from most periods increases steadily from mafic to felsic compositions, forming a thick band. However, Castle Creek basaltic andesite to dacites form a second parallel trend. At the higher end of the silica array, a few samples extend to higher FeO*/MgO, and most Pine Creek dacites and andesites have higher FeO*/MgO at equivalent SiO_2.

Two types of basalt are present, calc-alkaline arc basalt with a variable composition (49–53 percent SiO_2, as much as 7 percent MgO, ~1 percent K_2O) and relatively rare tholeiitic basalt (composition 50 percent SiO_2, 7 percent MgO, and 0.5 percent K_2O). Basalts were erupted only in the Castle Creek period, although some compositions—early-Kalama magmatic inclusions and middle-Kalama-period basaltic andesites—approach basaltic compositions. The calc-alkaline basalts have higher abundances of incompatible major elements (K_2O, TiO_2, and P_2O_5) than Cave and pre-Cave Basalts.

Overall, there is a coherent array of compositions at Mount St. Helens. Variability is most substantial at the mafic end of the arrays, and it is clear that there is a range of parental basaltic compositions. During some periods (especially Pine Creek), compositions fall off the main array for some oxides. Eruptive periods do not strictly correspond to magmatic periods; in other words, there may be more than one parental magma erupted during a period.

Trace-Element Composition

A compilation of trace-element data for Mount St. Helens rocks from the literature and the USGS includes 650 samples

from rocks that pre-date 1980; 560 of those are from the Spirit Lake stage. In addition, there are 75 analyses from 1980–1986 rocks and 45 from 2004–2008 rocks in the compilation. These data were acquired by a variety of methods including WDXRF, EDXRF, INAA, and ICP-MS. Although the data are probably representative of the geochemical diversity of Mount St. Helens, there is considerable redundancy and some rock units have sparse data. Consequently, the data are displayed as averages for three compositional groups: basalts, andesites, and dacites normalized to primitive mantle. Given the variety of methods used to generate the analyses and the number of laboratories, the data arrays are remarkably coherent.

Basalts

The two types of basalt at Mount St. Helens, calc-alkaline and tholeiitic, are compositionally different. Because of enrichments in high-field-strength elements (HFSEs; Nb, Ta, Hf, Zr, and Ti), the tholeiitic type has been compared to ocean island basalt (OIB) (Smith and Leeman, 1987; Pallister and others, 1992). Spider diagrams for both types have spiky patterns, and some of the incompatible-element abundances are higher in the calc-alkaline basalts (CABs) than in the tholeiites (fig. 15*A*). Mount St. Helens CABs have spikes at Ba, U, Sr, and Zr. The uranium spike is greater, the strontium spike is smaller, and the barium spike is weak compared to typical Cascade Range CABs—for example, those of the Lassen area (Borg and others, 1997). The HFSEs (for example, niobium and tantalum) are depleted but not as strongly as is typical for the Cascade Range, and one group of Castle Creek basalts (the OIB-type of Smith and Leeman, 1987) is not niobium-tantalum depleted. Light rare-earth element (LREE) abundances in CABs are 20–35 times higher than primitive mantle and heavy rare-earth element (HREE) abundances are 4–5 times higher (LREE/HREE 5–10). The tholeiitic Cave Basalt has LREE abundance 11–12 times higher than primitive mantle and HREE abundance is about 6 times higher (HREE/LREE ~2). The HREE pattern is not as flat as is typical for Cascade Range basalts in either CABs or tholeiites. Mount St. Helens basalts are relatively H_2O poor, containing only 1–2 percent (Rea and others, 2012). The basalts have weak arc geochemical signatures, implying that they are not directly generated by slab dehydration or that their slab signature is diluted through interaction with the asthenosphere and (or) mantle lithosphere. Each basalt unit has a slightly different composition, requiring the mantle composition and (or) degree of melting to be somewhat varied (Wanke and others, 2016). The Cave Basalt was probably derived from a different mantle domain than the other basalts. Although most of the basalts have similar geochemical patterns, they display more geochemical diversity than the andesites or dacites.

Dacites

Spider diagrams for dacites of Mount St. Helens are spiky with large spikes at uranium, potassium, and lead (fig. 15*B*). Abundances for the most incompatible elements are about the same as the most enriched CAB, but there is no barium spike. The niobium-tantalum depletion is much greater than in the basalts. Dacites have similar abundances of potassium, zirconium, and hafnium to the basalts but substantial spikes relative to adjacent rare-earth elements (REEs) and HFSEs. LREE abundances are about 20 times higher than primitive mantle and HREEs are about 2–4 times higher (LREE/HREE 5–10). LREE, HREE, niobium, and tantalum abundances are similar to or lower than the basalts, and only the most incompatible elements (Cs, Rb, Ba, and Th) have higher abundances. The similar and generally lower incompatible-element abundances in the dacites make it difficult or impossible to derive the dacites from the basalts by crystal fractionation. The absent or weak europium anomalies in the dacites do not permit fractionation or accumulation of substantial plagioclase. The relatively constant composition of the dacites implies derivation from a homogeneous magma by a relatively constant process. The older dacites (Ape Canyon and Cougar stages) have generally similar compositions with only slight differences from Swift Creek and the younger dacites.

Andesites

Spider diagrams for the andesites of Mount St. Helens are spiky like those for the dacites, with large spikes at uranium, potassium, and lead (fig. 15*C*). The andesites have a bit more variability than the dacites but the abundances and patterns are similar for most elements, except for lower cesium, rubidium, and barium abundances (like the basalts) and higher HREE abundances (also like the basalts). The REE and HFSE trace-elements abundances in several andesites are intermediate in composition between the enriched basalts and the relatively depleted dacites. Thus, the andesites appear to have trace-element-abundance patterns like mixtures of the basalts and dacites. As at other Cascade Range volcanoes, most of the compositional variability is derived from the mafic component.

Petrogenesis

The first important geochemical and petrologic study was by Smith and Leeman (1987). Their work resulted in two fundamental conclusions concerning the origin and evolution of Mount St. Helens lavas. They noted that many incompatible element abundances in dacites were similar to or lower than mafic compositions, whereas others (for example Ba, Rb, K, Cs and Sr) were enriched. They interpreted this pattern to mean that the dacites could not have been derived from fractional crystallization of mafic magma and instead were derived by melting of metabasalt in the lower crust. Isotopic geochemistry of some of the same samples (Halliday and others, 1983; Leeman and others, 1990) indicated that the crust that produced the magmas was very young and probably related to intrusion of Tertiary or contemporary arc basalt. Two recent experimental petrology studies support the crustal melting origin of Mount St. Helens dacite (Blatter and others, 2015, 2017; Riker and others, 2015). Blatter and others (2017) established that Yn

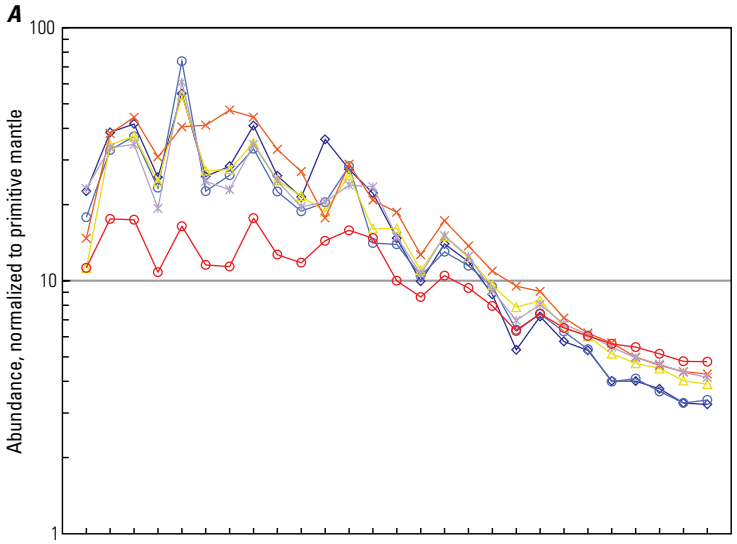

EXPLANATION

- Basalt and basaltic andesite
- Basaltic inclusions
- Basalt of Castle Creek
- Basalt of the north flank
- Basalt of the south flank
- Cave Basalt

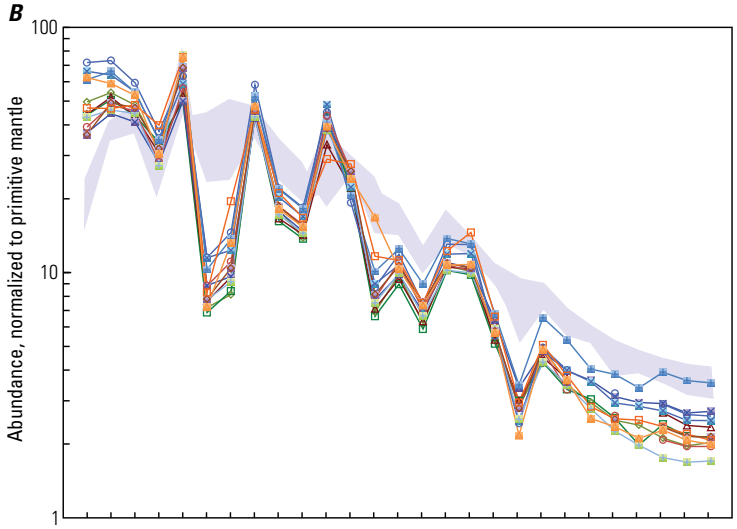

EXPLANATION

- 2004–2008
- 1980–1986
- Goat Rocks-period dacites
- Kalama-period summit-dome dacite
- Kalama-period dacite—early
- Sugar Bowl-period dacites
- Castle Creek-period dacites
- Pine Creek-period dacites
- Smith Creek-period dacites
- Swift Creek-stage dacites
- Cougar-stage dacites
- Ape Canyon-stage dacites
- Basalts from figure *A*

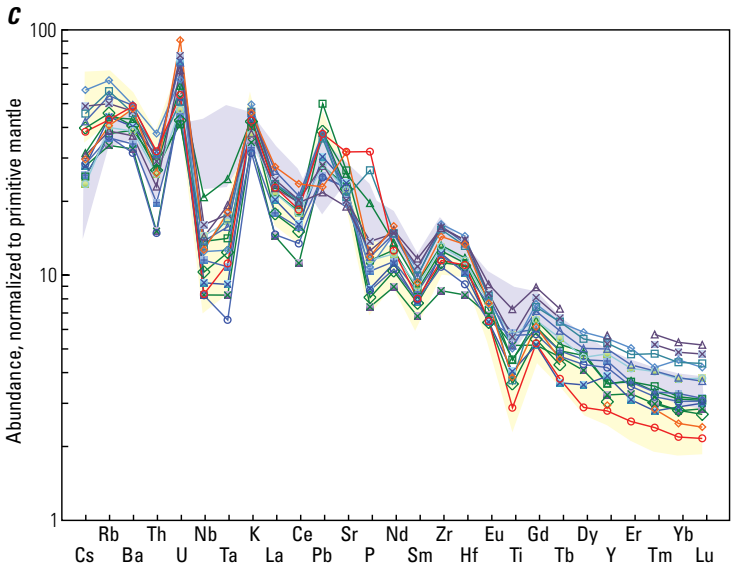

EXPLANATION

Goat Rocks period
- andesite of Floating Island

Kalama period
- Worm Complex andesite—middle
- set-X andesites and Xb tephra—middle
- Magmatic inclusions—early

Castle Creek period
- "S" andesite
- basaltic andesite of Nelson Glacier
- andesite of Sasquatch Steps
- andesite of the Plains of Abraham
- andesite of Truman Trail
- andesite of section 26
- andesite of Baguette lava flow

Pine Creek period
- W–74-type andesite and Bo tephra
- Loowit-type andesite and Bh tephra

Cougar stage
- andesite of Swift Creek

Ape Canyon stage
- andesite of Butte Camp

- Dacites from figure *B*
- Basalts from figure *A*

dacite is in equilibrium with a hornblende gabbro assemblage with 6–7 percent H_2O at 925 °C and 700–900 megapascals (MPa). Moreover, the crystallization path of this composition is remarkably similar to dacites of Mount St. Helens and the liquid line of descent converges on a pseudo-invariant point that explains the relatively constant composition. Gardner and others (1995) ascribed the textural and compositional diversity of Mount St. Helens dacites and andesites to mixing with mafic magmas in the dacitic reservoir, a point emphasized for the Kalama-period dacites and andesites by Pallister and others (1992), Carroll (2009), and Lieuallen (2010). Gardner and others (1995) noted the silicic nature of the Sugar Bowl-period dacite and suggested that it represents the silicic end-member in the mixing trends. Consistent with it being an end-member, Riker and others (2015) investigated a variety of degassing and decompression paths for a Sugar Bowl-period dacite and found that much of the textural diversity of this particular Mount St. Helens dacite can be explained without magma mixing.

Contrasting explanations for the origin of Mount St. Helens dacites have been proposed (Defant and Drummond, 1993; Berlo and others, 2004). Based primarily on high strontium/yttrium in dacites and location in the Cascades forearc, Defant and Drummond proposed that Mount St. Helens dacites are slab melts. However, they do not have the extreme strontium/yttrium generally attributed to slab melts, and many other origins for such adakitic rocks have been proposed. Thus, we suggest that the adakitic signature of Mount St. Helens dacites may be inherited from their gabbroic protolith through its generation by fractionation of garnet or amphibole from arc basalt.

Berlo and others (2004) modeled U-series disequilibria during partial melting of mafic lower crust. They showed that ^{226}Ra disequilibria required extremely rapid generation and ascent of silicic magma and (or) involvement of mantle-derived basalt less than a few thousand years old. Therefore, they preferred a crystallization of mantle-derived basalt as the origin of Mount St. Helens dacite.

Smith and Leeman (1993) addressed the origin of andesites at Mount St. Helens. They described two types of mantle-derived basalt, and a variety of andesites derived from them. As noted above, they pointed out that mineral-assemblage and trace-element-abundance constraints rule out generation of the andesite suite by either fractional crystallization or assimilation and fractional-crystallization processes. Instead, they proposed that the andesites were primarily derived by mixing between the mafic and silicic magmas.

Pallister and others (1992) reported the first comprehensive study of a single eruptive period. They built on the concept of the Hopson and Melson (1990) magmatic cycle and the Smith and Leeman (1987) model of magma mixing for andesite to produce a model for the origin of lavas erupted during the Kalama period. Their model explains the compositional cycle of dacite to andesite by intrusion and mixing of basalt into the magma, but does not explain the return to dacite compositions late in the Kalama period. Lieuallen (2010) analyzed a variety of phenocryst minerals in Kalama-period deposits in an attempt to refine the Pallister and others (1992) model. She confirmed the magma-mixing hypothesis in general, but also demonstrated that the path of magma evolution was more complex than that envisioned by Pallister and others (1992), as described in the Field Log section of this report (Day 2, Stop 12).

Two studies have found that recycling of crystals in the Mount St. Helens magmatic system is an important process. Cooper and Reid (2003) reassessed the $^{226}Ra/^{230}Th$ crystal ages of Volpe and Hammond (1991) for several Mount St. Helens samples. They found that, on average, crystals were as much as 2–4,000 years older than their eruption ages and proposed that a substantial proportion of crystals in the rocks had been stored somewhere in the magmatic system, probably as crystal mush, before being incorporated into younger erupted magma. Claiborne and others (2010) measured the ages in zircon crystals from several Mount St. Helens dacites with known eruption ages. None of the rocks contained zircon with ages equal to the eruption age; all were older. Moreover, all of the magmas were undersaturated in zircon. This means that zircons were inherited from older magmas or intrusions and were in the process of dissolving prior to eruption. Zircon chronology revealed that magmatism at Mount St. Helens extends back to about 500,000 years, about 250,000 years

Figure 15. Spider diagrams for Mount St. Helens rocks. Data consist of averages for each plotted unit and are normalized to primitive mantle of Sun and McDonough (1989). *A*, Basalts of Mount St. Helens. Most basalts are calc-alkaline with weak arc geochemical signatures although there is also a tholeiitic ocean island basalt type. Cave Basalt is also tholeiitic but lacks an arc signature and has lower incompatible-element abundances and higher heavy rare-earth element (HREE) abundances than the calc-alkaline basalts. Quenched basaltic inclusions are from early-Kalama dacite; basalt and basaltic andesite are lava and tephra from middle-Kalama set-X tephras. *B*, Dacites of Mount St. Helens. Dacites of all stages and periods have very similar parallel patterns. The shaded blue field is the superimposed range of the basalts from *A* (except for the Cave Basalt). Most incompatible-element abundances (especially the rare-earth elements [REE]) are higher than in these basalts, but uranium and thorium are similar. High field strength elements are more depleted than in the basalts and REE are slightly lower than in the basalts. *C*, Andesites of Mount St. Helens. Andesites of all stages and periods have similar parallel patterns. Andesites are more variable than the dacites, and they are more similar to Mount St. Helens dacites than basalts. The shaded blue and yellow fields are for the basalts (except the Cave Basalt) and dacites from *A* and *B*. Abundances of the most incompatible elements are similar to or slightly higher than in the basalts, but uranium and thorium are similar. High field strength elements are more depleted than in the basalts and REE are slightly lower than in the basalts.

older than any exposed Mount St. Helens rock, and, except in gabbroic inclusions derived from wall rocks, zircon derived from Tertiary or older basement is extremely rare in Mount St. Helens dacites.

Rutherford and others (1985) and Rutherford and Devine (1988) analyzed phase compositions and performed a series of experiments on the 1980 pumice. They determined that just prior to eruption, the 1980 magma was stored at about 920 °C and 220 MPa, contained about 4.6 percent H_2O, and had X_{H2O} of about 0.67. Using the Mount St. Helens crustal density column of Williams (1987), the 220 MPa determination is equal to a depth of 8.6 km. Gardner and others (1995) conducted phase equilibria experiments on samples of Wn tephra, and compared it with experimental results on pumices from 1980 and Yn tephra to infer a range in equilibration pressures (and depth equivalencies), temperatures, and X_{H2O} for the other major tephra layers (Ye, Pu, Bi, We, and T). The resulting ranges extend from depths of about 7 km to 12 km, from temperatures of 790 °C to 920 °C, and from X_{H2O} of 0.4 to 1.0. Cyclically zoned amphibole and hypersthene in the 2004–2008 dacite and a wide range in aluminum abundance in amphibole suggest that the central part of the crustal magma reservoir was actively convecting in a zone between about 5- and 10-km depth prior to the 2004 eruption (Rutherford and Devine, 2008).

Rutherford and Devine also investigated the rate of reaction-rim formation on amphibole phenocrysts from the 1980–1986 eruptions to determine ascent rates for magma rising through the shallow conduit system above the crustal reservoir at Mount St. Helens (Rutherford and Hill, 1993). These reaction rims form as a result of volatile loss during ascent and they suggest 6–10 days for magma to ascend from the crustal reservoir to the surface during the dome-building eruptions of 1980–1986. However, as noted below, Cashman (1992), Blundy and Cashman (2001), and Cashman and McConnell (2005) found textural evidence for multiple stages of shallow storage and decompression crystallization during ascent for these same eruptions.

Geschwind and Rutherford (1992) determined that cummingtonite in Mount St. Helens dacites of the Smith Creek period and older stages is stable only below about 800 °C at relatively low pressures (250–300 MPa in water-rich compositions [>6 percent]). Thus, the cummingtonite-bearing dacites of the early Swift Creek stage, the early Spirit Lake stage, and the Ape, Cougar, and Smith Creek periods (table 3) were generated in the uppermost, H_2O-rich, low-temperature parts of the Mount St. Helens reservoir system. These data, when combined with mapping of a seismically quiet zone (Scandone and Malone, 1985) and subsequent seismic tomography (Lees, 1992; Waite and Moran, 2009) and geodetic modeling (Lisowski and others, 2008, Mastin and others, 2009) suggest that the crustal reservoir system at Mount St. Helens has a strongly vertical aspect and extends from about 5-km to more than 12-km depth (fig. 16) as depicted in Pallister and others (1992, 2008).

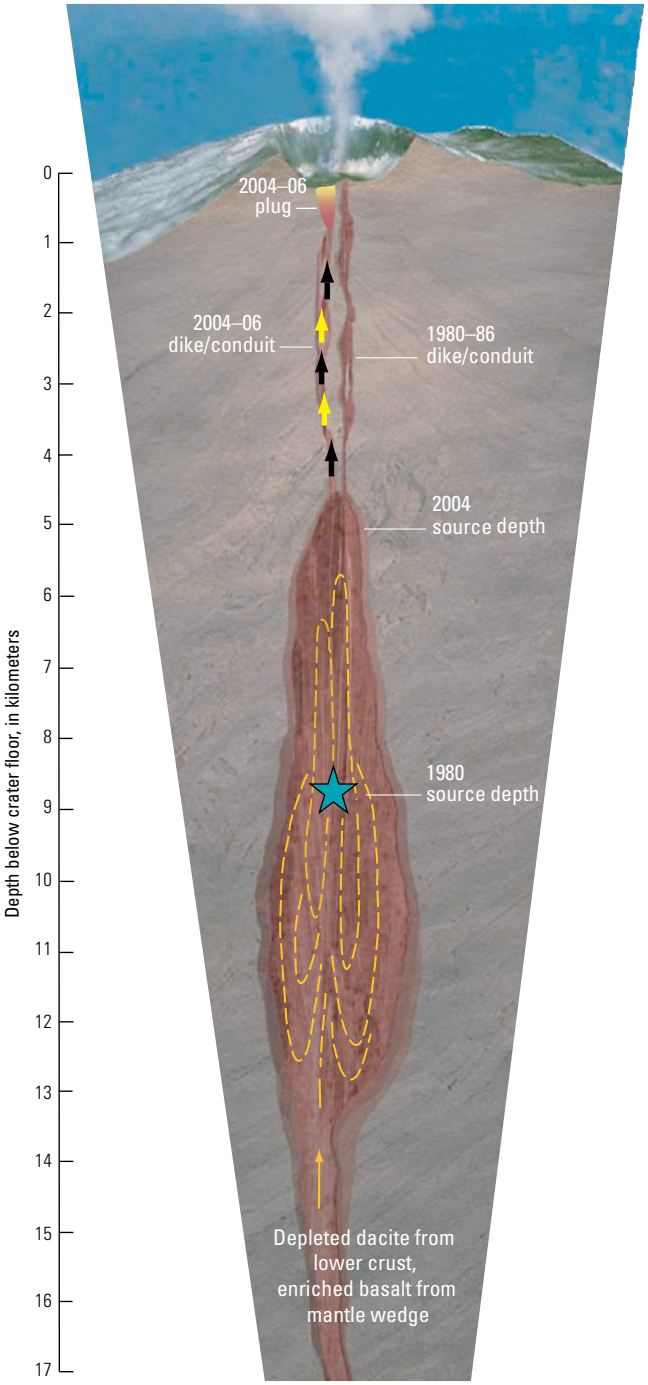

Figure 16. Schematic cross section of Mount St. Helens plumbing system, updated to include constraints from the 2004–2008 eruption. Yellow dashed lines are inferred convection paths in the reservoir (Rutherford and Devine, 2008) and are overlain by a stagnant crystal-rich mush zone considered the source for the 2004–2006 eruption. It is likely that the reservoir system is more complex than shown in this simplified diagram; for example, parts of the reservoir and conduit are probably dike-like and possibly aligned along the northeast-trending tensional axis of the Mount St. Helens pull-apart basin (fig. 2).

Summary of Eruptive History, Geochemistry, and Petrology

Mount St. Helens has an intermittent eruption history spanning at least 270,000 years that is divided into a series of stages (table 2). It exhibits periods of greater and lesser-to-no activity on a millennial to centennial scale. Mount St. Helens is dominantly a dacitic volcano, but includes a more mafic component. During the Ape Canyon stage (>35 ka, table 2), low-temperature, wet, quartz-hornblende and quartz-hornblende-biotite dacites dominated the erupted products. These eruptions were more widely spaced in time and more varied in composition than the dacite eruptions of the later stages. There is no evidence of mantle-derived magma contributing to the magmatic system at this time. As it aged, the Mount St. Helens magmatic system became increasingly organized so that mixing and interaction with residual or stored dacite and mantle-derived magma became typical. The earliest known basalts are from the Cougar stage (28–18 ka), and andesites became an increasingly substantial component of the erupted magmas during the Spirit Lake stage.

Mount St. Helens silicic magmas were most likely generated from Tertiary pyroxene-hornblende gabbro 21–27 km deep in the lower crust. They are water rich to saturated at about 925 °C at this depth. The dacite was probably generated rapidly and ascended to the subvolcanic magma reservoir system, where it underwent mixing with crystal mush and residual magma before ascending to even shallower parts of the reservoir system at about 5–12-km depth. There, it underwent further evolution to produce the array of dacites erupted at Mount St. Helens. Interaction with mantle-derived mafic magmas produced the array of andesites erupted at Mount St. Helens. Occasionally, basalt circumvented or ascended through the felsic magmatic system and erupted relatively unevolved. Detailed studies of Mount St. Helens 1980–1986 and 2004–2008 dacites have greatly improved our understanding of shallow magmatic degassing and crystallization of silicic magmas and the effects of these processes on monitoring data, eruption dynamics, and explosivity.

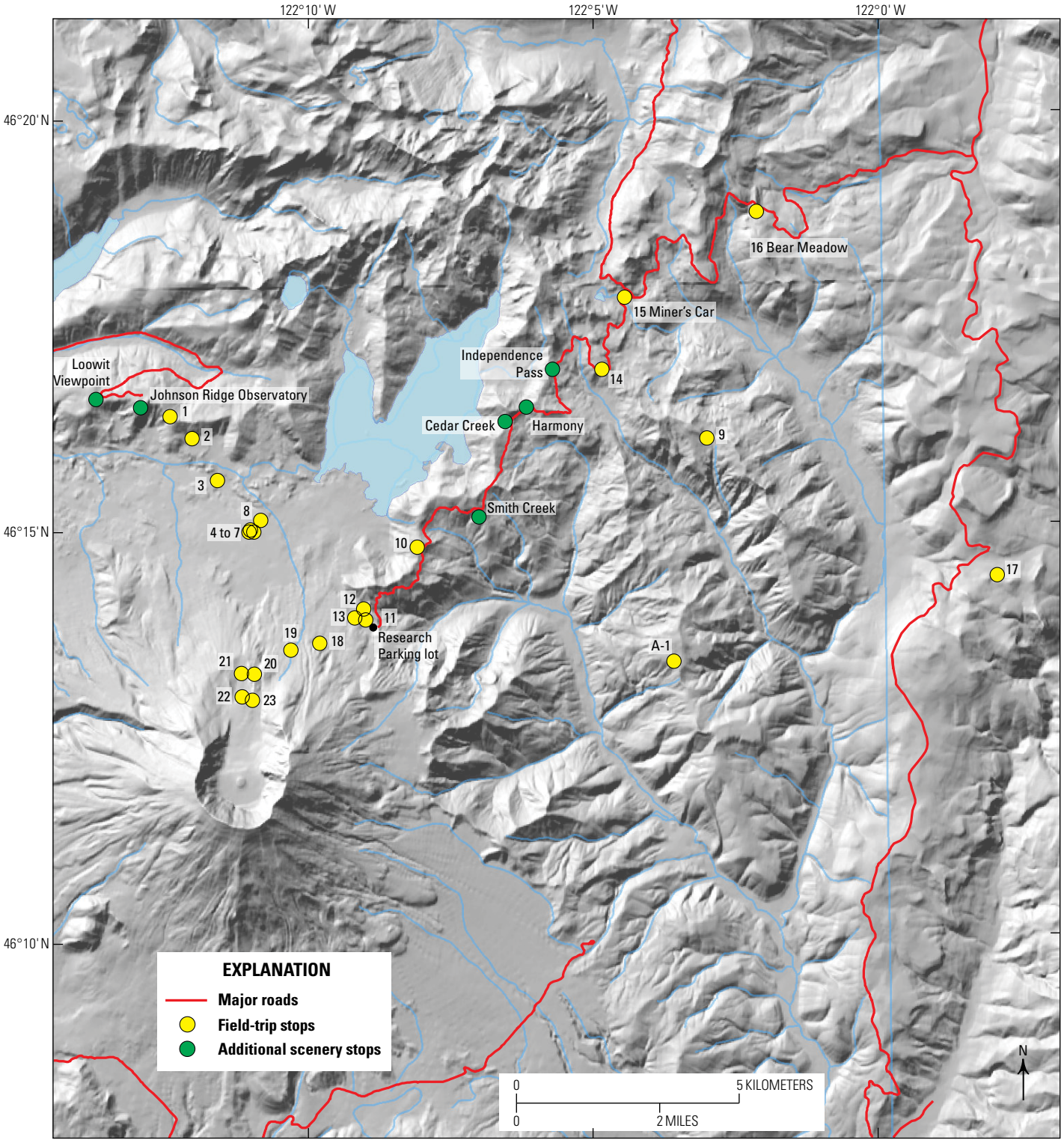

Figure 17. Shaded relief map of Mount St. Helens and terrane to the north and east. Stop 9 is the Mount St. Helens Institute campsite. JRO, Johnston Ridge Observatory.

Field Log

Vehicle distances are in miles, hiking distances are in meters, and coordinates are based on the WGS84 datum. An index map (fig. 17) shows the localities of the major stops in this field-trip guide.

Day 0: Drive from Portland/Vancouver to Castle Rock, Washington

In order to get an early start to the hike on day 1, during the late afternoon of the day before we drive from Portland, Oregon, to Castle Rock, Washington, where we spend the night at the Mount St. Helens Motel.

Day 1: 1980 Pyroclastic-Flow Deposits

By James W. Vallance,[1] B. Peter Kokelaar,[2] and Alexa R. Van Eaton[1]

This trip begins at Castle Rock, Washington. From the Portland, Oregon–Vancouver, Washington, area, drive north on U.S. Interstate 5 (I-5) to Exit 49 in Castle Rock, Washington. Mileage begins at the end of Exit 49 off ramp as you turn east onto Washington State Route 504 (SR-504).

We depart the motel at 6:00 a.m. Please leave your room keys in the box by the lobby.

The drive to Johnston Ridge Observatory takes about 1 hour.

0.0 Proceed east on SR-504, following the signs to Johnston Ridge Observatory. En route you will pass several visitor centers and Silver Lake (at 6.0 miles), which was impounded by lahars following two debris avalanches during the late Pine Creek period (assuming lake breakout shortly after the younger debris avalanche, the age of both lahar deposits would be 2,590±120 years B.P. [Hausback and Swanson, 1990; Hausback, 2000]). In addition, you pass the town of Toutle (~10 miles) and a gift shop with an A-frame house that was partly buried in 1980 by lahar or hyperconcentrated flow (19.2 miles)

20.9 Pass the access road for the Sediment Retention Structure (SRS), which was built after the 1980 eruption to limit the downstream transmission of sediment from the 1980 deposits in the Toutle and Colombia Rivers. Views of the Toutle River upstream of the SRS reveal the sediment-choked braided river, which still transports an order of magnitude more sediment than prior to the eruption (Major and others, 2000).

29.2 Just before the bridge, you enter the 1980 blast zone, which was planted with a forest after the 1980 eruption.

45.2 Take the ramp to the right to bypass the U.S. Forest Service (USFS) Science and Learning Center and continue toward Johnston Ridge Observatory.

47.0 Pass the entrance on the left to Coldwater Lake, a large lake impounded by the 1980 debris-avalanche deposit.

47.2 Pass the entrance to the Hummocks Trailhead (which provides a wonderful loop hike through the 1980 debris avalanche). As you continue up the road along Coldwater Creek, notice the debris-avalanche deposits that fill the valley floor. The debris avalanche flowed over the summit of Johnston Ridge at the headwaters of the valley and flowed part way down the canyon. Notice also the bare hillsides above the valley. The 1980 blast swept this area, as well as much of the terrain en route to here, downing the forest.

51.0 Cross Coldwater Creek near the head of the valley and the outlet of the Spirit Lake tunnel. The tunnel was constructed by the U.S. Army Corps of Engineers following the 1980 eruption (completed in 1985) to prevent a breakout of Spirit Lake and downstream flooding of the Toutle River. The May 18, 1980, debris-avalanche and pyroclastic-flow deposits blocked the natural exit of the lake and raised its elevation by 64 m, increased its surface area from 1,300 to 2,200 acres, and decreased its maximum depth from 58 to 34 m.

52.5 Arrive at Johnston Ridge Observatory. Park in the northeast corner of the lot (near the trailhead) and prepare for a 15-km day-long hike. Restrooms are available just inside the entrance to the visitor center. We will not be stopping at the visitor center on this field trip—there is a mid-conference trip that includes a stop there.

8:15 a.m. Exit the parking lot at the northeast corner and take the Boundary Trail (#1) to the east along the crest of Johnston Ridge.

Additional stops as shown today are off trails and require special permission from the USFS National Monument. To prevent damage to the sensitive environment, we do not provide a hiking guide to these localities. We only provide coordinates and an index map (fig. 18) for the locations we will visit.

[1]U.S. Geological Survey.

[2]University of Liverpool.

Future users of this guide are instructed to contact the National Monument for off-trail access.

Hike from Johnston Ridge Observatory to Stop 1

Head east along the Boundary Trail that follows Johnston (or Coldwater) Ridge. May 18, 1980, blast deposits as thick as 1 m covered this Tertiary bedrock ridge. Much of the blast deposit is now eroded and washed off these slopes. Nonetheless, remnants of the blast are abundant. Especially notable are numerous medium-gray microvesicular dacite fragments that are the juvenile component of the blast deposit. These rocks formed when the debris avalanche suddenly removed about 1 km of rock from the cryptodome that had been growing within the upper edifice of Mount St. Helens since late that March. This loss of overburden caused the catastrophic decompression of the cryptodome magma body and generated the laterally directed pyroclastic density current that is now known simply as the lateral blast. The hot incompletely degassed parts of the cryptodome not only released the gas that drove the eruption but also formed small vesicles that are visible in the light-gray blast dacite. Less common dark-gray to black nonvesicular dacites have the same composition as the light-gray (microvesicular) blast dacite. Before the lateral blast, the darker (nonvesicular) dacites were completely degassed parts of the magma body that had formed the cooling and solidifying margin of the cryptodome.

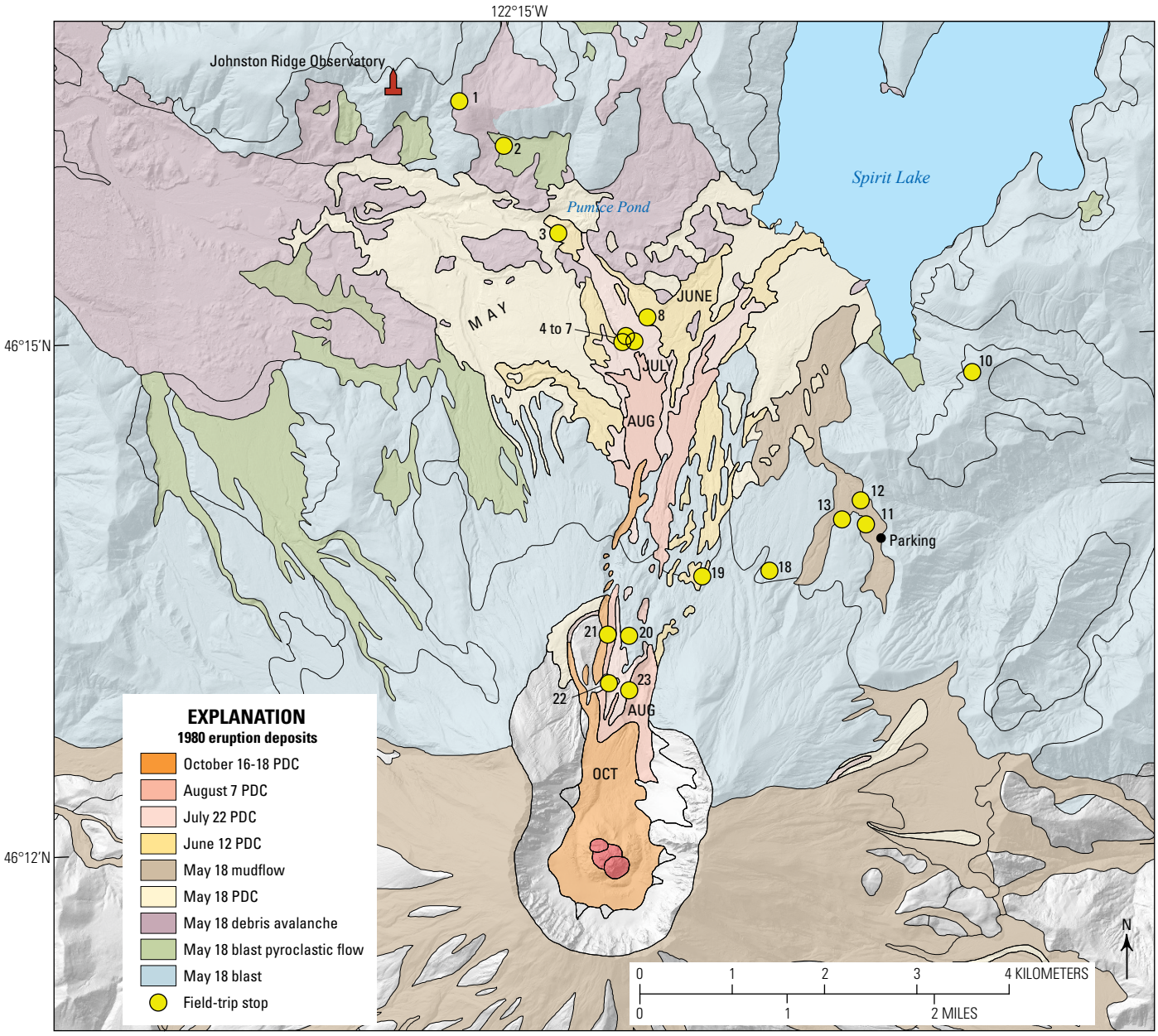

Figure 18. Geologic map showing deposits from the May 18, 1980, eruption and the following summer and fall. Considerable erosion and eruption of the 2004–2008 lava dome have changed the distribution patterns shown here. PDC, pyroclastic density current.

Stop 1: Debris-avalanche and blast deposit atop Johnston Ridge (along the Boundary Trail that descends from Johnston Ridge Observatory) (lat 46°16′23.91″ N., long 122°12′30.84″ W.)

The debris avalanche overtopped Johnston Ridge here and descended into South Coldwater Creek valley to the north (fig. 18). The slopes along the trail to the west are covered by a thin veneer of blast deposits as scattered patches overlying Tertiary bedrock. To the east along the trail is the debris-avalanche deposit, several meters thick and composed chiefly of a heterolithic mixture of Mount St. Helens rocks that vary in size from pebbles to boulders and in composition from basalt to dacite. The view north reveals debris-avalanche deposits coating the slopes of South Coldwater Creek valley. In contrast, the view southwest reveals steep and bare Tertiary bedrock slopes (fig. 19). The debris avalanche ran up high on this slope and scraped the surface clean of vegetation and all loose soil and rock debris. To the south, the debris-avalanche deposit forms a varicolored irregular surface in the Toutle River valley bottom.

The flat terrace at the base of the steep slope to the south is underlain by the blast pyroclastic-flow deposit first described in Hoblitt and others (1980). These deposits formed when loose, hot blast deposits remobilized on steep slopes, coalesced, and flowed into valleys to form flat-topped deposits many meters thick. The deposits below were actually emplaced by flows that moved southward, opposite to the overall direction of the lateral blast (northward here). To the northwest, deposits that form the flat-floored bottom of South Coldwater Creek had the same origin, owing to late-stage remobilization of the blast deposit.

Light-colored deposits that form another terrace to the east in the Toutle River valley are from the pumiceous pyroclastic flows of the afternoon of May 18 (fig. 19). Continuous Plinian eruption during the afternoon of May 18 generated multiple pyroclastic flows. These flows filled the area directly north of the amphitheater to depths of 40 m or more, forming a flat terrace that sloped a few degrees northward and became known as the Pumice Plain.

Stop 2: Secondary blast and accretionary lapilli-bearing fall deposits south of Johnston Ridge (lat 46°16′08″ N., long 122°12′09″ W.)

Secondary blast pyroclastic-flow deposits form this terrace, and the area is framed by steep bedrock hillslopes to the northeast and west. Terminology of blast-related deposits is given in table 3. The debris-avalanche deposits crop out just south of

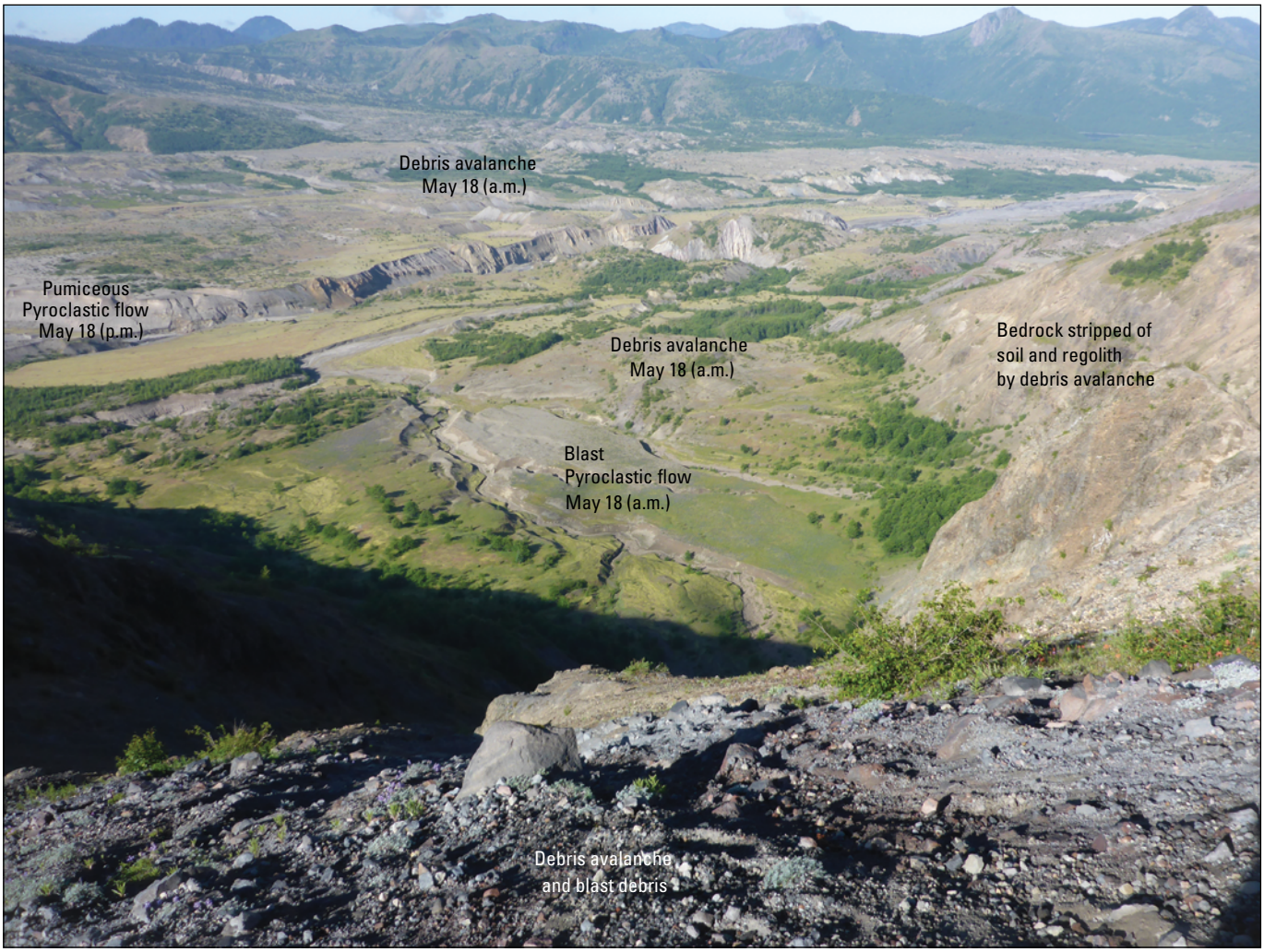

Figure 19. Photograph of lower part of Pumice Plain from Boundary Trail along Johnston Ridge.

Table 3. Terminology of blast deposits by various authors.

Hoblitt and others (1981)	Moore and Sisson (1981)	Waitt (1981)	Fisher and others (1987)
Directed blast deposit	Pyroclastic surge deposit	Pyroclastic density flow deposit	Laterally directed pyroclastic surge (or "blast surge")
Accretionary-lapilli-bearing unit	Air-fall unit	Sandy silt facies (A3)	Blast fallout deposit (A3)
Blast pyroclastic-flow unit	Secondary pyroclastic-flow unit	Not discussed	Secondary blast flow (A2*)
Pyroclastic-surge unit	Fine upper unit	Fine sand facies (A2b)	Blast surge deposit (A2)
Massive unit	Fine upper unit	Coarse sand facies (A2a)	Blast surge deposit (A1)
Basal unit	Coarse basal unit	Basal gravel unit	Blast surge deposit (A0)

here (fig. 18). On May 18, after emplacement of the debris avalanche and development of the lateral blast, the ground-hugging currents traveled up Johnston Ridge, coalesced, then drained back down its steep slopes and ponded here. The deposit is a few meters thick, grayish brown, and poorly sorted. This reflects mixing of the blast-derived material as it gravitationally cascaded back down the steep surrounding slopes.

The overlying, well-preserved blast ash fall (~2 cm) lofted from the blast pyroclastic density current, rose into the stratosphere, and fell as accretionary lapilli by about 9–9:30 a.m. Therefore, reworking of the blast pyroclastic density currents must have occurred within this period (but was likely synchronous with deposition of the blast density current). Accretionary lapilli in the blast ash fall are as much as 1 cm diameter and reasonably well preserved here, with concentric internal layers. This raises an interesting question about how they formed. Coherent aggregates require abundant moisture to grow (water–ash ratios of about 0.2; Van Eaton and others, 2012), suggesting that the co-blast ash clouds contained plenty of water. This moisture may have been sourced from the groundwater hydrothermal system in the volcano, as well as from snow and glacial ice scoured by the eruption.

Pumiceous pyroclastic flows during the afternoon of May 18 emplaced a thin layer (~13 cm) of fine-grained elutriated ash on the terrace (fig. 20). The currents were likely dilute and low energy by the time they were emplaced here. Subsequently, the May 18 pyroclastic-flow deposits interacted with water, causing phreatic eruptions and forming a large explosion pit just ~1 km south of this site (the pumice pond). Low-angle cross-stratified ash deposits from the phreatic explosions drape the terrace here. Observations from a USGS overflight around 6:00 p.m. on May 18 show this explosion pit and continuing eruptions from it, thus constraining the emplacement of the phreatic surge deposits.

Stop 3: Pumice pond (lat 46°15′37″ N., long 122°11′42″ W.)

"Pumice pond" refers to the largest of many phreatic explosion pits that were created in the pumiceous pyroclastic-flow deposits of May 18, 1980 (Lipman and Mullineaux, 1981, pl. 1). Rowley and others (1981) referred to this feature as the "big phreatic-explosion pit." It originally measured as deep as 38 m, but did not excavate through to the base of the May 18 pyroclastic-flow deposit. When the pit was later partially filled by the pyroclastic-flow deposits from the June 12, 1980, eruption, it became known as the pumice pond. The June pyroclastic-flow deposits are not commonly pink in color, except within the pumice pond. At this stop, clast-rich distal facies of June pyroclastic density current deposits are pink to gray in color (fig. 21). Overlying the June pyroclastic-flow deposits are well-bedded fine-grained sediments produced during the 1980–1981 and 1981–1982 rainy seasons. At the top of the section lies a massive lahar deposit created on March 19, 1982, when an explosion caused rapid snowmelt and production of a transient lake around the lava dome. Rapid discharge from this lake produced a lahar that traveled down the north flank of Mount St. Helens and into the North Fork of the Toutle River (Waitt and others, 1983), filling the top of the pumice pond depression.

Stops 4–8 Summary

The next four stops focus on surface, sedimentologic, and depositional characteristics of pyroclastic-flow deposits emplaced on June 12 and July 22, 1980. These were chosen for detailed study because simple two- and three-pulse eruptions generated them, their surface features are well preserved, and subsequent erosion has incised them and exposed continuous near-vertical cross sections of the deposits. Their simple emplacement history means we can separate and correlate the deposits of individual eruptive pulses from place to place and thereby more readily interpret their origins. The resultant deposit architecture is less complex than architectures of continuously aggraded and multi-pulse pyroclastic depositional systems would be, and the simple architecture facilitates interpretation of emplacement mechanisms that might otherwise be difficult to fathom. Examination of June 12 deposits will emphasize (1) the overall emplacement trend from widespread and thin to confined by levees and (2) the remobilization of primary deposits by means of piecemeal retrograde failure to form fines-deficient secondary deposits and scallop-and-mesa topography. Our examination of July 22 deposits will focus on depositional trends during eruptive sequences, simple lobe and levee formation, surface wave generation as it relates to stacking of multiple deposits during deposition of a single flow pulse, and formation of complex digitate deposit termini.

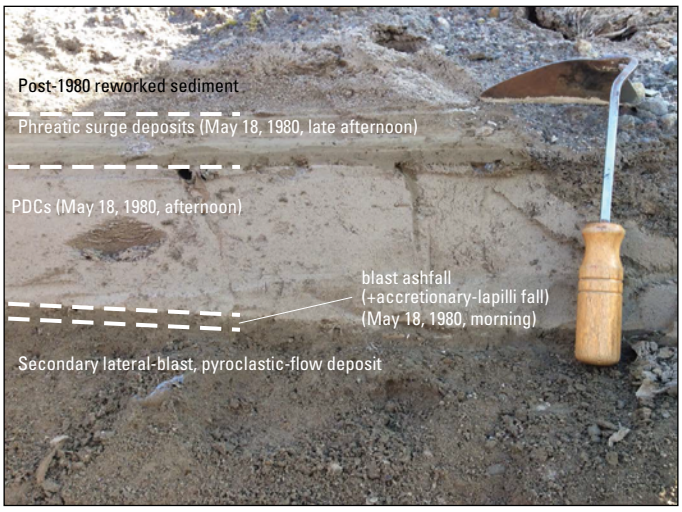

Figure 20. Photograph of section from surface through secondary pyroclastic-flow deposit of the lateral blast. Secondary pyroclastic-flow deposit coalesced from laterl-blast-surge debris, remobilized, and flowed off steep, surrounding hill slopes.

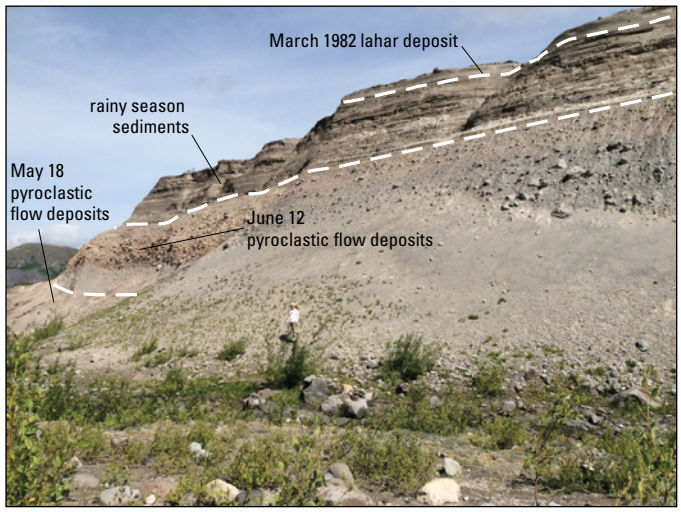

Figure 21. Photograph showing deposits at the site of the Pumice Pond.

Stop 4: Mathematicians' gully (lat 46°14′59.28″ N., long 122°11′8.95″ W.)

Mathematicians' gully is informally named in honor of University of Manchester mathematicians, whom geologists convinced to take a lot of tedious sedimentologic field measurements. The gully system now slices through a sequence of May 18, June 12, and July 22, 1980, pyroclastic flow deposits (figs. 22, 23). The overview from the west edge of Mathematicians' gully shows a stacked sequence of 1980 pyroclastic-flow deposits emplaced on July 22, June 12, and May 18 in the gully wall to the east (fig. 21). Studies in progress by Kokelaar, Vallance, and Gray focus on eruptions of June 12, July 22, and August 7 because the source vent produced simple 1–3-pulse pyroclastic events during their deposition, which, unlike the complex multiple-stage series of pyroclastic flows of the May 18 eruption, are easier to interpret. Ongoing work includes three modes of investigation: (1) analysis of vertical and oblique aerial photos, (2) field investigation of deposits conducted during three field campaigns, and (3) appropriate laboratory-based experiments that use analogue materials to simulate processes responsible for deposition of the deposits. This fieldtrip focuses on field study, chiefly of June and July sequences, includes some photographic analysis, and alludes to experiments.

Critical facts associated with the June 12, 1980, pyroclastic flows are summarized in table 1 and as follows:

- The initial eruption on June 12 at 7:05 p.m. cleared the vent to produce minor ash fall but included no pyroclastic flows.
- The Plinian column erupted on June 12 at 9:11 p.m. initiated the production of pyroclastic flows.
- The flows poured off the steps sloping 10–15° below the mouth of the amphitheater and flowed across the relatively flat May 18 pyroclastic-flow surfaces of the about 15-km^2 Pumice Plain, which sloped gently northward at 2 to 7 degrees.
- Outcrops illustrate that the eruption produced at least two separate primary flows and a secondary remobilization flow on the Pumice Plain (fig. 24). Smaller flows, if any, apparently were confined to the floor of the amphitheater and the steps area.
- It appears that the secondary flow is interbedded between the two primary flows (fig. 24).

Figure 22. Oblique aerial photograph of the Pumice Plain taken in August of 1980 showing the Mathematicians' gully area bounded in red. Gray areas are June 12 pyroclastic-flow deposits; cream-colored areas are July 22 and August 7 deposits. Photograph illustrates how early July flows spread widely, whereas late July flows were confined to lobe and levee systems. Preserved deposits in this area are from May, June, and early, middle, and late July.

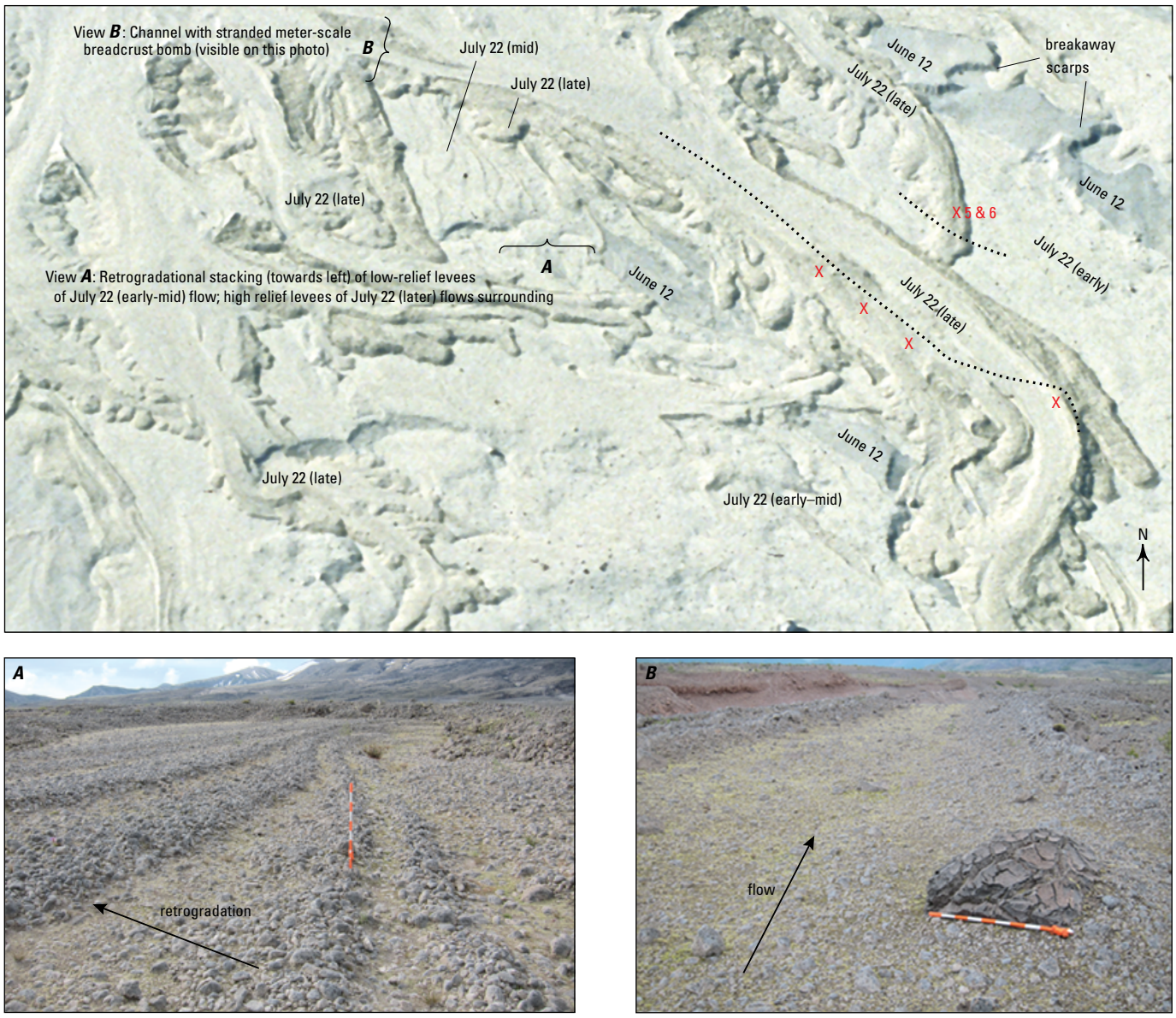

Figure 23. Oblique aerial photograph from August 1980 of the Mathematicians' gully area. Black dotted lines show approximate location of present-day gully walls. Red X's (labeled 5 and 6) are sites for detailed study. *A*, Photograph taken in 2010 of field of retrograde levees in mid-July deposits. *B*, Photograph taken in 2012 of leveed feeder channel in late July deposits. Canyon exposures reveal May, June, and early- and late-July ignimbrites.

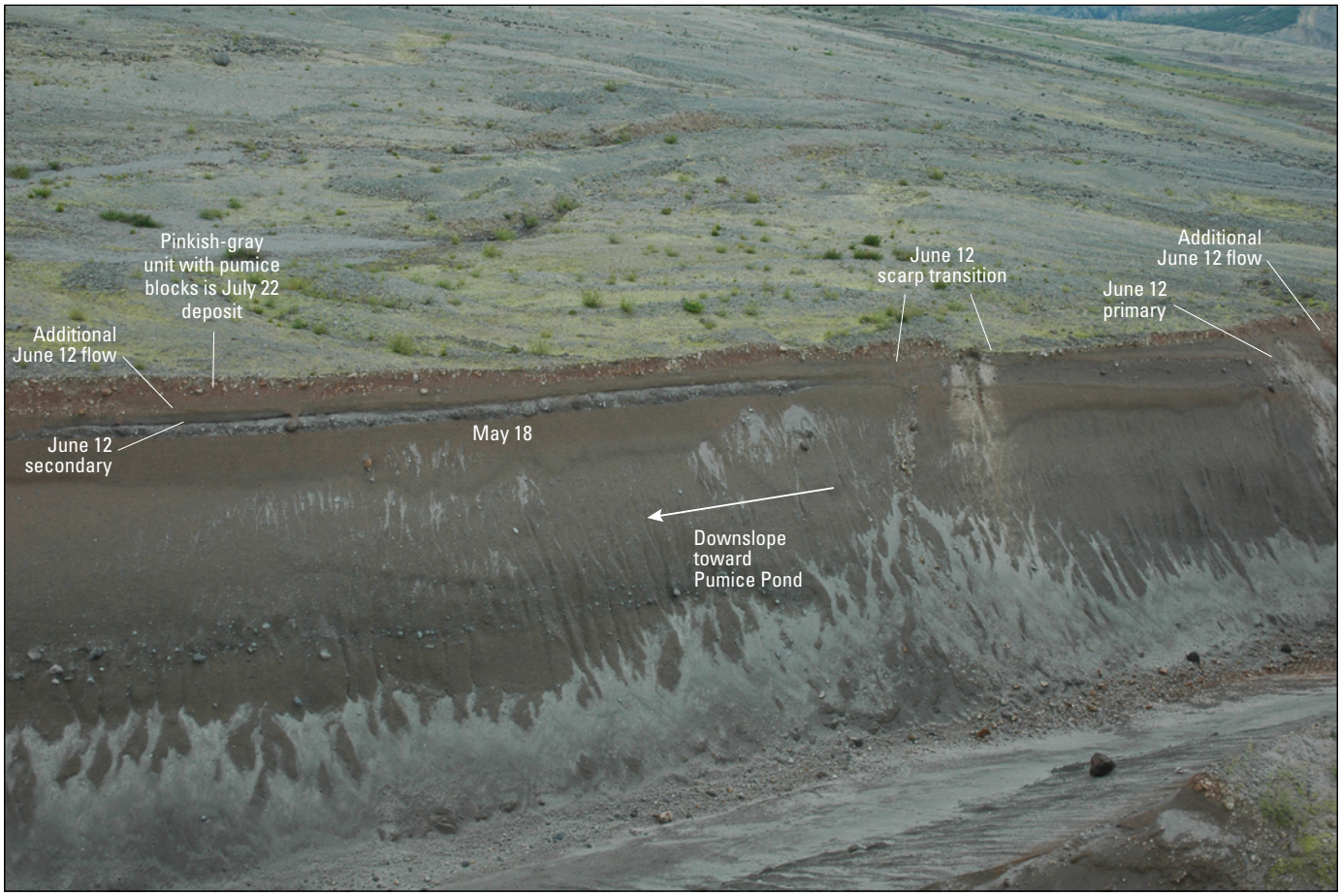

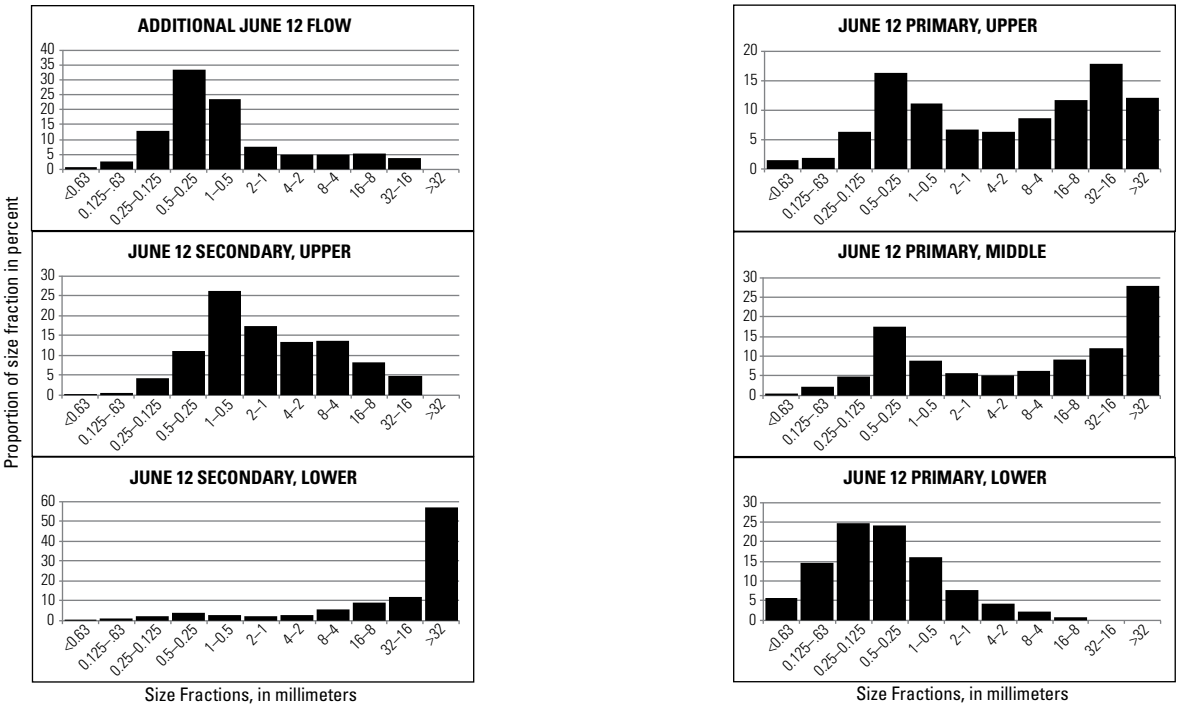

Figure 24. Photograph illustrating cross section of pyroclastic-flow deposits exposed along the east wall of Mathematicians' gully. The photograph was taken from near sites 5 and 6 shown in figure 23. July 22, June 12, and May 18 pyroclastic-flow deposits are exposed. A breakaway scarp is preserved in the June 12 deposits.

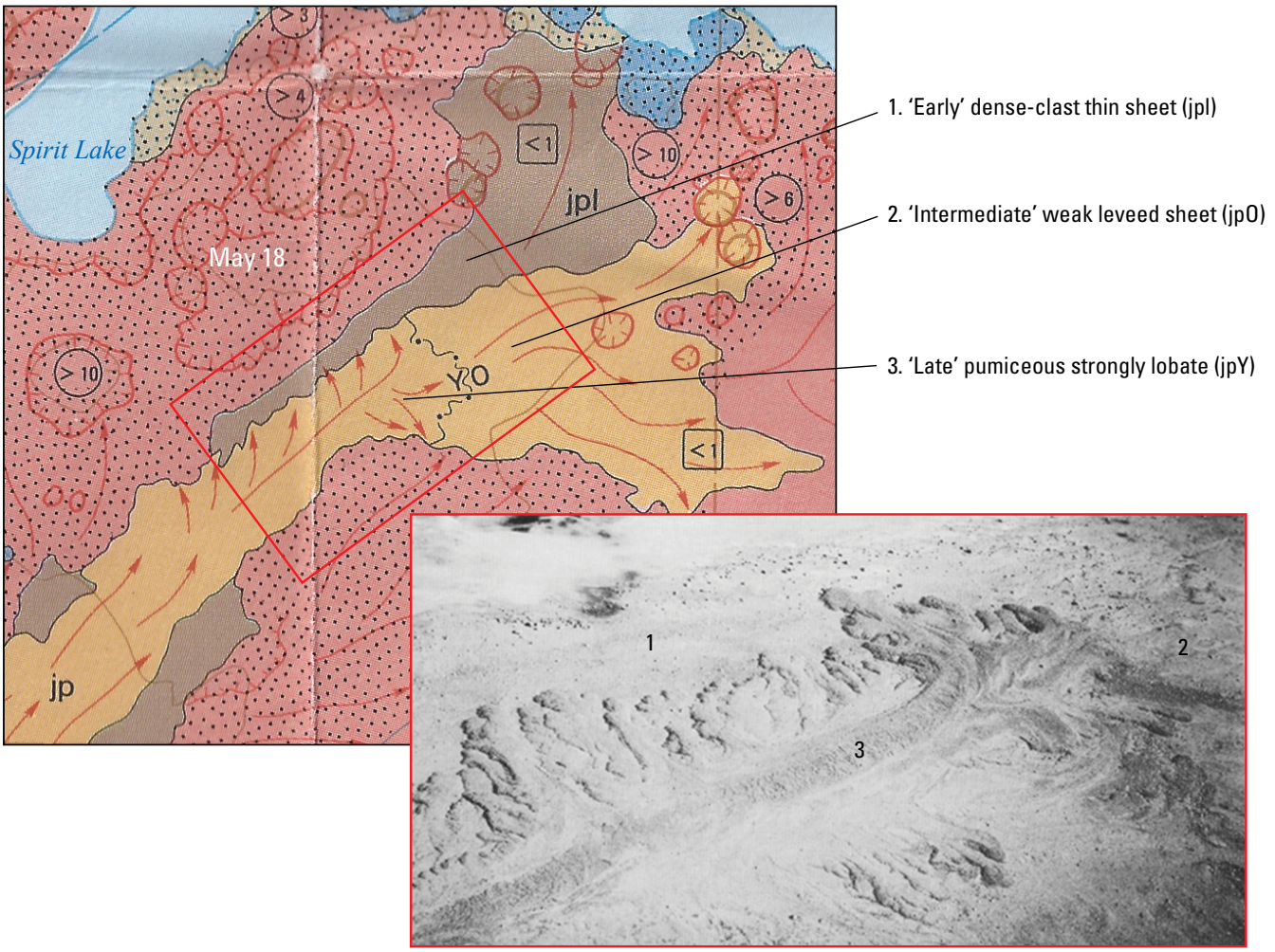

Figure 25. Excerpt of geologic map from Kuntz and others (1990) near Spirit Lake (note lake at top of map) and photograph illustrating flow and deposit evolution in June 12, 1980, flows near the northeast termination of this deposit. Stages include early thin-sheet deposits; intermediate weak-levee deposits; and late, pumiceous, lobate deposits. Erosion and subsequent deposition have destroyed some of these deposits since mapping. Red box shows the area of the photograph at lower right. "May 18" indicates PDC deposits of May 18, 1980; Dark blue area shows exposures of May 18 debris avalanche deposit. Symbols "jp" and "jpl" indicate pyroclastic-flow deposits and pyroclastic-flow lag deposits of June 12. Y and O designate the younger and older sides of a contact (indicated by black line with dots) between flows deposited on June 12. Numbers in circles indicate thicknesses of May 18 deposits in meters; numbers in squares indicate thickness of June 12 deposits in meters. Brown arrows show flow directions; circles with hachures delineate secondary explosion craters; irregular line with hachures shows break-away scarp.

- Like other eruptive sequences (July and August), the June flows initially spread more widely then became progressively more lobate and channeled (fig. 25).
- The June flows poured into the big phreatic explosion pit to form the pumice pond (fig. 21).
- The flows initially formed metastable deposits that later remobilized by piecemeal retrograde failure to form an unusual scallop-and-mesa topography delineated by sinuous breakaway scarps (fig. 26).
- A dome formed at the vent at the end of the eruption.

A cross section of a buried June 12 breakaway scarp crops out in the wall of Mathematicians' gully to the east (fig. 24). Superposition of a 1980 map of the June 12 pyroclastic flows (and scarps) (Kuntz and others, 1990) onto present topography confirms that one of these breakaway scarps intersects the east wall of the gully at an oblique angle. Upslope are primary June 12 deposits, but downslope a buried break in slope shows the transition from the lower primary flow to the remobilized secondary flow. The primary flow deposits are enriched in fine-grained components, are compact, and exhibit basal inverse grading. The remobilized flow is poor in fine-grained components, extremely friable, and normally graded. Efficient elutriation of fine-grained components apparently accompanies the piecemeal retrograde remobilization process. The June 12 initial explosions excavated a vent through dense dome lava within the crater; hence, pyroclastic-flow deposits from June 12 deposits contain denser lithic clasts than those of July and August. We will revisit this topic and discuss it in

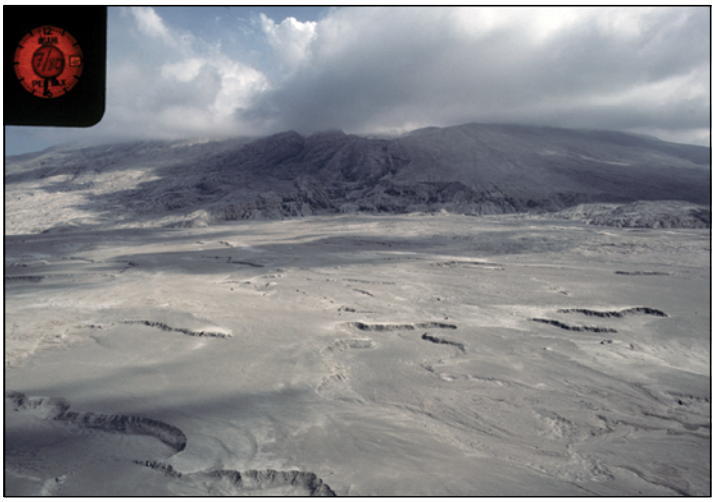

Figure 26. Aerial photograph of June 12, 1980, pyroclastic-flow deposits taken shortly after June 12. Note mesa-and-scarp topography on surface of June 12 deposits. Sinuous scarps are entirely formed in deposits of June 12 where slopes were 2–7°owing to piecemeal breakaway and remobilization of primary June 12 pyroclastic-flow deposits as secondary flows. Breakaway occurred both during and shortly after the June 12 ignimbrite emplacement, in which case secondary fine-grained ash deposits formed near the scarps. The scarps could then trap the coarse, dense bedload of successive currents. Upstream of the June terminations, the fines-enriched top of the ignimbrite is distinctive and coarse levees are not apparent. Huge bedload boulders, dense and commonly 3–4 m in diameter, crop outlocally.

more detail where the scallop-and-mesa topography of June 12 is exposed at Stop 8.

Key facts associated with the July 22, 1980, pyroclastic flows and their deposits are summarized as follows:

- At 5:14 p.m., a 6-minute eruption formed a vent through the June 12 dome lava and caused a small flow confined to the amphitheater.
- At 6:26 p.m., a second eruptive outburst lasting less than 10 minutes formed pyroclastic flows that moved 6.5 km toward Spirit Lake.
- At 7:01 p.m., a third eruptive outburst lasting less than 10 minutes formed pyroclastic flows that moved 7 km to the upper end of the pumice pond (fig. 27).
- The flows forked into east and west branches (fig. 28). The west branch was the source of the deposits in Mathematicians' gully. The east branch deposits were destroyed by lahars of March 19, 1982.
- The flows spread more widely initially then became more lobate and channeled, with channels bounded by prominent levees rich in pumice blocks (fig. 22).
- In the Mathematicians' gully area, prominent lobe and levee features originated from a late-stage feeder channel (fig. 23).
- Logged sections are noted in figure 24. The cross sections across the gully to the east cut across lobes that broke away from the main channel that followed what is now the axis of the gully.
- In outcrop across the gully, the July 22 deposits have a strong pinkish tint and exhibit concentrations of blocky rounded pumice (figs. 29, 30, 31). Finer grained channel fill crops out adjacent to an asymmetric pumice-block

Figure 27. Aerial photograph of the July 22, 1980, pyroclastic eruption taken shortly after the second eruptive event at 6:26 p.m. Fountaining plume fed lobate pyroclastic flow that was moving out of the amphitheater. Photograph by James Vallance, U.S. Geological Survey.

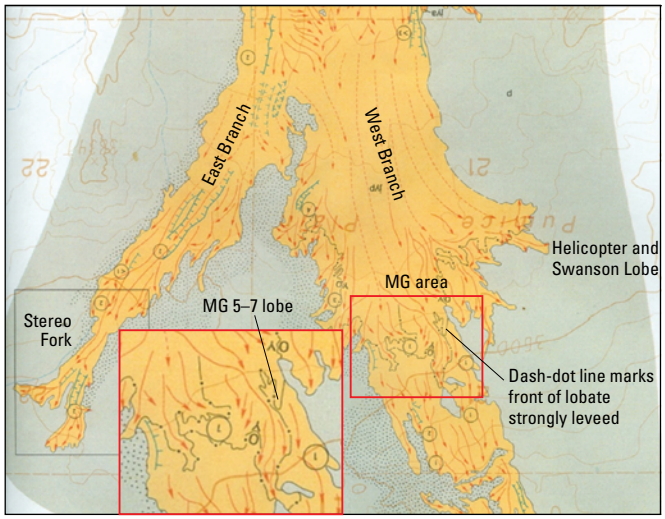

Figure 28. Excerpt of geologic map from Kuntz and others (1990) showing the July 22 pyroclastic flows in the Mathematicians' gully area (MG) as well as the location of this on the MG 5–7 lobe.

mound (fig. 30*A*). Evidence of two July 22 pyroclastic flows shows where a low-relief pumice-clast bedform underlies continuous channel fill of the upper flow deposits (fig. 30*B*). Elsewhere, the lower of the July flow deposits is thin and contains a dearth of coarse pumice blocks (fig. 30). We interpret this thin layer as a deposit of the early stage "spready" flow of the July sequence.

Stop 5: Feeder channel for late-stage flows of July 22 (lat 46°14′57.20″ N., long 122°11′02.48″ W.)

This late-stage channel is the source of many blocky flow lobes that have been mapped and exposed in outcrop downslope of here (fig. 32). Large low-density blocks border the channel and form the lobe margins. These coarse pumice blocks preferentially move to the top of moving pyroclastic flows. The mechanism by which the pumices unmix is a combination of inverse size segregation and density segregation. Because the particles at the flow top move faster than flow fronts, they migrate to the front and margin of the flows much like coarse grains in the debris flow experiments of Johnson and others (2012) (fig. 33). Coarse-grained flow margins are more permeable and more easily release fluidizing gas than the more fluid, fines-enriched flow interiors. Coarse-grained flow margins thus form flow perimeters that are more resistant to flow than fines- and gas-enriched flow interiors. The numerous lobes formed when pulses of pyroclastic flow broke out of channel confines. Jams, owing to downstream slowing or deposition and pulses that exceed channel margins, are causes of flows breaking away from channel confines.

As flow in a channel finally wanes, its more fluid interior drains away and sharpens levees from the inside out (fig. 34) (Kokelaar and others, 2014). The inner walls of such channels collapse or are eroded as flows wane. Inner wall removal may proceed piecemeal from the inside until the coarse-grained

Figure 29. Panorama photographs from left to right (*A* to *B* to *C* to *D*) showing continuous cross-sectional exposure of July 22 deposits in east wall of Mathematicians' gully.

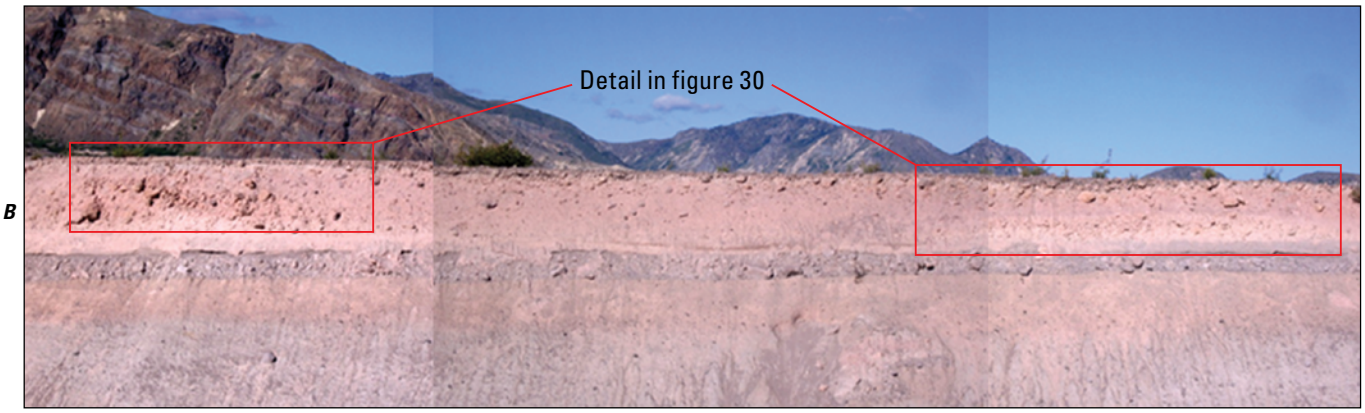

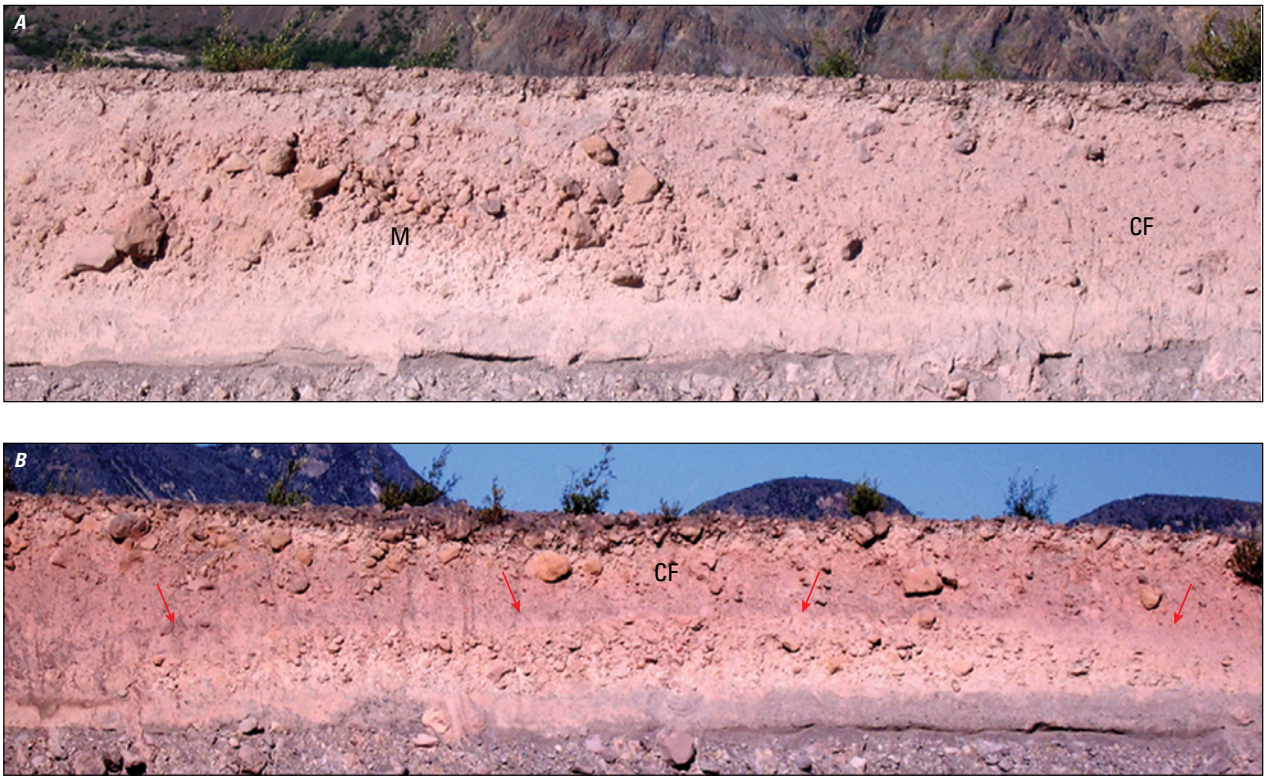

Figure 30. Photographs taken at Stops 4–7 showing detail from figure 29. *A*, Contrast between asymmetric pumice-block mound (M) and channel fill (CF). *B*, Buried, low-relief, pumice-clast bedform highlighted by arrows. Pumice-clast bedform grades laterally to "spready" early July deposits (see fig. 31). Late-stage channel fill continuously overlies the bedform.

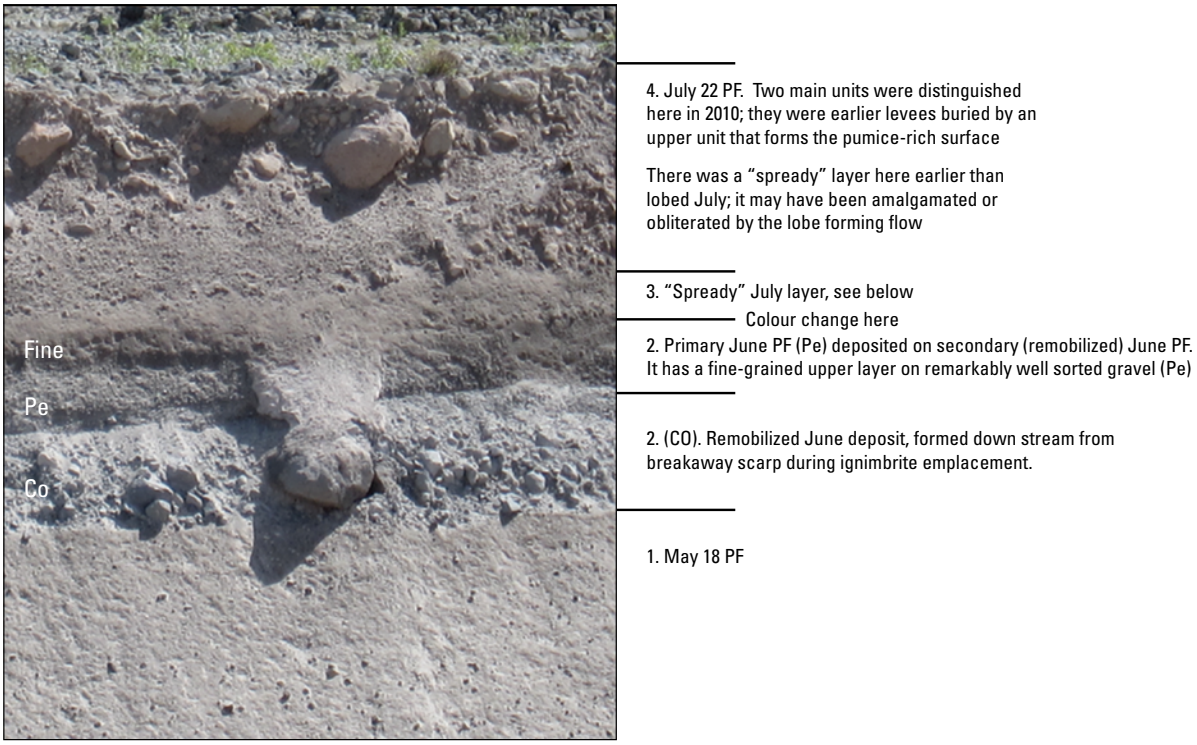

Figure 31. Photograph showing detail of Mathematicians' gully section from outcrop of 1980 deposits along the east wall. Location of section is shown in figure 32. PF, pyroclastic flow. Key questions to consider: How does the remobilized deposit (Co) compare with its counterpart upstream of breakaway? How much of it is the early primary deposit? Is it all remobilized?

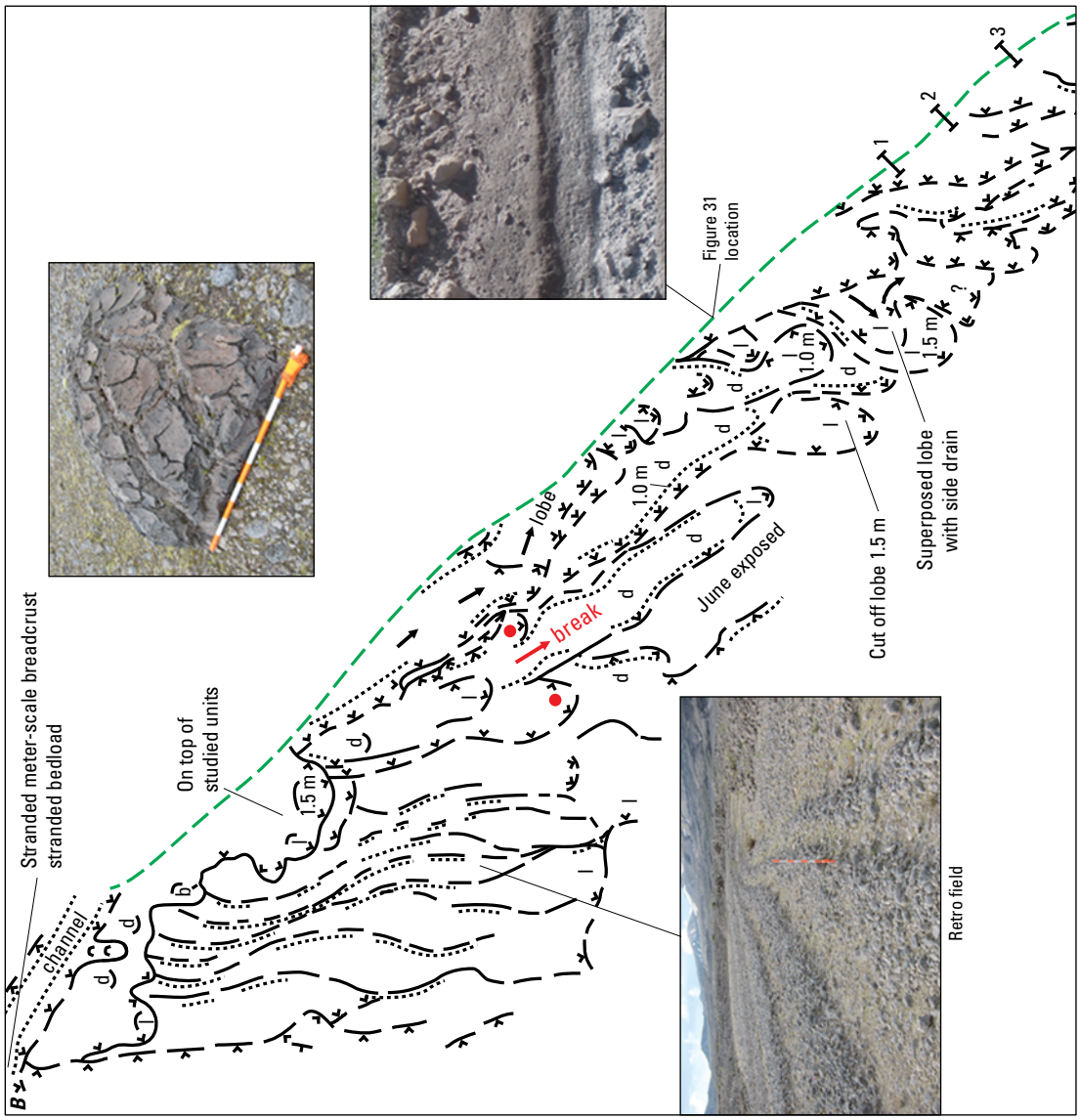

Figure 32. Field map (*A*) enlarged (*B*) to illustrate features of the July 22 deposits near Mathematicians' gully. Note location of late-stage feeder channel with breadcrust block (1-m-long pole pole for scale), retrograde pumice levee field (retro field), and figure 31 photograph.

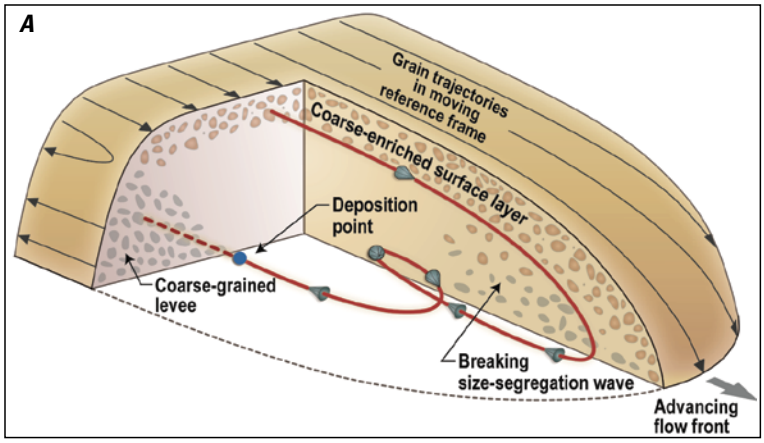

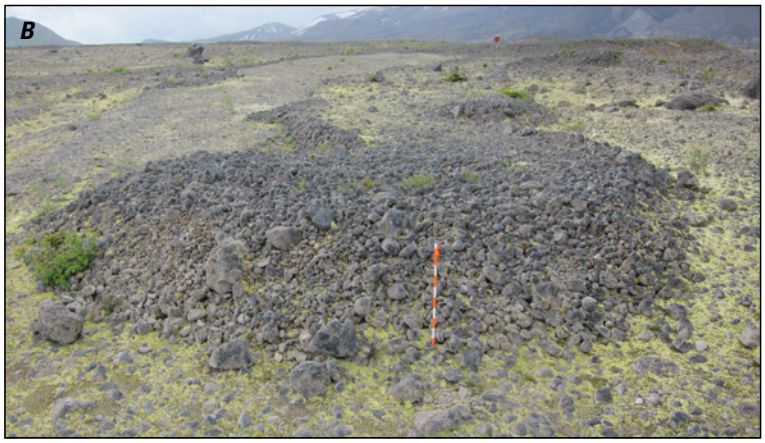

Figure 33. Diagram and photograph of debris flow. *A*, Schematic cutaway illustration of the process leading to formation of lateral levees behind a debris flow front. Red path shows how a coarse grain near the surface migrates toward a levee. Reference frame moves at speed of advancing flow so that grain advancing less rapidly than flow front appears to move backwards (Johnson and others, 2012, gives details). Coarse particles in a granular pyroclastic flow circulate in a fashion similar to those in a debris flow to form lobate termini and levees. *B*, Lobe of July 1980 pumiceous pyroclastic-flow deposit on the Pumice Plain at Mount St. Helens (photographed in 2010). The flow-head deposit shows characteristic bulbous form and is about 1 m thick (pole is 1 m); the levees behind maintain the same form and grain-size characteristics as they bound the channel-flow deposit for more than 250 m into the distance. Sparse meter-scale boulders between the levees (middle distance) are a stranded bedload of relatively dense rock presumed to have rolled or slid along the channel driven and partially supported by the channel-flow mixture. The substrate slope is approximately 4°.

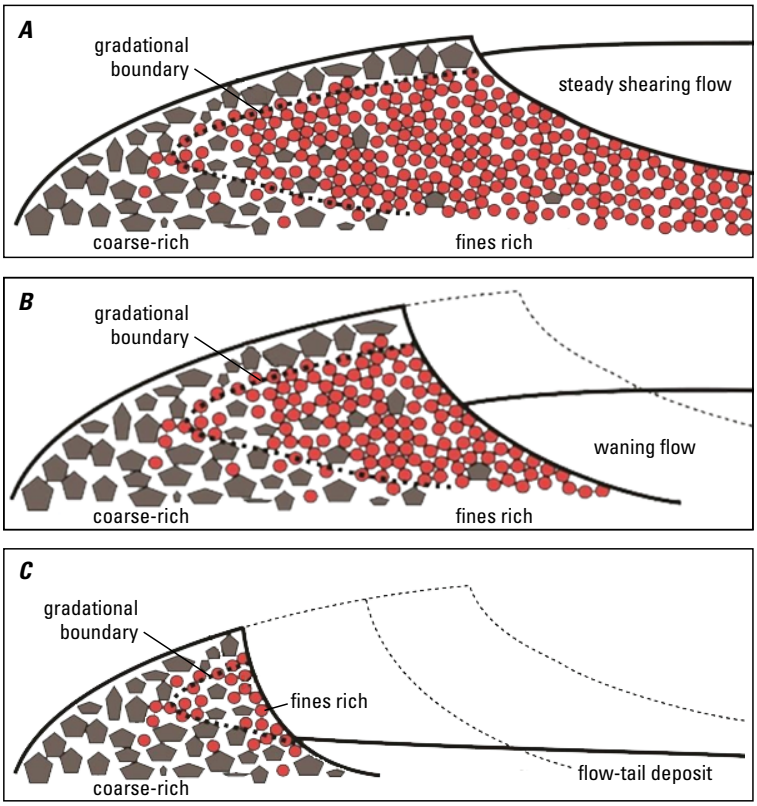

Figure 34. Diagram of "levee sharpening." Gray pentagons represent coarse particles and red circles are fine particles. The bulk of the levee, lined by fine particles, is deposited from a laterally distribution-graded flow that forms in the segregating head cell. The upper layer of coarse particles more directly reflects supply from the coarse-rich layer that forms in the top of the channel-flow. *A*, During steady flow a relatively large layer rich in fine particles is built up on the inner levee wall. *B*, With waning flow, part of the inner levee wall collapses and (or) is eroded, making it narrower. *C*, In a drained channel, further removal of inner levee material has rendered the inner wall very steep and the levee is thus sharpened. At this stage the coarse particles probably form a touching framework in the levee. Throughout the sharpening, a lining of fine particles persists to reduce both flow-contact friction and deposition of large particles by locking. Figure from Kokelaar and others, 2014.

framework of the resistant perimeter is encountered. Throughout the sharpening process, a fine-grained lining persists to reduce both flow-contact friction and deposition of large particles by locking.

Stop 6: Intermediate stage of July 22 retro field
(lat 46°14′59.61″ N., long 122°11′04.02″ W.)

The surface exposes a succession of retrogressively stacked levees that were emplaced midway through the July 22 eruption (figs. 32, 35). Stacking occurred from west to east. Here and elsewhere successions of small nested levees were common in deposits of July 22 and August 7, 1980. Most of these are now destroyed.

We infer that these levees are the result of pulses or waves of pyroclastic flow that moved down a channel containing still-fluidized (soupy) pyroclastic flow material:

- The wave packets cannot be the result of unsteady supply at the vent because field observations show that the July and August deposits derive from single-pulse events at the

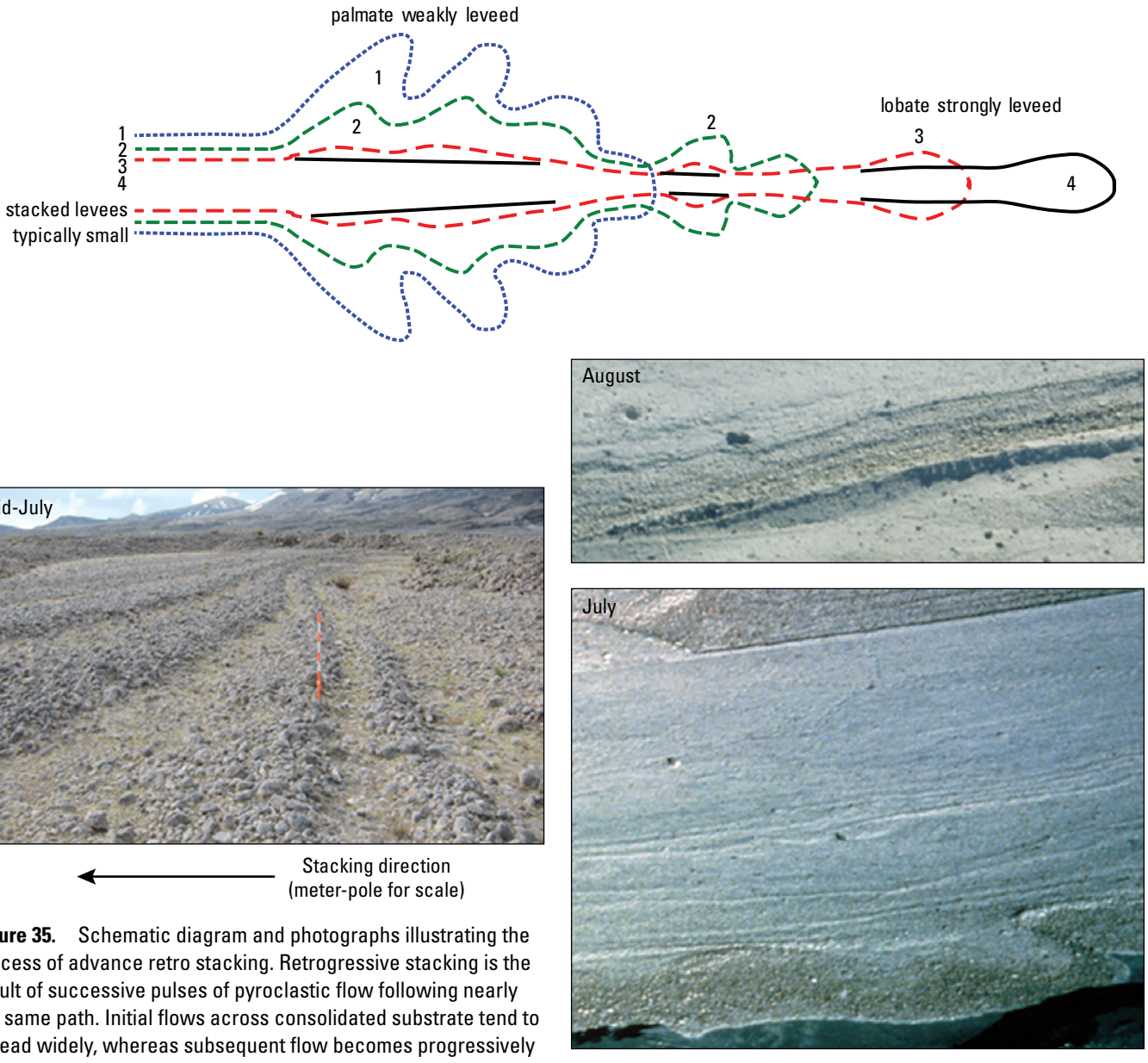

Figure 35. Schematic diagram and photographs illustrating the process of advance retro stacking. Retrogressive stacking is the result of successive pulses of pyroclastic flow following nearly the same path. Initial flows across consolidated substrate tend to spread widely, whereas subsequent flow becomes progressively more confined in leveed channels. Thus, coarse levee systems that resist erosion bound gas-rich, fines-enriched, still-fluid, pyroclastic sediment and serve as conduits for successive waves of the pyroclastic flow. These flows tend to deposit as nested and stacked levee systems. Because the channel is lubricated by the fluid pyroclastic debris, successive flow waves will commonly travel farther than previous ones. Photographs (labeled by month deposited) illustrate successions of as many as 20 or more nested and stacked levees in July and August pyroclastic-flow deposits. The right (east) half of the "retro field" of Stop 6 is an example of a retro-stack field that was partly buried by subsequent flow deposits.

source (two during the July eruption and one during the August eruption) and that the pyroclastic flows from each of these events were emplaced within 5–10 minutes.

- The wave packets plausibly result from inertial flow instability as partly fluidized granular flows moved across the Pumice Plain. Such flow instabilities are possible in all free-surface flows as dictated by the Froude number:

$$\mathrm{Fr}=v^2/gh$$

where

Fr is the Froude number,
v is velocity,
g is acceleration owing to Earth's gravity, and
h is thickness of the flow.

If the Froude number approaches or exceeds one, granular flow is susceptible to instability that will cause it to break into surface waves, sometimes known as roll waves. Forterre and Pouliquen (2003) document surface-wave instability for dense granular flow. We note that any free-surface flow, including pyroclastic flow, is susceptible to such instabilities. Hoblitt (1986) has shown that the August flows were moving 5–10 m/s as they spread onto the Pumice Plain, and we infer that the more voluminous July 22 flows had velocities as great or greater. Judging from levee heights, flow thicknesses were no more than 1–2 m thick. Using these numbers we can infer that pyroclastic flows initially moving across the Pumice Plain had Froude numbers of about 1–10, conditions that favor surface-wave instabilities. Once formed, such waves are likely to continue to propagate even as the flow fronts slow and stop.

- Sequences of waning flow pulses, regardless of origin, will preferentially follow paths bounded by previous levees because the levees consolidate quickly and resist erosion or remobilization whereas the still-fluid material within the levees facilitates flow. For weeks after deposition of the pyroclastic-flow deposits, the fine-grained interiors of the July and August flows remained incompletely consolidated and fluid (fig. 35) (Hoblitt, 1986).

- Subsequent flow pulses remain bounded by levees of previous flows, but will push through terminal levees and flow farther than preceding flows because paths are lubricated by fluid and easily remobilized pyroclastic material rich in fine particles contained between levee frameworks (fig. 35) (Kokelaar and others, 2014).

- Advance retro stacking involves frontal advance with a tendency to stack channels with successively more pumice-rich and steeper levees (fig. 35).

Stop 7: Breakout lobes in Mathematicians' gully area (lat 46°15′01.88″, long 122°11′08.94″ W.)

Downslope or northwest of the retro-stack field, a network of overlapping breakout lobes is distributed across the surface (fig. 32). A feeder channel, now eroded away by Mathematicians' gully, fed these late-stage July 22 lobes. Evidence of the following flowage features can be observed in this area:

- Lobes broke out from the channel when active flow fronts slowed and deposited, thus damming any late-stage flow pulses that followed.

- Where a central channel was stacked high, breakout flows trended away from the central channel at a high angle, commonly 90°, and flowed down to low points (fig. 36).

- Across the gully to the west, a single late-stage flow lobe overlies early thin and widespread flow deposits (figs. 36 and 37). Examination of 1980 photographs (fig. 23) shows that the gully slices a prominent late-stage lobe within a few meters of its terminus nearly perpendicular to its flow direction (fig. 38).

- The core of the lobe is fines enriched and the exteriors are coarse-tail graded.

- Detailed sedimentological measurements show little variation with position within the lobe in the size fractions finer than 8 mm. Larger and less dense grains are segregated to the margins of the flow lobe. In the middle of the flow lobe, coarse, high-density grains are most common at the base, whereas large, low-density grains are most common at the top. A matrix-rich (<1 cm) core occupies the interior of the flow lobe.

Between Stops 7 and 8: We cross from cream-colored blocky July 22, 1980, deposits to gray fine-grained June 12 deposits with scattered lithic blocks several meters in diameter.

Stop 8: June 12 breakaway scarps (lat 46°15′7.66″ N., long 122°10′56.66″ W.)

The June 12 ignimbrite breakaways form headwall scarps and secondary flows with subdued levees (fig. 39). Generally, June 12 deposits are finer grained, thinner, and more widely distributed than July 22 deposits. Initial deposits were metastable and especially prone to remobilization.

Oblique aerial photography shows that breakaway headwall scarps developed incrementally with steep listric detachments that step outward (fig. 40). The headwall scarps grew by upslope piecemeal slope failures of the still-fluid June ignimbrite. We speculate that initial ignimbrite failures may have begun where slopes steepened near the margins of the pumice pond (recall that the pumice pond, now to the west, is filled with June 12 ignimbrite). The photograph (fig. 40) shows that fine ash and gas were preferentially

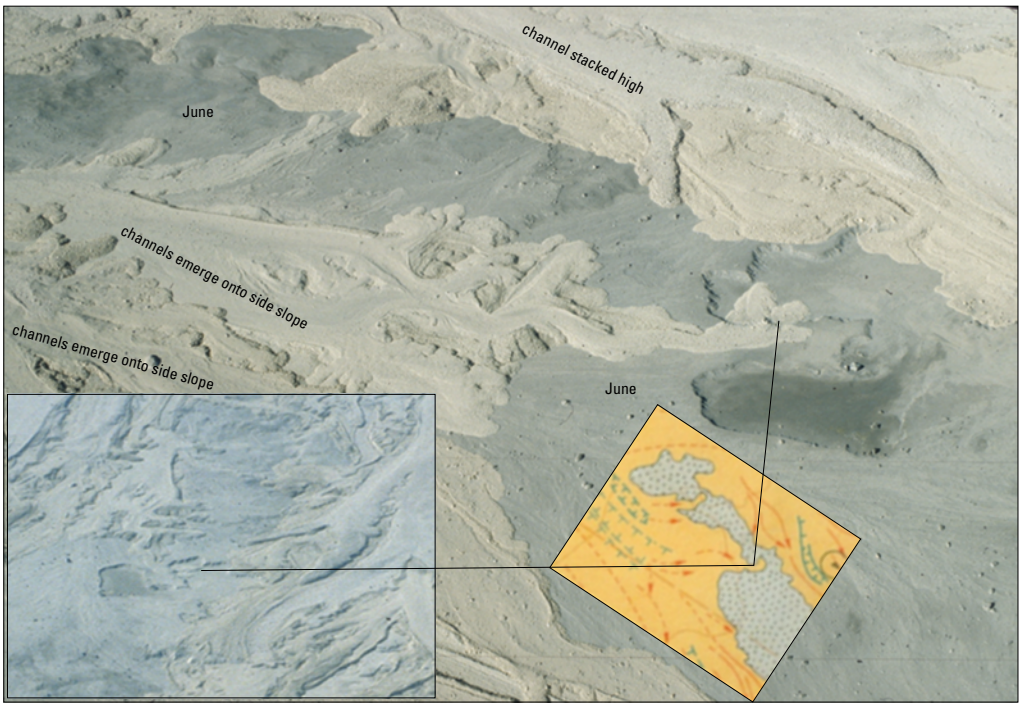

Figure 36. Photograph illustrating how breakaway from a retro-stacked sequence of flows crested at high angles owing to the slope of the retro-stack field. View in this photo is to the southwest. The breakouts typically occur as advancing flows slow and deposit, causing subsequent waves that were more fluid to dam up then spill out over previous levees. This image shows east (lower-left) and west (upper-right) branches of a light-tan-colored July flow overlying a gray-colored June flow. Where a channel is stacked high and levee built above a slope, breakout flows commonly trend away from channels at high angles, near 90°, down to the low point. Insets show equivalent areas of the geologic map of Kuntz and others (1990) and in aerial view.

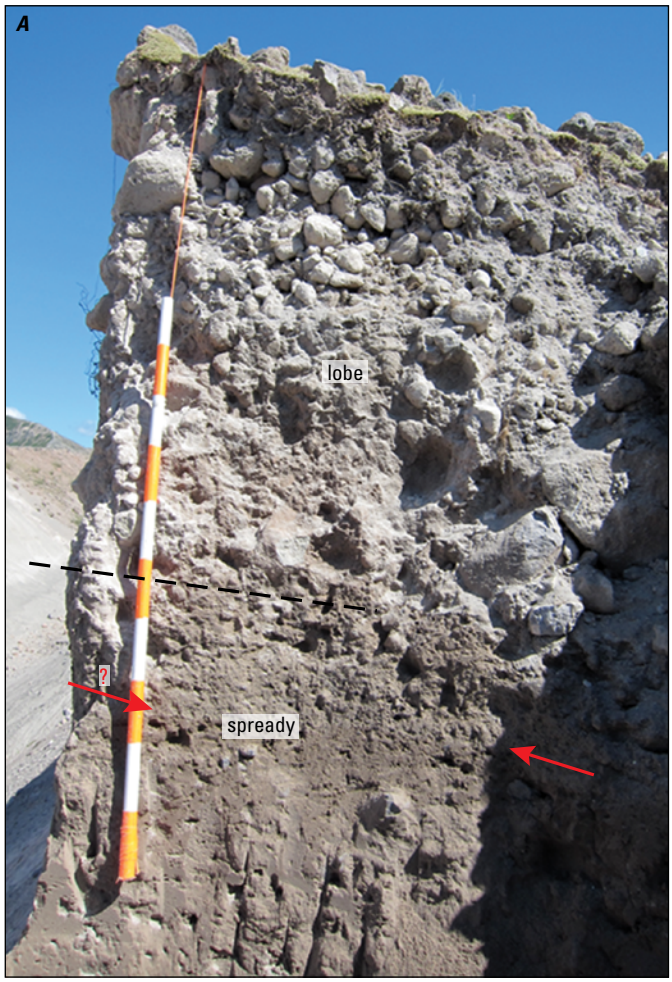

Figure 37. Photographs showing detail section of the MG 5–7 lobe on the west side of Mathematicians' gully. The color change marks the contact between June and July deposits. Here we see no obvious early July 1980 layer, but the lowermost 15–20 cm is inverse coarse-tail graded and could be the "spready layer." The lower 20–70 cm is non-graded; the upper 70–110 cm is the inverse coarse-tail graded lobe. Also, lower large clasts are dense to intermediate and uppermost clasts are low-density pumice.

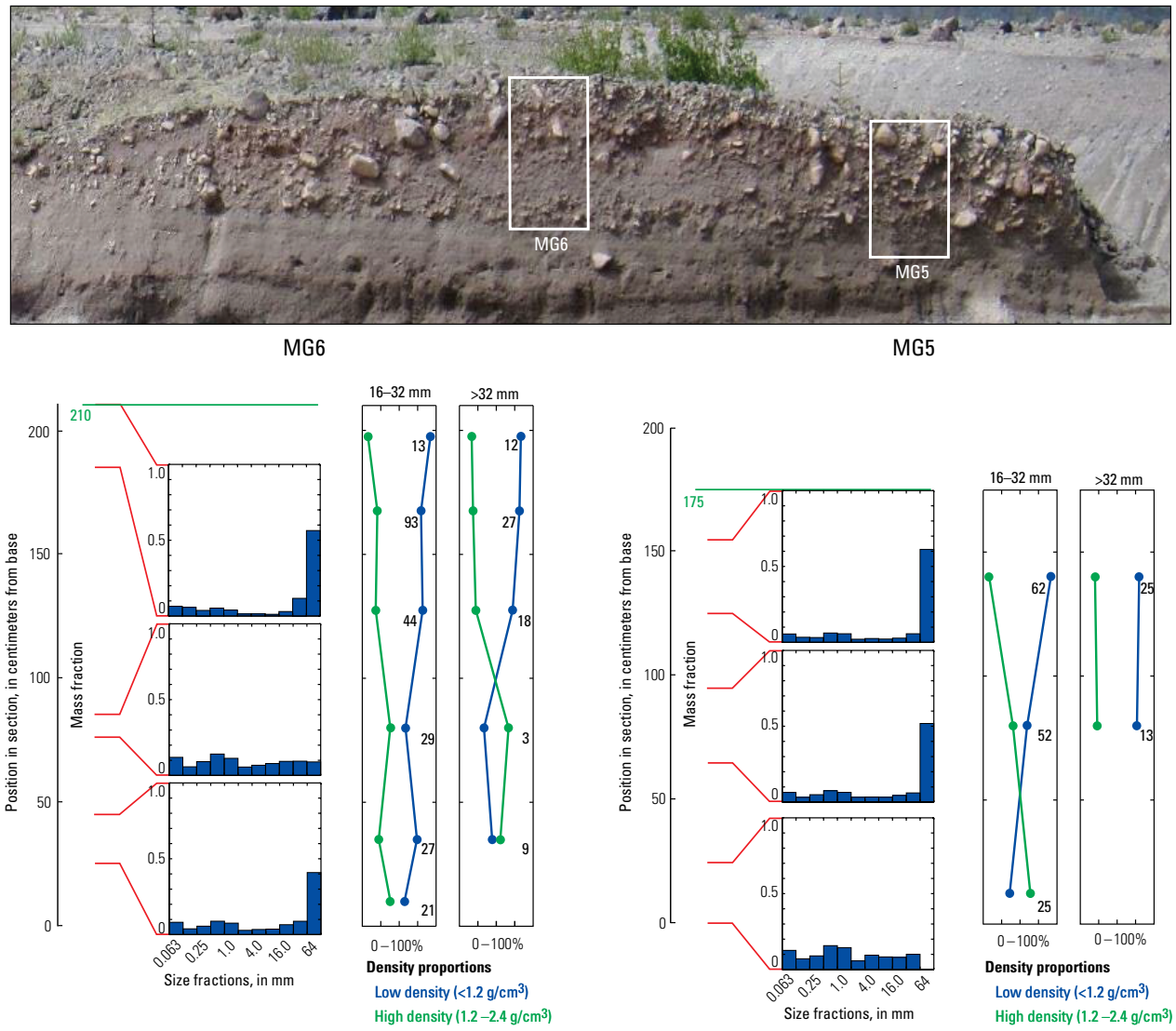

Figure 38. Photograph and sedimentological data from a single pumice lobe that has been sectioned a few meters upslope of its terminus. Photograph shows coarse-grained exterior and fine-grained core. Grain-size plots are standard phi-size histograms with coarse fractions plotted to the right. The plots are stacked in stratigraphic order as shown. Density versus stratigraphic position is shown with density divided into two separate bins: low (<1.2 grams per cubic centimeter [g/cm^3]) and high (1.2–2.4 g/cm^3). Sedimentology data show that grading is coarse tail and does not involve lapilli smaller than about 1 cm. Low-density, coarse-grained pumices are segregated to the top and margins of the flow lobe. Dense particles are concentrated in the basal part of the lobe but are also found in lateral levees. mm, millimeter.

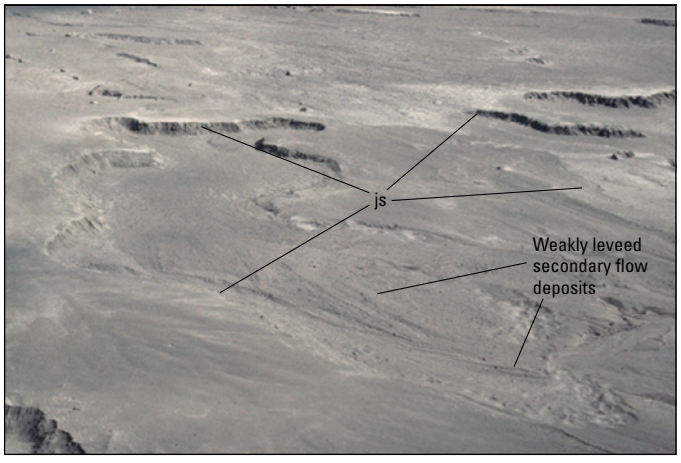

Figure 39. Photograph showing breakaway headwall scarps and weakly leveed secondary-flow deposits of June 12. Pale ash (js) was expelled during remobilization and forms fringes on breakaway scarps and other local drapes.

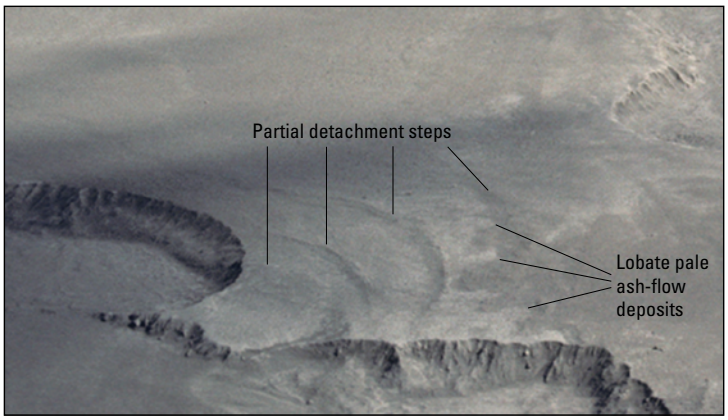

Figure 40. Photograph showing breakaway scarps and partial detachment steps of failed breakaways in June 12, 1980, deposits. These partial detachment steps suggest remobilization of the primary flow by a piecemeal retrograde failure that progressed upslope to form the distinctive scallop-and-mesa topography visible in photographs and preserved in outcrop remnants. Fine-grained pale ash lobes suggest that the retrograde-failure process promoted fine-ash elutriation and may account for why secondary flows are poorer in fine particles and more friable compared to primary June 12 deposits.

vented along the detachments. The expelled ash may have formed low, local clouds (Kuntz and others, 1990), but the locally lobate pale ash deposits indicate slope-sensitive granular flows.

From the last stop, follow the guides on a cross-country hike to intersect the cross-Pumice Plain trail (#270), then south on this trail to a small gravel parking lot at the south end of Windy Ridge near the Truman Trailhead. This lot is known locally as the "research parking lot." Vehicles will be waiting to take the group to the Mount St. Helens Institute campsite.

Road guide from the Pumice Plain to Mount St. Helens Institute campsite (fig. 17)

0.0 From the research parking lot, proceed up the dirt road to the main Windy Ridge Viewpoint and parking lot. This is a primitive road with controlled access. It has several treacherous areas. It may require 4-wheel drive or be impassible by vehicle.

1.9 Locked gate at the southeast corner of the parking lot requires a USFS key or partner key. *Be sure that the lock is fastened such that either padlock will unlock the gate*.

2.1 Windy Ridge Viewpoint parking lot. Restrooms are available. Take paved USFS Road 99 from the north edge of the parking lot headed north (left turn from the lot entrance).

4.0 Pass Smith Creek viewpoint on the right.

4.4 Pass Donnybrook viewpoint.

5.3 Pass Clear Creek viewpoint.

5.6 Pass Harmony viewpoint.

6.9 Pass Independence Pass.

8.4 Turn right onto USFS Road 2560 (unsigned) at Cascade Peaks Interpretive Station, continue past the visitor building onto the dirt road at the far end of the parking lot.

8.5 Locked gate. After the vehicles are through the gate, *be sure that the lock is fastened such that either padlock will unlock the gate*.

9.0 Junction with USFS Road 2562 (unsigned). Take the left fork.

9.7 Junction with quarry road at crest of ridge. Curve hard left to remain on USFS Road 2562.

10.6 Mount St. Helens Institute campsite. Turn left into campsite and park in the open area.

Day 2: Blast, Tephra, and Stratigraphy

By Heather M. Wright,[1] John S. Pallister,[1] and Michael A. Clynne[1]

On Day 2 we visit classic outcrops of pumice, scoria, and ash-fall deposits from Mount St. Helens. These deposits are collectively referred to as "tephra layers" and beds of similar eruption age as "tephra sets" by Mullineaux and Crandell in their classic papers. Letters were used to identify the principal tephra sets erupted in a given eruptive stage or period (table 4). In some cases, the first (capitalized) letter refers to the period or stage (for example, S, Swift Creek stage; P, Pine Creek period). In other cases, this letter refers to a distinguishing color or composition (for example, B, basaltic). For example, W refers to the white color of pumice-rich layers, which were deposited early in the Kalama period and Y refers to the yellow color of slightly iron-oxide-stained pumice layers that were deposited during the Smith Creek period.

A second (lower case) letter was used to distinguish individual fall beds (or multiple thin fall beds in which it is difficult to correlate individual fall deposits across multiple outcrops). This may include the position in the stratigraphy (for example, u, upper; b, basal) or the compass direction of the lobe axis for some distinctive tephra beds with well-defined distributions (for example, the Wn tephra has a dispersal axis to the north). The dominant wind direction in the Pacific Northwest is from west to east; consequently, the best exposures of the tephra deposits are on ridgetops east of Mount St. Helens. However, several large Plinian eruptions took place when the wind was from the south, resulting in tephra layers with dispersal axes to the north. Ridgetops provide the best outcrops because valley bottoms are swept by flows and because the loose fall deposits slump and slide off of the steep flanks of ridges.

The tephras are also distinguished by their mineral contents and in particular by different abundances of the mafic minerals (olivine, augite, hypersthene, hornblende, and cummingtonite). Donal Mullineaux (USGS) used a small mortar and pestle to crush, grind, and pan pumice or scoria lapilli to aid in field identification of the tephra layers. We will demonstrate this technique. Distinctive mineral assemblages and other characteristics of the tephra layers are summarized in table 4.

We will focus on tephra layers that were deposited within the past 3,900 years (the Spirit Lake stage, table 4).

Stop 9: 1980 blast deposit (lat 46°16.061′ N., long 122°03.146′ W.)

In the woods adjacent to the Mount St. Helens Institute campsite we will clean the surfaces of several existing pits to view the stratigraphy of May 18, 1980, and underlying deposits. At the base of the pits, set-X, layer-z, and layer-T tephras are exposed (see table 4) and are overlain by the 1980 blast deposit. The three-fold division of Hoblitt and others (1981) (basal—organic rich, middle—sandy surge, upper—ash and accretionary lapilli) (fig. 41, table 3) can be seen in the sections here. On top of the blast deposit, two May 18 fall units are exposed, a basal lithic-rich fall deposit and the overlying pumice-rich fall deposit. The basal fall deposit corresponds to deposition from the early Plinian column (9:00 a.m.–12:00 p.m.), whereas the overlying pumice-rich fall deposit represents deposition from the steady column that began about 3 hours after eruption initiation and produced the most voluminous pyroclastic density currents of the eruption sequence (table 1).

0.0 From the campsite, return along USFS Road 2562 toward the Cascade Peaks Interpretive Center. *Be sure that the lock is fastened such that either padlock will unlock the gate.*

2.2 At the Cascade Peaks Interpretive Center, turn left onto USFS Road 99 and proceed west toward Windy Ridge.

3.7 Pass Independence Pass Trailhead.

5.0 Stop at Harmony viewpoint to view the northeast arm of Spirit Lake. Note the bare ground on the adjacent

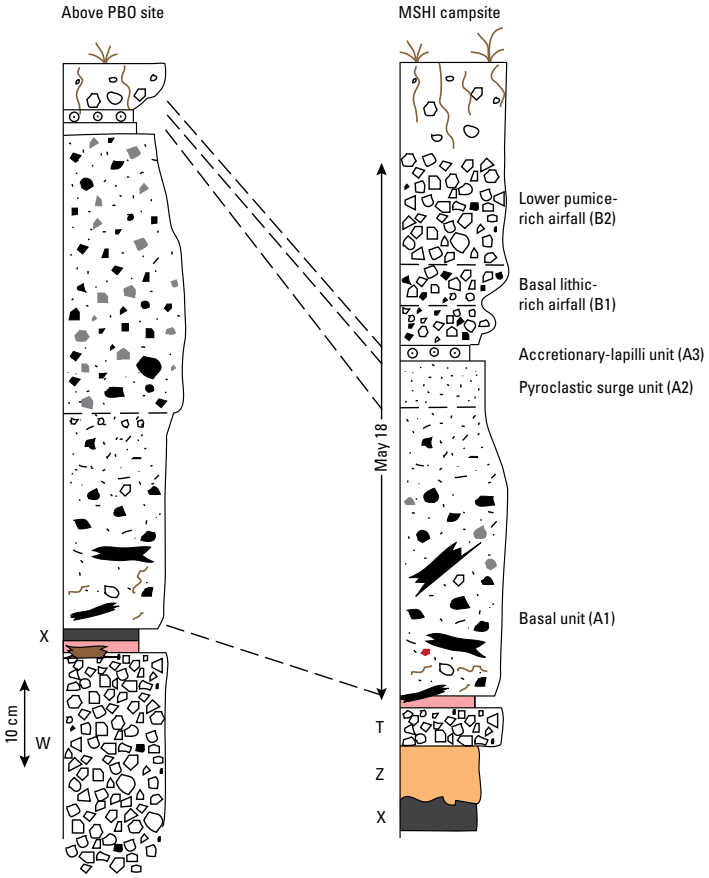

Figure 41. Stratigraphic columns showing sections through the blast deposit on the crest of Windy Ridge above the Plate Boundary Observatory (PBO) strainmeter site and at the Mount St. Helens Institute (MSHI) campsite. cm, centimeters.

[1]U.S. Geological Survey.

ridge, denuded by the May 18, 1980, blast, which had overtaken the debris avalanche at this distance from the volcano. A massive wave of lake water was pushed up the ridge and then washed back downslope, leaving a strand line of trees at the base of the slope (the forest had been downed by the blast a few minutes earlier). The May 18, 1980, debris-avalanche and pyroclastic-flow deposits blocked the natural exit of Spirit Lake, raised its elevation by 64 m, increased its surface area from 5.3 to 8.9 km^2, and decreased the maximum depth from 58 to 34 m.

6.3 Stop at Donnybrook viewpoint. This is a quick stop to photograph Spirit Lake, with trees still floating at the surface (although many have sunk in the past 5 to 10 years). Note also the entrance to the tunnel, which was constructed by the U.S. Army Corps of Engineers following the 1980 eruption (finished in 1985) to prevent lake breakout and flooding on the Toutle River. The tunnel drains the lake into Coldwater Creek, diverting the path of water around the 1980 debris-avalanche and pyroclastic density current deposits.

6.8 Pass Smith Creek viewpoint on the left.

8.7 Stop at the Windy Ridge Viewpoint. A quick stop can be made here for a view of the Pumice Plain and Mount St. Helens. Restrooms are available. Continue to the locked gate at south end of lot.

8.8 Unlock the gate and proceed southeast on the unpaved road. *Be sure that the lock is fastened such that either padlock will unlock the gate.* We are entering an area of the Mount St. Helens National Monument that is normally closed to motorized vehicles. Permission to enter this area by motorized vehicle must be granted by the U.S. Forest Service. Proceed by vehicle or on foot, following the road to the base of Windy Ridge. This is a primitive road with controlled access. It has several treacherous areas. It may require 4-wheel drive or be impassible by vehicle.

9.2 Stop at the Plate Boundary Observatory (PBO) strainmeter.

Stop 10: Two-layer 1980 blast deposit, Windy Ridge (lat 46°14′41″ N., long 122°08′13″ W.)

From the PBO strainmeter, hike north along the ridge crest for about 240 m to a series of pits near the summit of the ridge that are dug into the blast deposit. At this site, an excavation at the top of the ridge exposes a thick section of Wn tephra (>100 cm), overlain by thin layers of We and set-X tephras. The May 18, 1980, blast deposit shows a two-layer stratigraphy, indicating two depositional pulses. Studies by Moore and Rice (1984) and Hoblitt (2000) both suggest that the lateral blast was actually the product of two explosions, closely spaced in time (about 2 minutes apart). Here we can see a lower organic-rich, tawny-colored layer (~20 cm), attributed to the initial blast. A sharp contact separates this material from the overlying "classic" blast sequence, which is massive, lacking in fine particles, and dominated by fresh cryptodome dacite, becoming more stratified and rich in fine particles upwards. At the top of the deposit is the accretionary lapilli unit (blast ash fall) representing aggregated fall deposits from the 30-km-high plume that lofted from the blast pyroclastic density currents (Hoblitt and others, 1981) (table 3). The accretionary lapilli are somewhat poorly preserved here, but it is still possible to distinguish a layer of fine-grained, olive-colored ash.

Return to vehicles and continue south on the unpaved road.

10.8 Arrive at end of unpaved road at "research parking lot" and Truman Trailhead. Depart cars and hike down the drainage that crosses Truman Trail a few meters from the trailhead. Stay in the drainage to minimize damage to sensitive ground surfaces on the Pumice Plain. The Pumice Plain is an area of intensive biological investigation, so please do your biologist-colleagues a favor and tread only in the channel area of the drainage; avoid walking on the upland surfaces.

Stop 11: "Blastalanche" (lat 46°13.901′ N., long 122°09.124′ W.)

Examine the bluffs along the drainage and about 50 m downstream, northwest of the Truman Trailhead marker. The 1980 blast deposit facies is exposed in low bluffs on the sides of the drainage. The blast deposit here, close to the volcano, includes a muddy pyroclastic-flow phase, as well as the more typical sandy open-matrix facies, but here with blocks greater than 20-cm diameter. We informally term deposits in this area "blastalanche" because, this close to the volcano, the blast and debris avalanche were mixing, producing both pyroclastic density current and debris avalanche-like facies. The abundance of lithic blocks and fragments derived from the avalanche-landslide, blast-derived cryptodome fragments, and trees and ash varies considerably. These flowage deposits form low-relief terraces in this local area of a few square kilometers west of Windy Ridge. Note the two distinct varieties of juvenile 1980 cryptodome dacite: gray crystalline-matrix dacite and black glassy dacite. Hoblitt and Harmon (1993) noted that the two types represent volatile-rich (gray, average 0.6 percent H_2O) and volatile-poor (black, average 0.3 percent H_2O) dacite in the cryptodome. They argue that the dacite underwent subsurface degassing, establishing a volatile gradient in the cryptodome. The black dacite shows evidence of early vesiculation and subsequent vesicle collapse. Upon eruption, because of its higher water content, the gray dacite underwent a second vesiculation resulting in the lower density population in the cryptodome dacite clasts.

Continue about 260 m farther downstream along the drainage to a prominent stratified bluff on the right (east).

Stop 12: Tephra deposits of the Spirit Lake stage
(lat 46°14.042′ N., long 122°09.159′ W.)

A 10-m-high bluff on the east side of the first main drainage west of Windy Ridge provides an especially good section of tephra fall and blast deposits from the Spirit Lake and 1980 explosive eruptions (fig. 42). This is the outcrop described by Crandell and Hoblitt (1986). Prepared exposures show the overall section in the main bluff, and the upper part of the section is also exposed in the small tributary at the downstream (northwest) end of the bluff.

The section here consists of pink to gray set-P and dark-brown set-B tephras of Pine Creek and Castle Creek periods and the thin white (dacite) Bi tephra. The set-B tephras are overlain by a pyroclastic density current deposit associated with the Sugar Bowl-period blast—the associated tephra layer D is dated at about 1,030±30 years B.P. (~920 C.E.; table 4). The Sugar Bowl-period deposit is, in turn, overlain by a thick section of the Wn tephra, which was erupted at the beginning of the Kalama period in 1479 C.E. The Wn tephra is overlain by dark-brown set-X tephras, the basal unit (Xb) which contains centimeter-sized scoria was erupted in about 1505 C.E. The overlying pink ash bed "z" represents ash derived from summit-dome eruptions, which continued into the mid-1700s, completing the Kalama tephra section. Tephra layer z is overlain by tephra layer T, a Plinian pumice fall deposit erupted at the beginning of the Goat Rocks period. Finally, tephra layer T is overlain at the top of the bluff by the 1980 blast and fall deposits. The upper part of the section may also be viewed in the small tributary canyon at the downstream end of the exposure.

The tephra layers at Mount St. Helens display a remarkable range in color, mineral assemblage, and clast texture and composition (table 4). This wide range enabled the detailed tephra-stratigraphy studies of Mullineaux (1986, 1996). In addition, the tephra layers are excellent chronologic markers for geologic mapping and for petrologic and geochemical studies. Table 4 provides an updated listing of the distinctive tephra layers from Mullineaux, along with notes about eruptive mechanism and updated age determinations.

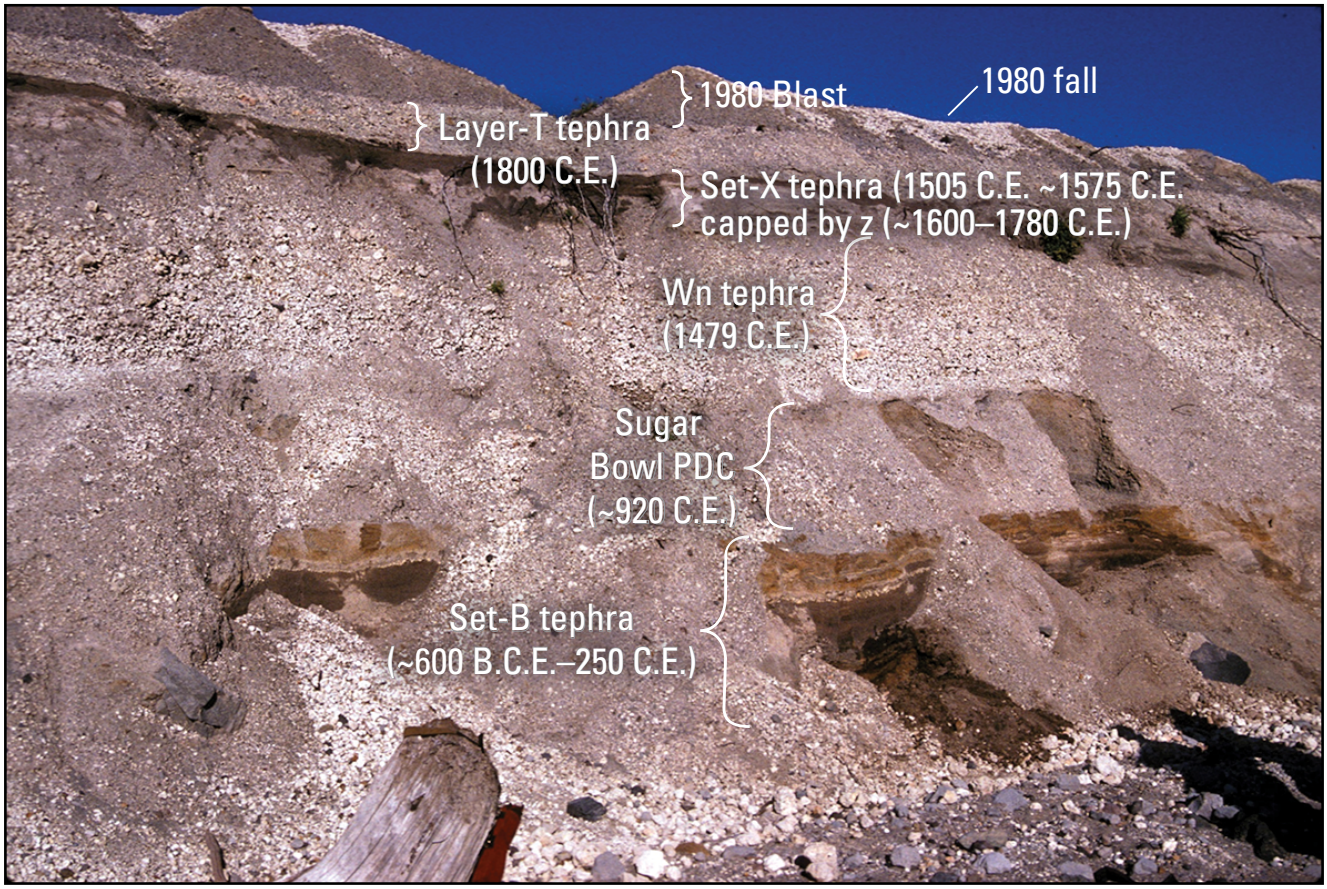

Figure 42. Photograph showing stratigraphic section at Stop 12. Photograph taken in 1990, when the base of the exposed section was within tephra set-B, in subsequent years the section has extended into the set-P tephra. PF, pyroclastic flow or blast.

Table 4. Distinctive characteristics of tephra units from Mount St. Helens erupted before 1980.

[Table modified from Mullineaux (1996), updated with unpublished ages from Michael Clynne, U.S. Geological Survey. A substantial chronostratigraphic change has reassigned the mafic Bh and Bo tephra layers to the Pine Creek period. Tephra units listed in order of increasing age. Co-pf (co-ignimbrite) ash units in lower case; includes deposits from units. v, vesicular; nv, nonvesicular. Ferromagnesian (Fe-Mg) minerals listed in approximate order of abundance; slash denotes a marked decrease in abundance: hy, hypersthene; hb, hornblende; cm, cummingtonite; ag, augite; ol, olivine. Da, dacite; An, andesite; BAn, basaltic andesite; Ba, basalt. abund., abundant; dom., dominant. Col. Ht., eruption column height; yr B.P., years before present; Lrgst., largest eruption of a given stage]

Period	Eruptive characteristics	Tephra set	Layer	Co-pf ash	Munsen color	Units	Vesicularity	Fe-Mg minerals	Composition	Percent lithics	Distrib.[1]	Axis	Grain size (at 8–10 km)[2]	Age[3]	Volume (km^3)[4]	Col. Ht. (km)[4]
Spirit Lake stage (3,900–0 years B.P.)																
Goat Rocks (1800–1857 C.E.)	Block-and-ash flow deposits (Goat Rocks fan), Floating Island lava: 1801 C.E.		T		Light gray	1	v	hy, hb/ag	Da		NE	NE	lapilli	1800 C.E.	0.4	16
Kalama (1479–1750 C.E.)	Early domes, pyroclastic-flow deposits to W, SW and NE, lahars; middle andesite lavas from S crater rim (also Worm Complex, Mitten flow); late summit dome, pyroclastic-flow deposits, lahars			z	Pale pinkish to grayish brown		nv		Da		N-SE		ash	1650 C.E.		
		X	Xh		Brownish gray	many	v, nv		An		NE		ash			
			Xm		Dark gray	many	v, nv		An		N-NW	ENE	ash			
			Xs		Pale to moderate grayish brown	many	nv, v		An		N-S	E	ash			
			Xb		Brownish gray	1	v, nv		An		NE-E	NE	lapilli	1505 C.E.		
		W	Wd	yes	White	1	v, nv	hy/hb	Da		N-E	NE	ash, lapilli			
			We	yes	White	1	v	hy/hb	Da	<30	NE-S	E	lapilli, ash	1479 C.E.	0.4	21
			Wb	yes	White	2	v, nv	hy/hb	Da	abund., <Wa	NE	NE	ash, lapilli			
			Wa	yes	White	2	nv, v	hy/hb	Da	>50	NE	NE	ash, lapilli			
			Wn		Yellowish white	1	v	hy/hb	Da	minor	NE	NE	lapilli, bombs	1479 C.E.	2	24
Sugar Bowl (1,050–1,000 years B.P.)	Domes on three flanks, lateral blast		D		Gray	1	v[5]	hy, hb	Da		NE	NE	ash	1,030 yr B.P.		
Castle Creek (2,025–1,700 years B.P.)	Early andesite & basaltic andesite lava flows, dacite domes, pyroclastic-flow deposits, lava, late basalt	B	Bu		Brown to gray	2	v	ol	Ba		NW-SW		lapilli, ash			
			Bi		White to yellow	2	v	hy/ag	Da		NE-SE	E	lapilli, ash			
			Bd			1	nv, v	hy/ag/hb	Da		NW-N		ash, lapilli			
				bab	Grayish brown	many	nv				NW-SW	E	ash			
				bag	Dark brownish gray	many	nv		An		NW-SW	E	ash			

Table 4.—Continued

Period	Eruptive characteristics	Tephra set	Layer	Co-pf ash	Munsen color	Units	Vesicularity	Fe-Mg minerals	Composition	Percent lithics	Distrib.[1]	Axis	Grain size (at 8–10 km)[2]	Age[3]	Volume (km³)[4]	Col. Ht. (km)[4]
Pine Creek (3,000–2,550 years B.P.)	Domes in crater, extensive block-and-ash flow deposits, lahars, two debris avalanche, lake-breakout lahars	B	Bo		Brown	3	v	ol, ag, hy	BAn		N-W	ESE	ash, lapilli			
			Bh		Brown	2	v	hy, ag	BAn		NW-S	E	lapilli, ash			
				v	Purplish gray to pinkish brown	many					NE-S	E	ash			
		P	Py		Yellowish gray to gray	2	nv, v	hy, hb	Da		N-S	E	ash, lapilli			
			Pu		Gray, salt and pepper	3	nv, v	hy, hb	Da		NE-SE	NE	ash, lapilli			
				pa	Yellowish gray to pinkish brown	many					NE-S		ash			
			Ps		Gray, salt and pepper	2	nv, v	hy, hb	Da	dom.	NE-SE	E	ash, lapilli			
			Pm			1	nv, v	hy, hb	Da		NE-S		ash, lapilli	2,930 yr B.P.		
Smith Creek (3,900–3,300 years B.P.)	Pyroclastic-flow deposits on north flank, lahars North Toutle, co-ignimbrite interbeds with tephra fall, pyroclastic-flow deposits and lahars on SE, dome in crater			pbp	Pink–brown–pink (brown ash bed with reddish brown to pink top and bottom)	many	nv, v				NE-S	E	ash			
		Y	Yu		Yellow	6	nv, v	cm, hb	Da	abund.	NE-SE	E	ash, lapilli			
			Yo		Gray	1	v			dom.	NE-E		ash, lapilli			
				yp	Pinkish brown	1	v				NE-E	NE	ash			
			Yf			5	nv, v	cm, hb		dom.	NE-E	NE	ash, lapilli			
				ya	Dark gray	1	nv	cm, hb		dom.	NE-E		ash, lapilli	3,350 yr B.P.		
				yc	Brown to gray	many	nv				NE-E	E	ash			
			Ye		Yellow	1	v	cm, hb	Da		NE-S	E	lapilli		0.9	23
			Yn		Pale yellow or brown	1	v	cm, hb	Da	few	N-SE	NNE	lapilli, bombs		4	31
			Yd		Gray to brown	3	nv, v	cm, hb	Da	many	NE-SE	E	ash, lapilli			
			Yb		Pale yellow to brownish gray	2	v, nv	cm, hb/bt	Da	abund.	N-SE	N,E	lapilli, ash		0.3	22
Swift Creek stage (16–10 ka)																
	Pyroclastic-flow deposits *under* set J		J	Jg		Gray brown (darker than below)	1	v	hy/hy/ag	An		SW-NW	WSW	lapilli, ash		
			Jb													
			Jy													
	Big pyroclastic-flow deposits to S (co-ignimbrite ash interbeds)		Js		Brown	1	v	hy, hb	An		E-SE	SE	lapilli			
					Grayish yellow to brown	2	v	hy, hb	Da		NE-S	E	lapilli, bomb			
					Gray brown	many	v, nv	hy, hb	Da		E-SE	E	ash			
		S	So		Yellow brown	1	v	cm, hb/hy	Da		NE-SE	ENE	lapilli			
			Sg		Grayish yellow brown	1	v	cm, hb/hy	Da		NE-SE	ENE	lapilli, ash		Lrgst.	
			Ss		Brown	1	v	cm, hb/hy	Da		E-SE	SE	ash, lapilli	12,910 yr B.P.		
			Sw		Pale gray	2	v, nv	cm, hb	Da		NE-SE		ash, lapilli			
			Sb		Yellow brown	many	v, nv	cm, hb/hy	Da		NE-SE		ash, lapilli			

Table 4.—Continued

Period	Eruptive characteristics	Tephra set	Layer	Co-pf ash	Munsen color	Units	Vesicularity	Fe-Mg minerals	Composition	Percent lithics	Distrib.[1]	Axis	Grain size (at 8–10 km)[2]	Age[3]	Volume (km^3)[4]	Col. Ht. (km)[4]
Cougar stage (28–18 ka)																
	Small to moderate volume explosions pumice layers with purple-gray ash interbeds, pyroclastic-flow deposits	K			Brownish gray		v, nv	cm, hb		abund.	E-S		ash, lapilli			
		M	Mt		Yellow pumice		v, nv	hb, hy/cm		abund.	E		ash			
			Mm		Yellow pumice		v	hb, hy/cm		<50	E-S		lapilli, ash			
			Mp		Yellow pumice		v	hb, hy/cm		abund.	E-SE		ash, lapilli			
			Mc		Yellow pumice		v	hb, cm/hy		50	E-S		lapilli, ash		Lrgst.	
			Mo		Yellow pumice		v	cm, hb/ol, hy		abund.	E-SE		ash, lapilli			
			Mg		Yellow pumice		nv, v	cm, hb		abund.	E-SE		lapilli, ash			
				ms			v, nv	cm, hb			E-SE		ash, lapilli			
Ape Canyon stage (>270–35 ka)																
	Pumiceous layers interbedded with ash, pyroclastic-flow deposits	C	Cs		Pale yellowish brown		v	cm, hb/bt	Da		SE-SW	SSE	lapilli, bombs			
			Cy		Pale yellowish brown		v	cm, hb/bt	Da		E-SE		lapilli, bombs			
			Cm		Pale yellow to brown, stained lapilli		v	cm, hb/bt	Da		E-SE		lapilli, ash			
			Cw		Yellow gray, stained lapilli		v	cm, hb/bt	Da		E-SE		lapilli, bombs			
			Ct				v, nv	cm, hb/bt/hy	Da		SE		lapilli, ash			
			Cb		Brown		nv, v	hb/cm/bt	Da		E-S		ash			

[1]Distribution on flanks of volcano given in a clockwise arc; downwind direction is direction carried beyond volcano, if known.

[2]Grain size is dominant grain size along axis of distribution lobe at 8–10 km downwind from volcano.

[3]Ages from Clynne and others (2005, 2008), Yamaguchi (1983, 1985), Yamaguchi and others (1990), and Yamaguchi and Hoblitt (1995).

[4]Volumes and eruption column heights are from Carey and others (1995).

[5]Fine vesicles.

Sugar Bowl-Period Pyroclastic Density Current at Stop 12

Remarkably, a Sugar Bowl-period directed blast was recognized by Crandell and Mullineaux well before the 1980 eruption on the basis of ballistic features and distribution in a narrow lobe extending northeast from Sugar Bowl dome. Blocks of nonvesicular Sugar Bowl-period dacite are found associated with ash in the ballistic deposit, which extends as much as 30 km northeast from the Sugar Bowl dome. The maximum size of ballistic fragments decreases with distance from Sugar Bowl, with a mean diameter of 5 cm extending to 10-km distance. Crandell and Hoblitt (1986) also recognized ash-fall and ballistic deposits, pyroclastic flows, and lahars associated with the blast. They note that, in outcrops near Sugar Bowl dome, the pyroclastic flows are overlain directly by talus shed from the growing dome.

They identified two principal types of dacite fragments in the ballistic and pyroclastic-flow deposits: (1) hypersthene-hornblende, nonvesicular dacite, identical to that which forms the Sugar Bowl dome and (2) dense biotite-cummingtonite-bearing dacite, similar to that found in deposits from the ancient Ape Canyon eruptive stage of Mount St. Helens. The hypersthene-hornblende Sugar Bowl-period dacite blocks are typically prismatic and bread-crusted, indicating that they are juvenile. The presence of dense Ape Canyon-type lithic clasts in the upper part of the pyroclastic-flow deposits, but lack of fragments from the younger pre-Sugar Bowl-period rocks, suggests that the Sugar Bowl dome intruded a buried topographic high, which was developed on Ape Canyon-stage deposits beneath the northwest flank of Mount St. Helens. The lower parts of the deposits were probably derived from an early extrusive phase of the Sugar Bowl dome, and later deposits were derived from deeper levels of the dome or dome-conduit, thereby entraining Ape Canyon rocks from beneath the dome (Crandell and Hoblitt, 1986).

The Sugar Bowl-period pyroclastic flow exposed here consists of nonstratified, poorly sorted gray ash and small lapilli, but also includes breadcrust blocks of juvenile dacite as great as 50 cm in maximum diameter (as seen in among the blocks in the drainage). Although the pyroclastic flow here appears to be a single unit, differences in the lithic types in the lower and upper parts indicate that two units are present. Rock fragments in the lower part are entirely of Sugar Bowl-period dacite, those in the upper part include about 15 percent of Ape Canyon-type biotite-cummingtonite dacite. Wood fragments and twigs are abundant in the deposit, and the lower part contains abundant conifer needles, some of which are carbonized, as well as lenses of soil that were entrained upward into the deposit. The entrained soil, flat top of the deposit, and massive and poorly sorted character indicate emplacement by flowage.

Petrologic Discussion Concerning the Stratigraphy at Stop 12 (Kalama-Period Magma Mixing)

The tephra outcrops here are a good place to consider how such substantial changes in erupted magma composition during the Kalama period can take place in such short periods. It was field relations such as these, which show large compositional changes (67–58 percent SiO_2) in short time spans (for example, 25 years between eruption of Wn and set-X tephras), along with the presence of mingled pumice and scoria in the set-X and -W tephras that first led Pallister and Hoblitt (1985) and Pallister and others (1992) to suggest magma mixing as the dominant process responsible for compositional variation during the Kalama period.

Pallister and others (1992) further proposed that the approximately linear silica-variation (Harker) diagram trends of the early-Kalama-period compositions with respect to major, minor, and many trace elements represents magma mixing between a set-W tephra-type dacite and a chromium- and high field strength element (HFSE)-enriched (OIB-like) basaltic magma, the latter similar to one of the basalt types erupted during the Castle Creek period (figs. 43, 44). They further suggested that the late-Kalama-period linear trend might represent mixing between dacite and a different (chromium- and HFSE-depleted)

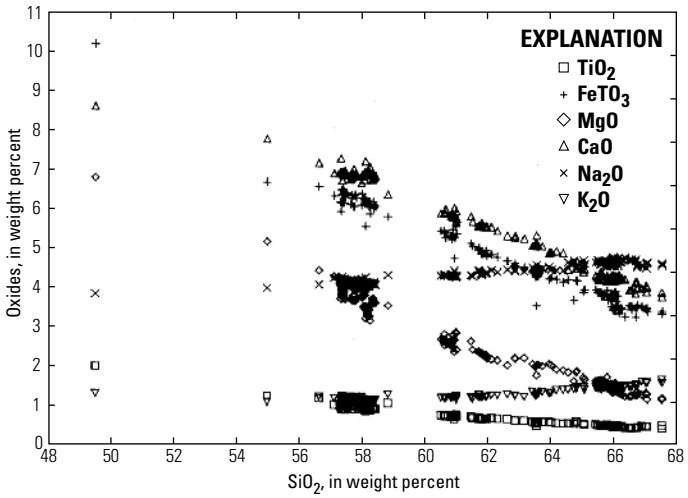

Figure 43. Harker diagrams for Kalama dacites and andesites compared to basalts from the Castle Creek period (modified from Pallister and others, 1992). The basalt composition plotted here includes high field strength element (HFSE)-enriched (ocean island-like) basalts, including the north flank-type samples of Smith and Leeman (1987). Additional U.S. Geological Survey analyses of basalts from the Castle Creek period span a range of compositions and include high-TiO_2 (~2 percent) and low-TiO_2 (<2 percent) types. Cave Basalt and pre-Cave basalt, which have crossing rare-earth element (REE)-patterns compared to Kalama REE-patterns, are not plotted. Points plotted in blue represent mingled scoria clasts from the basal set-X tephra and associated flowage deposits.

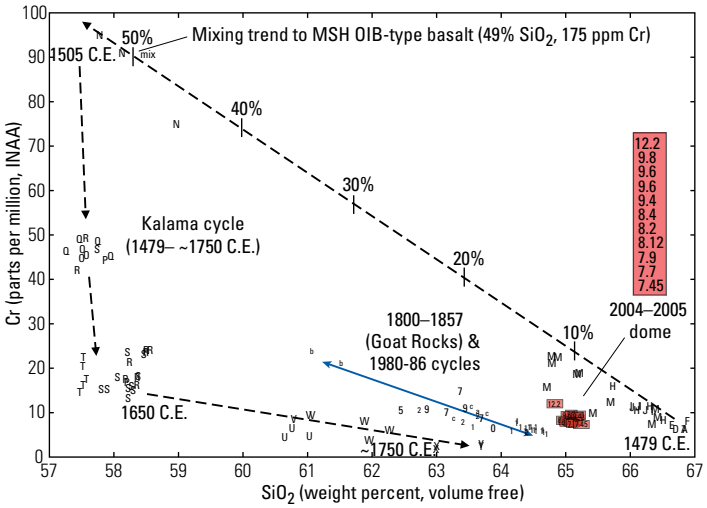

Figure 44. Variation diagram of chromium versus SiO_2 for samples from the Kalama, Goat Rocks, 1980–1986, and 2004–2008 eruptive periods. Chromium abundances are from Instrumental Neutron Activation Analyses (INAA); analytical uncertainties based on repeat analyses of the bulk samples yield error bars of less than one to two times the size of the bold letters in this graph; A–G are from the set-W tephras, H–M are from early-Kalama-period pyroclastic flows, N's are scoria samples from the basal Xb tephra, O–T are andesite lava samples from the middle Kalama period, and U–Y are from the late-Kalama-period summit dome. Letters and numbers are in stratigraphic order (lower to upper). Dashed line is a hypothetical mixing line between dacite of Wn pumice composition and a tholeiitic (OIB-type) basalt composition from Smith and Leeman (1987) that was erupted in the Castle Creek period.

basalt type. A similar conclusion was reached by Gardner and others (1995). Subsequent work by Carroll (2009) confirmed the mixing model of Pallister and others (1992) for the early-Kalama-period trend, and showed that even the Wn and We pumices contain rare olivine and augite, interpreted as evidence of mingling of a small amount of mafic magma in the earliest eruptions of the Kalama period. Subsequent work by Lieuallen (2010) also confirmed the general magma-mixing hypothesis for the Kalama period, but showed that it was more complex than envisioned by Pallister and others (1992) and Carroll (2009). Lieuallen's study was more detailed than the previous work; it included extensive mineral chemistry as well as analysis of juvenile components in X-tephra-age lahar and lava samples, quenched mafic inclusions, and gabbroic inclusions. Like Carroll, Lieuallen confirmed that mixing of dacite and an HFSE-enriched (OIB-like) calc-alkaline basalt was involved in the early-Kalama-period trend. She also confirmed that mixing between dacite and a different basalt type (lower-HFSE calc-alkaline) began during the middle Kalama period and was involved in the origin of the later Kalama-period magmas (see also Gardner and others, 1995). Her work on quenched mafic inclusions also showed that the mafic mixing endmembers involved in the Kalama period interacted in complex ways upon invading the cumulus gabbroic base of the crustal reservoir system. Such interactions included assimilation of earlier formed gabbroic cumulates and Miocene gabbroic wallrocks and resulted in a range of compositional and textural evidence in the erupted magmas.

From Stop 12, continue about 30 m down the drainage to the north, then turn left and hike about 200 m up the tributary canyon to the south-southwest until you intersect the Truman Trail. At the trail turn right (west) and hike about 100 m along the front of a tephra-blanketed lava flow.

Stop 13A: Andesite of Section 26 (lat 46°13.948′ N., long 122°09.250′ W.)

Continue up the west flank of the flow to the small canyon

Stop 13B: Basaltic andesite of Truman Trail (lat 46°13.883′ N., long 122°09.434′ W.)

A good section of the andesite of Truman Trail is exposed here.

Castle Creek Stratigraphy—A Discussion at Stop 13

As noted in the introductory section of this guidebook, the Castle Creek period was the most complex and compositionally diverse period of the Spirit Lake stage. Compositions from dacite to basalt were erupted during a roughly 325-year-long interval between about 2,025 and 1,700 years B.P., in three phases (early, middle, and late). The early phase was primarily dacitic and includes two groups of deposits: (1) pumiceous and lithic pyroclastic flows, dacite lava flows, and the northwest dome, and (2) Dogs Head dacite dome, lithic pyroclastic flows and related lahars found on the south flank, tephra layer Bi, and the lava flow at Redrock Pass. All these deposits were erupted in the interval ~2,025–1,990 years B.P. and are primarily finely porphyritic augite-hypersthene dacite.

Deposits of the middle Castle Creek period are confined to the south flank of Mount St. Helens. This phase was initiated by eruption of basaltic tephra Bu1, and followed by three units of mafic lava flows: basalt of the south flank, pre-Cave Basalt and basaltic andesite, and Cave Basalt. These eruptions took place shortly before and about 1,895 years B.P. Rock types are primarily porphyritic (augite)-olivine basalt and basaltic andesite.

During the late Castle Creek period, eight (possibly nine) units of basalt to andesite were erupted on the north and east flanks of Mount St. Helens (table 5). In order of eruption these are (1) andesite of section 26, (2) basaltic andesite of Truman Trail, (3) tephra Bu2 and basalt of the north flank, (4) andesite of the Plains of Abraham, (5) andesite of Sasquatch Steps, (6) tephra Bu3 and basalt of Castle Creek, (7) basaltic andesite of Nelson Glacier, and (8) andesite of Loowit Trail. Andesite of the Baguette, a pyroxene-andesite lava flow of uncertain age on the southwest flank, is lithologically and compositionally similar to andesite of Sasquatch Steps, and may be related to the late Castle Creek period. These lava flows were emplaced between about 1,895 and 1,700 years B.P. Four radiocarbon ages for units 5 and 6 in the list above

range from 1,795±30 to 1,730±35 years B.P., and paleomagnetic directional data suggest that this period of volcanism was short. Late Castle Creek-period lava flows cap parts of the post-1980 crater rim. Rock types are a variety of porphyritic olivine basalt, augite-olivine basaltic andesite, and augite-hypersthene andesite. Late Castle Creek units contain equilibrium to weak-disequilibrium to strong-disequilibrium phenocryst assemblages.

Composition and Petrology of the Late Castle Creek Period

Brief petrographic descriptions of the late-Castle Creek-period units that describe the major characteristics of the rocks are given in stratigraphic order in table 5. In general, the basalts are coarsely porphyritic, with simple phenocryst assemblages of olivine and plagioclase. The basaltic andesites to andesites are finely porphyritic, with augite-olivine and augite-hypersthene assemblages dominated by multiple populations of plagioclase. Most units contain glomeroporphyritic clots or large crystals derived from clots that were picked up in the Mount St. Helens magmatic system and probably represent cumulus crystals fractionated from mafic magmas.

Late Castle Creek-period units span a range of compositions from 49 to 64 weight percent SiO_2, 0.9 to 1.7 weight percent K_2O, 7.4 to 2.2 weigh percent MgO, and 2.2 to 0.7 weight percent TiO_2. There are nine stratigraphic units, (1) andesite of section 26, (2) basaltic andesite of Truman Trail, (3) basalt of the north flank, (4) andesite of Sasquatch Steps, (5) andesite of the Plains of Abraham, (6) andesite of the Baguette, (7) basalt of Castle Creek, (8) basaltic andesite of Nelson Glacier, and (9) andesite of Loowit Trail. Late Castle Creek-period andesites and basalts plot as clusters or linear arrays in a wide band. These units form an array on some Harker diagrams (for example CaO, FeO*, and Na_2O) that is more coherent than the entire Castle Creek period (for example),

Table 5. Petrography and stratigraphy of lava flows of the late Castle Creek period.

[Units listed in stratigraphic order of youngest to oldest. pl, plagioclase; ol, olivine; ag, augite; hy, hypersthene; hb, hornblende; %, percent; Cr, chromium; mm, millimeter]

Unit name	Percent SiO_2	Percent phenocrysts	Phenocrysts	Notes
Andesite of Loowit Trail	58.9–63.4	15–25	pl>hy>ag	Remnants of three slightly different but similar andesites that overlie basaltic andesite of Nelson Glacier. Finely porphyritic, dominated by small, weak to complexly zoned plagioclase and a second population with a variety of sieved to patchy zoned cores and overgrowth rims. Glomeroporphyritic clots of plagioclase and pyroxene and strongly reacted hornblende are sparsely present.
Basaltic andesite of Nelson Glacier	54.9–56.1	30	pl>ol>ag	Olivine (4%) has thin reaction rims of pyroxene and some contain inclusions of Cr-spinel. Augite (1–2%) is small. Most plagioclase (25%) is small and has weak zoning, but a smaller population is larger, sieved and with thick clear overgrowth rims. Glomeroporphyritic clots and larger resorbed crystals are rare.
Basalt of Castle Creek	50.3–53.6	15–20	pl>ol>(ag)	Coarsely porphyritic olivine basalt. Olivine (5–8%) contains abundant inclusions of Cr-spinel and calcic plagioclase (5–15%) and is weakly zoned. A second population of sieved sodic plagioclase is present in variable abundance and wormy-cored augite is rare.
Andesite of the Baguette	59.0–61.9	25–30	pl>hy>ag	Majority of phenocrysts are small, euhedral and unreacted (hypersthene 3–4% and augite 1–2%), but a small proportion are found as glomeroporphyritic clots and larger crystals derived from clots that have reaction rims or are sieved. Unsieved, small, weakly zoned phenocrysts of plagioclase (20–25%) dominate the phenocryst assemblage, but a sparse population of larger phenocrysts with strongly sieved cores and thick clear overgrowth rims is present. Andesite of the Baguette contains sparse olivine-bearing quenched magmatic inclusions. Andesite of the Baguette is texturally similar to the andesite of the Plains of Abraham and andesite of Sasquatch Steps.
Andesite of the Plains of Abraham	59.1–62.6	15–25	pl>hy>ag	Bimodal with large and small phenocrysts. Majority of phenocrysts are small, euhedral and unreacted (augite 1–2% and hypersthene 2–3%), but a small proportion are glomeroporphyritic clots and larger crystals derived from clots that have reaction rims or are sieved. Unsieved, small, weakly zoned phenocrysts of plagioclase (15–20%) dominate the phenocryst assemblage, but a sparse population of larger phenocrysts with strongly sieved cores and thick clear overgrowth rims is present. Texturally similar to the andesite of the Baguette and andesite of Sasquatch Steps.

Table 5.—Continued

Unit name	Percent SiO_2	Percent phenocrysts	Phenocrysts	Notes
Andesite of Sasquatch Steps	55.0–59.2	25–30	pl>ol>ag; pl>hy>ag>(ol); ag=ol>hy	Some early flows, <57% SiO_2, are augite-olivine basaltic andesite. Later flows, generally >57% SiO_2, are dominantly (olivine)-augite-hypersthene andesite. A few flows with about 57% SiO_2 contain sparse hypersthene and subequal amounts of augite and olivine. Olivine has increasingly thick reaction rims of pyroxene as SiO_2, increases. Unsieved, small, weakly zoned plagioclase phenocrysts dominate the phenocryst assemblage, but a sparse population of larger phenocrysts with strongly sieved cores and thick clear overgrowth rims is present. Some flows contain glomeroporphyritic clots and individual crystals of plagioclase, pyroxene, hornblende, and occasionally olivine derived from clots are a sparse component of most flows.
Basalt of the north flank	49.7–50.2	10–15	ol≥pl	Coarsely porphyritic olivine basalt. Olivine has abundant inclusions of Cr-spinel. Calcic plagioclase is weakly zoned, some have sodic cores.
Basaltic andesite of Truman Trail	56.2–57.5	25–30	pl>ag>ol> (hy) (hb)	Most phenocrysts are small (<1 mm). Assemblage dominated by plagioclase (20%) of several populations including unsieved calcic plagioclase and sieved sodic plagioclase. Olivine (1–2%) has thin to thick reaction rims of pyroxene and contains inclusions of Cr-spinel. Euhedral augite (2–3%) is mostly <0.25 mm.
Andesite of section 25	59.2–61.6	30–35	pl>hy>ag> (hb)	Most phenocrysts are small (<1 mm), but flows also contain a smaller population of larger phenocrysts including sieved sodic plagioclase, spongy-cored augite, hypersthene with reaction rims, and reacted hornblende. Euhedral augite (2%) is small (<0.25 mm). Euhedral prismatic hypersthene (2%) is 0.25–0.75 mm and larger crystals display reverse zoning. Anhedral olivine is small and sparse, with thick reaction rims of pyroxene. Euhedral, ~1 mm, weakly zoned, intermediate composition plagioclase is abundant (25%). Large (to 3 mm, mostly 1 mm) strongly sieved sodic plagioclase (5%) is resorbed and anhedral, but has clear overgrowth rims. Coarse-grained gabbroic inclusions common. Contains at least three mingled components: dacite, olivine-bearing basaltic andesite (possibly basaltic andesite of Truman Trail), and crystals derived from gabbroic inclusions.

but form more scattered arrays of MgO, TiO_2, P_2O_5, Al_2O_3, FeO*/MgO, and especially K_2O. Incompatible and compatible trace elements display ranges and patterns similar to K_2O and MgO respectively, and are not further discussed.

The order of eruption—two mixed andesites, basalt, three andesites, basalt, basaltic andesite, and andesite—suggests several cycles of fractionation and mixing. The two earliest late-Castle Creek-period units are andesite of section 26 and basaltic andesite of Truman Trail. Both units have a range of composition and phenocryst assemblages that suggests a mixing origin involving three components: (1) a felsic magma containing hypersthene, hornblende, and sodic plagioclase phenocrysts, (2) a mafic magma containing olivine and calcic plagioclase phenocrysts, and (3) cumulus pyroxene and plagioclase derived from somewhere in the plumbing system. Andesite of section 26 has a larger proportion of component 1 and basaltic andesite of Truman Trail has a larger proportion of components 2 and 3. The mafic magma may then have erupted as the relatively uncontaminated basalt of the north flank.

Andesite of Sasquatch Steps, andesite of the Baguette, and andesite of the Plains of Abraham are lithologically similar, and probably erupted sequentially. A second cycle of andesite to basalt might be proposed to explain their relation to basalt of Castle Creek. Finally, a third cycle is required to explain the basaltic andesite of Nelson Glacier and the andesite of Loowit Trail. Olivine with chromium spinel inclusions demonstrates that most basaltic andesites and andesites have a basaltic parent. Although they are grossly similar, the mineralogy and compositional variety of Mount St. Helens basalts and basaltic andesites suggests that at least three separate parental mafic magmas are involved (Wanke and others, 2016). Some minimally-fractionated basalts ascend into the shallow Mount St. Helens magmatic system where they grow large crystals at low pressure and pick up cumulate crystals but are not substantially contaminated. This requirement demonstrates that, at some times, small mafic magma batches can enter and ascend through the Mount St. Helens magmatic system without being completely obscured by a resident felsic component.

In summary, the compositional diversity of the Castle Creek-period rock types required repeated mafic magma inputs into the shallow magmatic system. Once there, interaction with felsic magma and cumulate mush residing in the magmatic

system played a role in generating the diversity of the late Castle Creek period.

After leaving this stop, the trail to the crater crosses numerous thin lava flows of coarsely porphyritic olivine basalt of Castle Creek and andesite breccias formed of andesite of Loowit Trail. After crossing Loowit Creek and beginning up the Sasquatch Steps, the route crosses lava flows and breccias of andesite of Sasquatch Steps. Once in the crater, outcrops of coarsely porphyritic (olivine)-augite-hypersthene andesites of the Pine Creek period can be seen. These rocks form most of the crater walls above the Pine Creek-period dacite domes.

From Stop 13, return to Truman Trail and hike about 450 m southeast, back to the trailhead and the research parking lot.

0.0 From the research parking lot, drive back to toward the Windy Ridge Viewpoint and then continue for 8.6 more miles to the Cascade Peaks Interpretive Station.

19.4 Arrive at the Cascade Peaks Interpretive Station and park in the lot. Walk to the outcrop on the north side of USFS Road 99. *Be careful of traffic.*

Stop 14: Wn tephra (lat 46°16.914′ N., long 122°04.946′ W.)

This is a short stop to view the Wn tephra layer near its downwind distribution axis. The layer is mantling a slope but, with a bit of digging to expose the base, we can estimate a thickness of more than 2 m.

20.8 Pass Meta Lake trailhead.

20.9 Stop at the Miner's Car viewpoint, just short of the junction with Norway Pass Road (USFS Road 26).

Stop 15: Vehicle caught in the blast (lat 46°17.793′ N., long 122°04.526′ W.)

This is a quick stop to examine a vehicle that was caught in the blast. Studies of the impact of the blast on the car (for example, the tires did not burn but plastic became soft and deformed) were used to determine that the blast moved at velocities reaching about 1,000 km/hr and transient temperatures were as much as about 350 °C in this area, 14 km miles from the vent. The blast devastated an area of about 600 km^2 and extended 27 km north of the crater.

From Stop 15, continue on USFS Road 99 for 4.5 miles.

25.5 Stop at the Bear Meadow viewpoint.

Stop 16: Early eruption viewpoint (lat 46°18.822′ N., long 122°02.178′ W.)

This is the location where, on May 18, 1980, Gary Rosenquist took the renowned sequence of photographs of the 1980 Mount St. Helens debris avalanche and early phases of the eruption (see Voight, 1981, fig. 38).

From Bear Meadow, turn right (east) onto USFS Road 99 and proceed 4.6 miles to the intersection with USFS Road 25.

30.1 At the intersection of USFS Roads 99 and 25, turn right (south) on USFS Road 25 toward Cougar, Wash., for 8.1 miles.

38.2 Turn left (west) onto a dirt road and proceed 0.5 mile.

38.7 Stop at the prominent roadcut bluff on the right (south).

Stop 17: Stratigraphic section of tephra (lat 46°14.3772′ N., long 121°58.0446′ W.)

This tephra locality is on a ridge 18 km east-northeast of the volcano. Here we see a stratigraphic section of tephra layers overlying Tertiary basement rocks. Representative fall deposits from the following eruptive stages and periods are seen here: Swift Creek (tephra set J), Smith Creek (tephra set Y), Pine Creek (tephra sets P, lower B), Castle Creek (tephra set upper B), Kalama (tephras We and set X), and 1980 fall deposit.

En route to Alternate Stop A-1 (*We will visit Stop A-1 instead of Stop 17 if the road has been repaired.*)

One of the best and most complete sections of tephra deposits from the past 12,000 years is located about 7 miles south of the Cascade Peaks Interpretive Station on Smith Creek Road. This locality is on a ridgetop 10 km east-northeast of the volcano in the dominant downwind direction. Unfortunately, a section of the road was lost to a landslide in 2016. Future users of this guide may reach the locality with an 8-mile (13-km) roundtrip hike from the site of the landslide, so a log and description is provided as follows.

0.0 From Cascade Peaks Interpretive Center, turn left (southeast) into the entrance road to the restaurant and continue 0.1 miles southeast to the locked gate on the unpaved and unsigned road (USFS Roads 2560 and 2562; Smith Creek Butte Road). Unlock the gate (*be sure that the lock is fastened such that either padlock will unlock the gate*), and proceed southeast on the dirt road. This area of the Mount St. Helens National Monument is normally closed to motorized vehicles. Permission to enter this area by motorized vehicle must be granted by the U.S. Forest Service.

0.5 At the junction of USFS Roads 2560 and 2562 (both are unsigned), take the right (west) fork on Road 2562 and descend toward the headwaters of Bean Creek.

2.0 Cross Bean Creek, then continue on Road 2562, climbing onto the ridge between Bean Creek and Smith Creek to the west.

3.1 Walk from where the road is washed out by a landslide.

4.8 Cross over into the Clearwater Creek drainage for downwind views of the blowdown.

6.0 At the junction of USFS Road 2562 and USFS Road 540 (neither is signed), take the right (west) fork, remaining on Road 2562.

7.1 Stop at the point where the road cuts through a 10 m high road cut on the left. The tephra section here has been excavated many times, but some cleaning of the steep roadcut surface with shovels always helps reveal wonderful details.

Alternate Stop A-1: 12,000 years of Mount St. Helens tephra stratigraphy and the 1980 blast deposit
(lat 46°13.204′ N., long 122°03.681′ W.)

Exposed here is a stratigraphic section extending back to the 13–12 ka tephra set S and the 11–10 ka tephra set J, both of the Swift Creek eruptive stage. In this single roadcut, we also see representative fall deposits from each eruptive period of the Spirit Lake stage, except for the Sugar Bowl-period blast (layer D) and Goat Rocks period (layer T). As illustrated in figure 45, tephra layers from the following eruptive periods are seen here: Smith Creek (tephra set Y), Pine Creek (tephra sets P and lower B), Castle Creek (tephra set upper B), Kalama (tephra sets W and X; layer z), and 1980 fall and blast deposits. Although not shown in figure 45, which was taken in 1990, deeper levels at the base of the outcrop have now been excavated, exposing both set-J and set-S tephra layers of the Swift Creek stage.

The upper part of the section (Castle Creek set B; Kalama set W, set X, and layer z) is best viewed near the north end of the bluff. A section of the 1980 blast deposit is visible atop the low bluff at the far (south) end of the outcrops (fig. 46). The blast deposit displays the three-fold division of Hoblitt and others (1981), consisting of a basal zone made up of a mixture of blast dacite with translocated forest duff, soil, bark, and wood, overlain first by a normally graded, fines-depleted dacite-rich bed with abundant charred wood, then by a bedded well-sorted ash-surge unit.

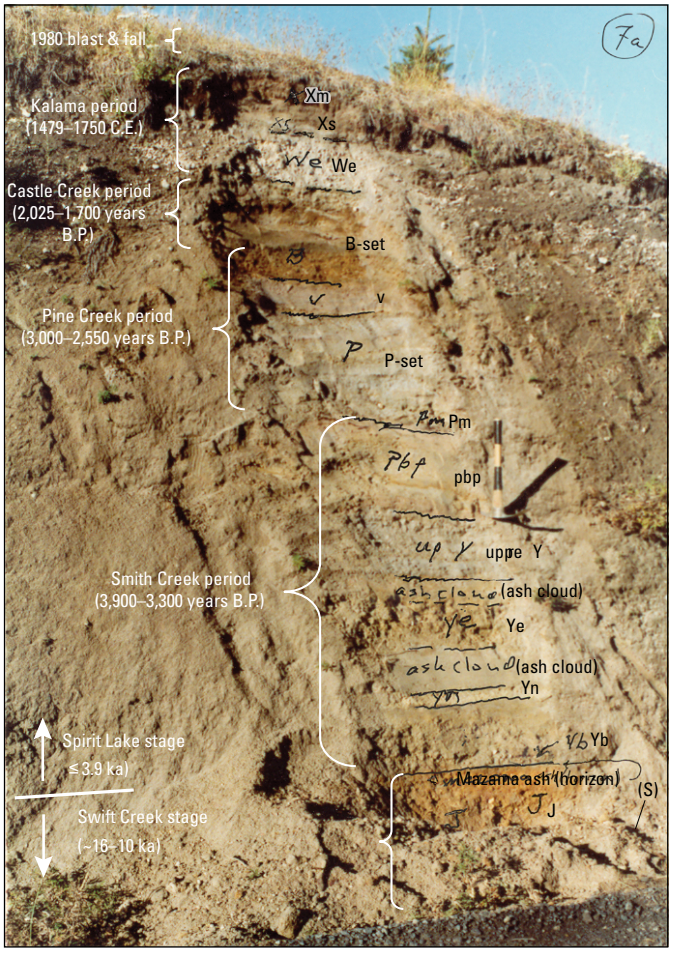

Figure 45. Photograph of tephra section at Stop A-1 taken in 1990. Major eruptive stages and distinct tephra layers of Mullineaux (1986, 1996) are indicated. Stage and period ages have been updated.

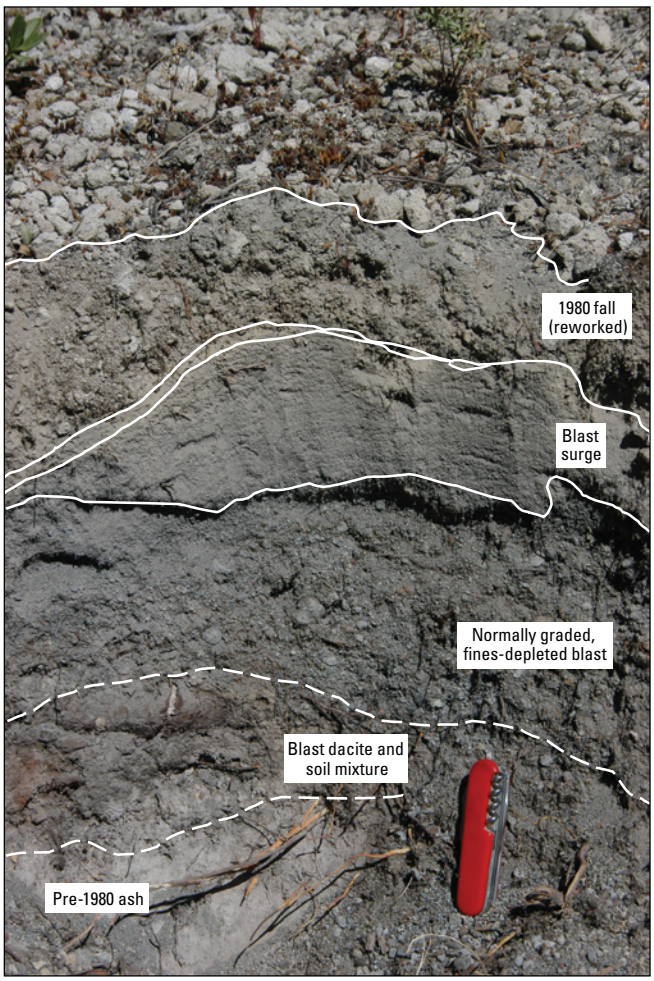

Figure 46. Photograph showing section of 1980 blast deposit at the south end of the roadcut at Stop A-1.

Day 3: Crater Hike

By Heather M. Wright[1] and David R. Sherrod[1]

0.0 Start from Windy Ridge Viewpoint. Restrooms are available.

0.2 Exit the parking lot from the primitive, gated road at the southeast corner. The road has several treacherous areas and may require 4-wheel drive or be impassible by vehicle. The locked gate requires a USFS key or partner key. *Be sure that the lock is fastened such that either padlock will unlock the gate.*

2.1 Stop at the research parking lot located at the base of Windy Ridge and at the trailheads for both the Truman (#207) and Loowit (#216) Trails. Take the upper trail (Loowit) toward Loowit Falls. The trail leads directly across the drainage to the west and climbs the low bluff at the west side of the drainage. The drainage has been intermittently affected by post-1980 lahars, which remobilize rocks from many different eruptive episodes of Mount St. Helens. Common rock types along the trail are illustrated in figure 47. We will continue on the trail to the vicinity of Loowit Falls, with several stops to observe key features en route.

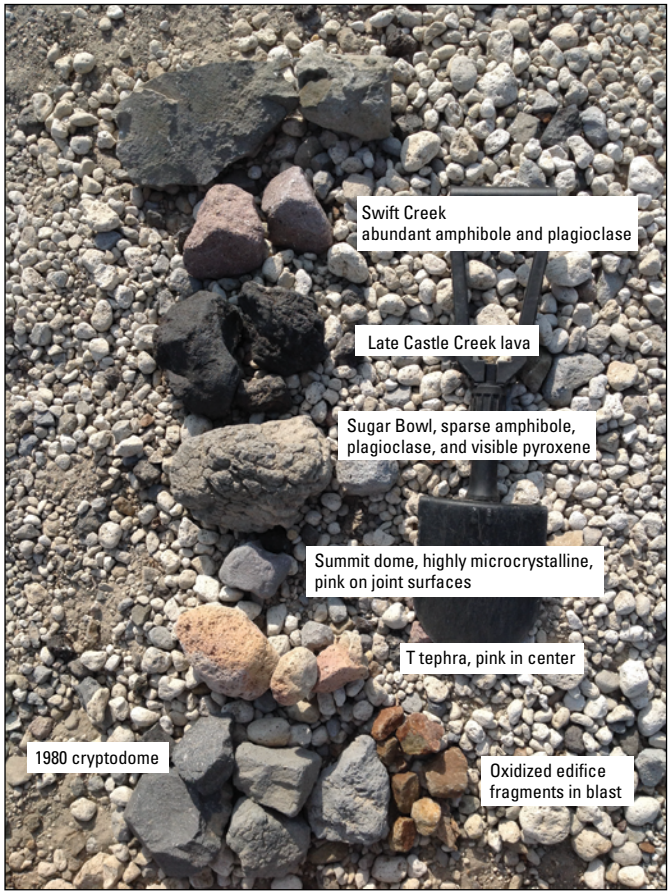

Figure 47. Photograph of common rock types exposed along the trail to the crater of Mount St. Helens. plag, plagioclase.

Most of the current Mount St. Helens edifice is visible as we climb out of the drainage and head toward Loowit Falls. The main edifice is Smith Creek stage or younger (<3,900 years B.P.). The large dome visible from this point is the Sugar Bowl dome, which erupted about 1,050–1,000 years B.P. (table 1; fig. 48).

Continue west on the Loowit Trail.

Stop 18: Layer-T tephra and basalt of the north flank (lat 46°13′38″ N., long 122°09′55″ W.)

The layer-T tephra and basalt of the north flank (near "big spring") are overlain by the basaltic andesite of Nelson Glacier (fig. 49). Prior to 1980, much of this area was covered with mature forest and the detailed stratigraphy was not known. Here, we will continue the discussion of the lava stratigraphy and geochemistry from yesterday.

Stop 19: Loowit Falls viewpoint (lat 46°13′47″ N., long 122°10′35″ W.)

Proceed along the trail passing, "big spring," and stop along the trail at a viewpoint to observe Loowit Falls and the northeast flank of Mount St. Helens and identify major geomorphic and geologic features (fig. 50).

Following the route in figure 51, climb up into the crater breach area through several hummocks of debris-avalanche deposit.

Stop 20: Debris-avalanche hummocks (lat 46°13′24.48″ N., long 122°11′12.24″ W.)

These debris-avalanche hummocks represent large blocks of the former summit area of Mount St. Helens that were transported during the final phase of the 1980 flank-collapse landslide and

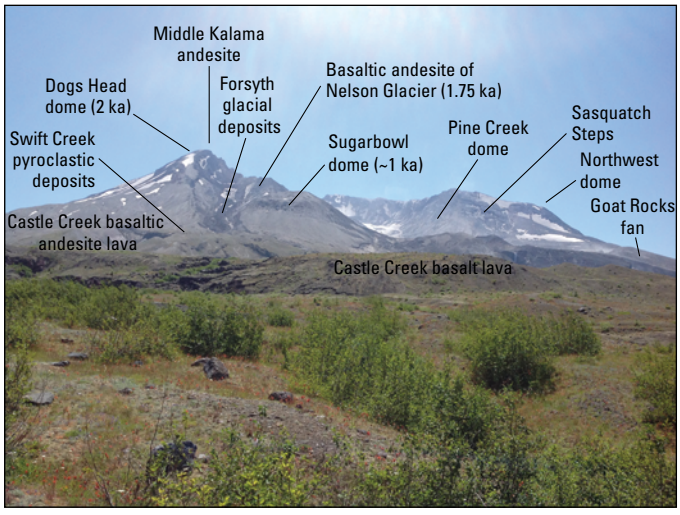

Figure 48. Photograph of Mount St. Helens from the trail to Loowit Falls showing various distinctive rock units. plag, plagioclase.

[1]U.S. Geological Survey.

Figure 49. Photograph taken in 2016 showing small canyon on trail to Loowit Falls that exposes basalt of the north flank overlain by basaltic andesite of Nelson Glacier. Both of these units are in turn overlain by layer-T tephra and 1980 deposits.

stranded here at what is now the crater mouth. The hummocks have a distinctive geomorphic expression, locally forming conical erosional masses and juxtaposing masses of different rock units of varying color and composition against one another. Outcrop areas of the debris avalanche are labeled in figure 51, along with other geologic units.

Stop 21: Lateral flow levees (lat 46°13′09″ N., long 122°11′19″ W.)

Here, we will cross a series of lateral flow levees (fig. 52) in pyroclastic-flow deposits probably formed during the October 17, 1980, eruption. Note the remarkable breadcrust bombs that are present in these pyroclastic-flow deposits.

Stop 22: Crater Glacier view (lat 46°12′52″ N., long 122°11′18″ W.).

Rockfalls and snow avalanches began mantling the crater floor of the newly formed crater soon after eruption in 1980. Crater-floor deposits were rock rich for the first few years, but snow became the dominant component during the past decade or two. Photographs of crevasses from 1996 provide the first evidence that the permanent snowfield was moving, evidence of the existence of Crater Glacier. The crater-floor material had thickened to 200 m by the year 2000, comprising one-third rock debris and two-thirds snow and ice. Growth and advance of a glacier is uncommon today in the Cascade Range, but the unique conditions provided by the May 18, 1980, eruption have been favorable; failure of the summit created a steep, north-facing, high-relief amphitheater, within which snow accumulates from storms and avalanches off the crater rim. The glacier was originally distributed around the south (higher elevation) side of the 1980–1986 dome. The glacier continues to advance northward, owing largely to the growth of an additional dome during the eruption of 2004–2008.

Global positioning system (GPS) receivers on the glacier recorded displacement rates as fast as 2–2.5 m/d in 2005, when the spines of the new dome were displacing the glacier and causing the glacier to thicken, doubling its original thickness. The GPS data show no large diurnal (day-night) differences, nor any seasonal differences. This evidence suggests the glacier does not slide over its bed in response to water flowing along its

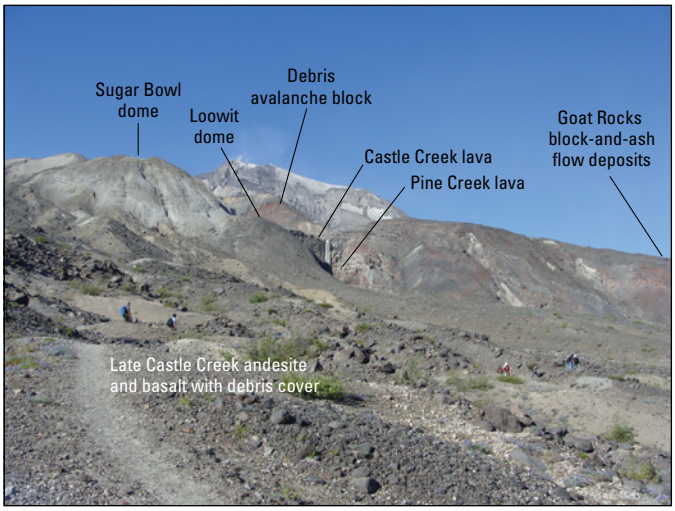

Figure 50. Photograph taken in 2016 showing Loowit Falls (center frame) as seen from the Loowit Trail. Prominent landmarks are labeled.

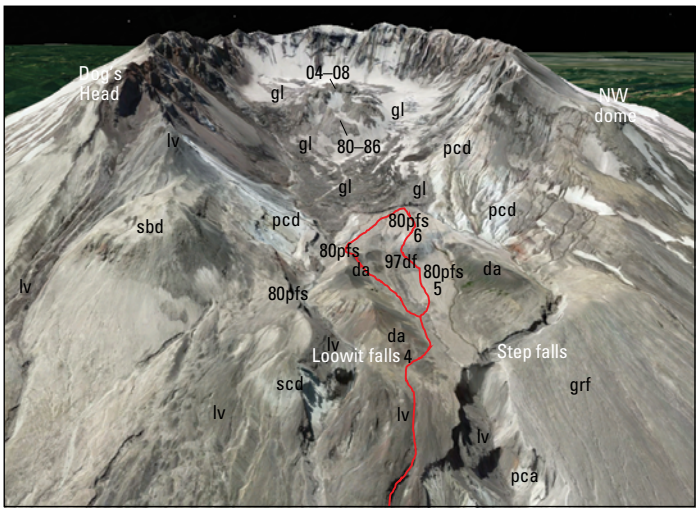

Figure 51. Imagery of Mount St. Helens crater and steps area viewed from the north, showing our climbing route (pale yellow line) and prominent features (imagery from Google Earth, 2016). grf, Goat Rocks fan (block-and-ash flow deposits); sbd, Sugar Bowl dome; pcd, Pine Creek-period domes; pca, Pine Creek-period debris-avalanche deposit; da, 1980 debris-avalanche hummocks; 80–86, 1980–1986 dome lobes; 04–08, 2004–2008 dome spines; 80pfs, 1980 pyroclastic-flow deposits; gl, post-1996 glacier; 97df, 1997 debris-flow deposit.

base. Further, mapping reveals that the snout advanced at rates ranging from 0.2 to 0.6 m/d in the years 2006–2009. While the 2004–2008 dome was growing, the glacier advanced to the north on both sides of the composite (1980–1986 and 2004–2008) lava dome. In February 2008 the west and east arms of the glacier met on the downslope side of the 1980–1986 lava dome, producing a single snout, as seen in figures 51 and 52. Since 2009, the snout advance rate has stabilized at less than 0.1 m/d and in 2011–2012 the front of the glacier advanced into the head of Loowit canyon. The total distance of snout travel between September 2006 and the end of May 2015 is about 750 m. (fig. 53).

Stop 23: Stacked pyroclastic density current deposits (lat 46°12′57″ N., long 122°11′08″ W.)

At this stop, we can see stacked pyroclastic density current deposits from explosive eruptions of 1980. Across the canyon above Loowit Falls, several deposits with coarse-clast-rich tops and fine bases are visible (fig. 54). The pink-topped unit near the top of the sequence is probably the sequence of July 1980 pyroclastic density currents, as these deposits typically display such a pink color. In the canyon wall to the east, we see a Pine Creek-period dacite lava dome that is intruded by Castle Creek-period mafic dikes. The dome rock is intensely shattered, possibly as a result of rapid decompression and shear accompanying unroofing and flank collapse in 1980 or in the Pine Creek period (Reid and others, 2010; Kendrick and others, 2013). Deposits from such Pine Creek-period avalanches (Hausback and Swanson, 1990) are exposed in the floor of Step Creek below Step Falls (fig. 51).

We now reverse our course, climb down from the crater, and follow the trail back to our vehicles and to the campsite for a final evening of rest and relaxation before returning to Portland.

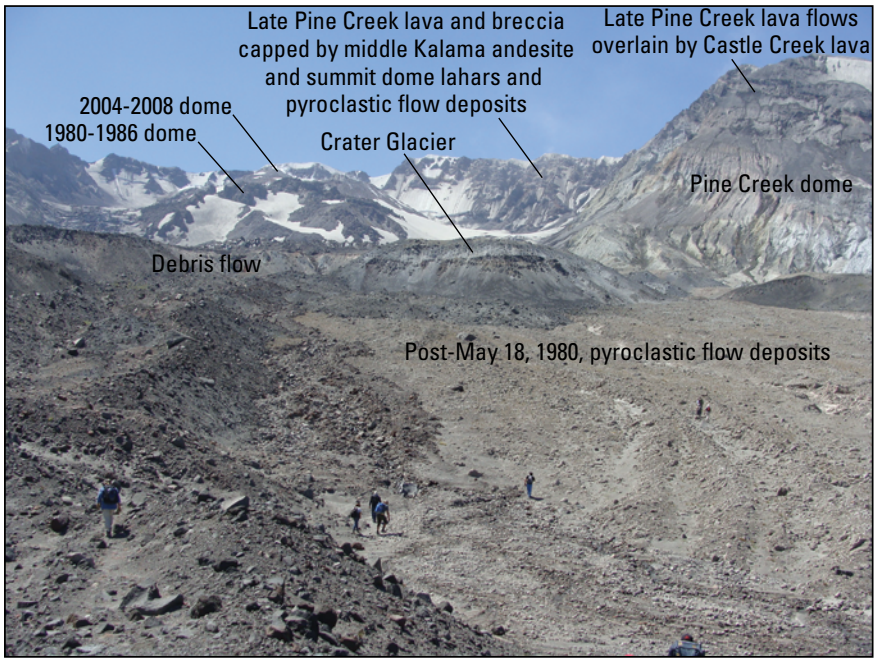

Figure 52. Photograph taken in 2016 looking south into Mount St. Helens crater from the northern breach area.

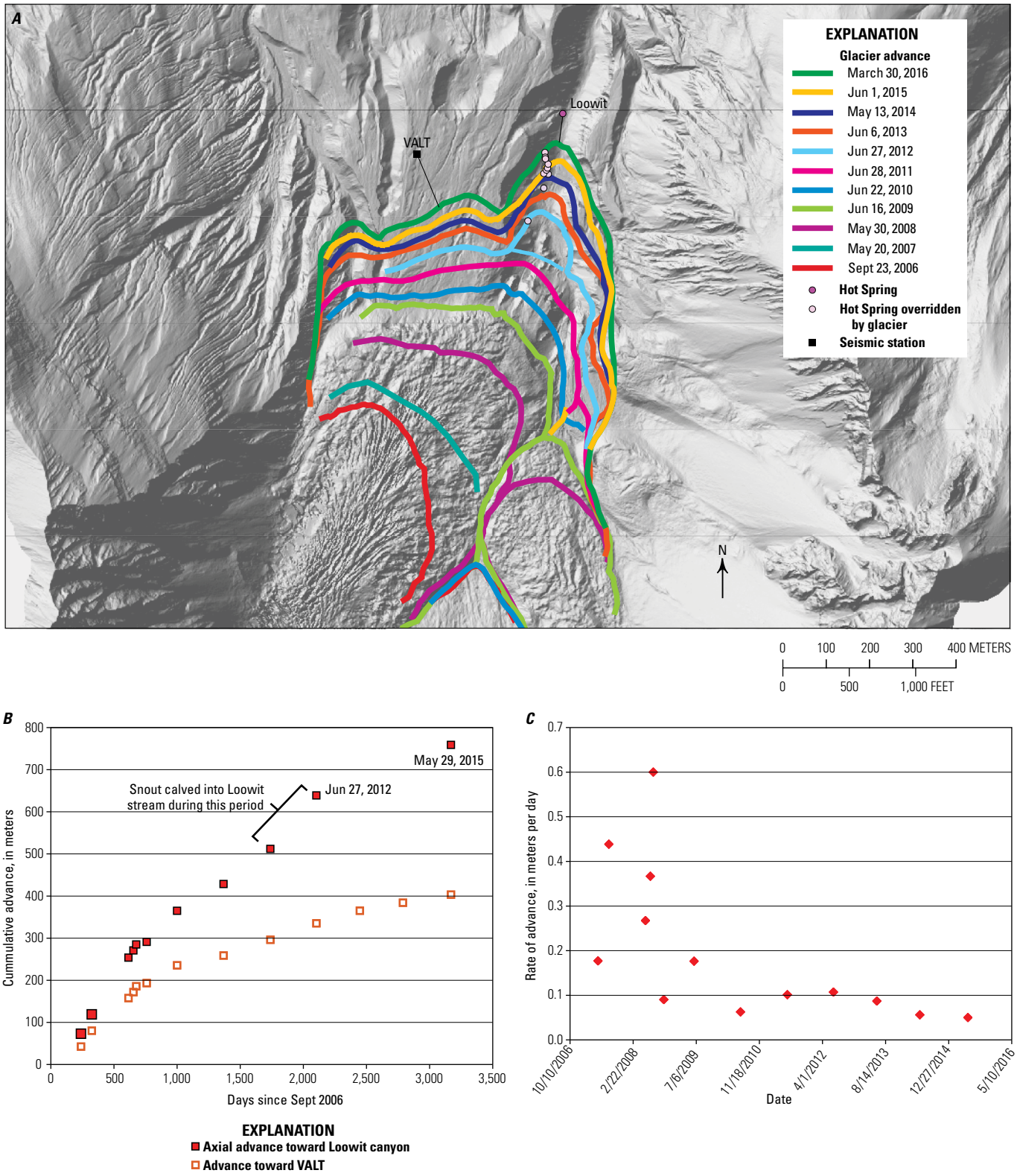

Figure 53. Imagery and plots of Crater Glacier advance. *A*, Aerial image from June 16, 2009, with advance of the Crater Glacier during the period 2006–2016 indicated. *B*, Cumulative northerly advance of the front (snout) of the glacier toward (and into) Loowit canyon and north toward seismic station VALT. *C*, Advance rates of the snout of the glacier during the 2006–2015 period.

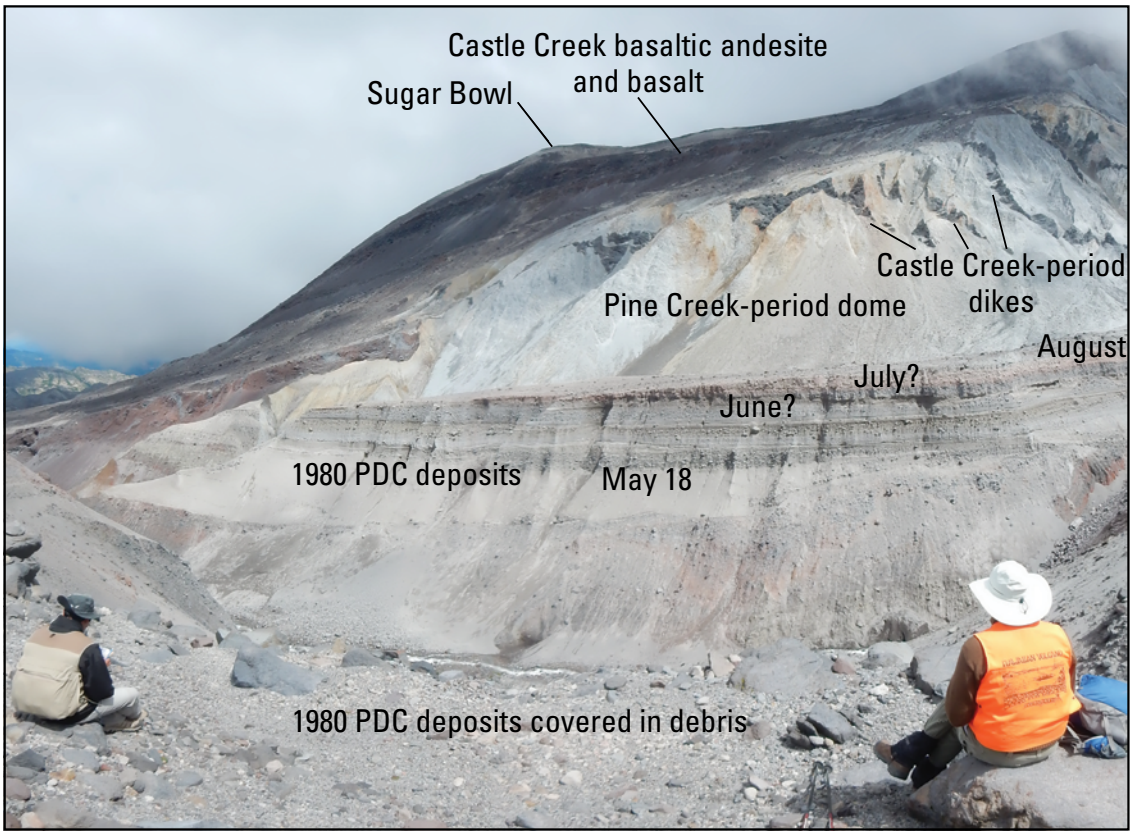

Figure 54. Panorama photograph showing stratigraphic section through 1980 pyroclastic density current (PDC) deposits in the east wall of Loowit canyon. In the background is an intensely shattered Pine Creek-period dome that is cut by mafic dikes of the Castle Creek period.

References Cited

Andrews, B.J., and Gardner, J.E., 2009, Turbulent dynamics of the 18 May 1980 Mount St. Helens eruption column: Geology, v. 37, p. 895–898.

Baker, V.R., and Bunker, R.C., 1985, Cataclysmic Late Pleistocene flooding from glacial Lake Missoula—A review: Quaternary Science Reviews, v. 4, p. 1–41.

Berlo, K., Turner, S., Blundy, J., and Hawksworth, C., 2004, The extent of U-series disequilibria produced during partial melting of the lower crust with implications for the formation of the Mount St. Helens dacites: Contributions to Mineralogy and Petrology, v. 148, p. 122–130.

Blatter, D., Sisson, T., and Hankins, W., 2015, Experimental constraints on the genesis of hydrous arc dacites [abs.]: American Geophysical Union Fall Meeting 2015 Abstracts, abstract no. V31-A-3005.

Blatter, D.L., Sisson, T.W., and Hankins, W.B., 2017, Voluminous arc dacites as amphibole reaction-boundary liquids: Contributions to Mineralogy and Petrology, v. 172, p. 27–54, http://www.dx.doi.org/10.1007/s00410-017-1340-6.

Blundy, J., and Cashman, K., 2001, Ascent-driven crystallization of dacite magmas at Mount St. Helens, 1980–1986: Contributions to Mineralogy and Petrology, v. 140, p. 631–650, http://www.dx.doi.org/10.1007/s004100000219.

Blundy, J., and Cashman, K., 2005, Rapid decompression-driven crystallization recorded by melt inclusions from Mount St. Helens volcano: Geology, v. 33, p. 793–796, http://dx.doi.org/10.1130/G21668.1.

Blundy, J., Cashman, K., and Humphreys, M., 2006, Magma heating by decompression-driven crystallization beneath andesite volcanoes: Nature, v. 443, p. 76–80, http://dx.doi.org/10.1038/nature05100.

Borg, L.E., Clynne, M.A., and Bullen, T.D., 1997, The variable role of slab-derived fluids in the generation of a suite of primitive calc-alkaline lavas from the southernmost Cascades, California: Canadian Mineralogist, v. 35, p. 425–452.

Brugman, M.M., and Post, A., 1981, Effects of volcanism on the glaciers of Mount St. Helens: U.S. Geological Survey Circular 850–D, 11 p.

Carey, S., Gardner, J., and Sigurdsson, H., 1995, The intensity and magnitude of Holocene Plinian eruptions from Mount St. Helens volcano: Journal of Volcanology and Geothermal Research, v. 66, p. 185–202.

Carey, S., Sigurdsson, H., Gardner, J.E., and Criswell, W., 1990, Variations in column height and magma discharge during the May 18, 1980 eruption of Mount St. Helens: Journal of Volcanology and Geothermal Research, v. 43, p. 99–112.

Carroll, K.R., 2009, Interaction of dacitic and basaltic magmas deduced from evolution of phenocrysts and mixing of crystal populations during the Kalama eruptive period, Mount St. Helens: Oregon, Portland State University, Master's thesis, 305 p.

Cashman, K.V., 1988, Crystallization of Mount St. Helens 1980–1986 dacite—A quantitative textural approach: Bulletin of Volcanology, v. 50, p. 194–209.

Cashman, K.V., 1992, Groundmass crystallization of Mount St. Helens dacite, 1980–1986—A tool for interpreting shallow magmatic processes: Contributions to Mineralogy and Petrology, v. 109, p. 431–449.

Cashman, K.V., and Hoblitt, R.P., 2004, Magmatic precursors to the 18 May 1980 eruption of Mount St. Helens, USA: Geology, v. 32, p. 141–144.

Cashman, K.V., and McConnell S.M., 2005, Multiple leves of magma storage during the 1980 summer eruptions of Mount St. Helens, WA: Bulletin of Volcanology, v. 68, p. 57–75, http://dx.doi.org/10.1007/s00445-005-0422-x.

Cashman, K.V., Thornber, C.R., and Pallister, J.S., 2008, From dome to dust—shallow crystallization and fragmentation of conduit magma during the 2003–2008 dome extrusion of Mount St. Helens, Washington, chap. 19 *of* Sherrod, D.R., Scott, W.E., and Stauffer, P.H., eds., A Volcano Rekindled—The Renewed Eruption of Mount St. Helens, 2004–2006: U.S. Geological Survey Professional Paper 1750, p. 387–414, https://pubs.usgs.gov/pp/1750/.

Clague, J.J., Barendregt, R., Enkin, R.J., and Foit, F.F., Jr., 2003, Paleomagnetic and tephra evidence for tens of Missoula floods in southern Washington: Geology, v. 31, p. 247–250.

Claiborne, L.L., Miller, C.F., Flanagan, D.M., Clynne, M.A., and Wooden, J.L., 2010, Zircon reveals protracted magma storage and recycling beneath Mount St. Helens: Geology, v. 38, p. 1011–1014, http://dx.doi.org/10.1130/G31285.1.

Clynne, M.A., Ramsey, D.W., and Wolfe, E.W., 2005, Pre-1980 Eruptive History of Mount St. Helens, Washington: U.S. Geological Survey Fact Sheet 2005–3045, 4 p.

Clynne, M.A., Calvert, A.T., Wolfe, E.W., Evarts, R.C., Fleck, R.J., and Lanphere, M.A., 2008, The Pleistocene eruptive history of Mount St. Helens, Washington, from 300,000 to 12,800 years before present, chap. 28 *of* Sherrod, D.R., Scott, W.E., and Stauffer, P.H., eds., A Volcano Rekindled—The Renewed Eruption of Mount St. Helens, 2004–2006: U.S. Geological Survey Professional Paper 1750, p. 593–627, https://pubs.usgs.gov/pp/1750/.

Cooper, K.M., and Reid, M.R., 2003, Re-examination of crystal ages in recent Mount St. Helens lavas—implications for magma reservoir processes: Earth and Planetary Science Letters, v. 213, p. 149–167.

Crandell, D.R., 1987, Deposits of Pre-1980 pyroclastic flows and lahars from Mount St. Helens Volcano, Washington: U.S. Geological Survey Professional Paper 1444, 91 p.

Crandell, D.R. and Hoblitt, R.P., 1986, Lateral blasts at Mount St. Helens and hazard zonation: Bulletin of Volcanology, v. 48, p. 27–37.

Crandell, D.R., Mullineaux, D.R., Rubin, M., Spiker, E., and Kelley, M.L., 1981, Radiocarbon dates from volcanic deposits at Mount St. Helens, Washington: U.S. Geological Survey Open-file report 81–844, 15 p.

Criswell, C.W., 1987, Chronology and pyroclastic stratigraphy of the May 18, 1980, eruption of Mount St. Helens, Washington: Journal of Geophysical Research, v. 92, no. B10, p. 10237–10266.

Davis, P.T., Barnosky, C.W., and Stuiver, M., 1982, A 20,000 yr record of volcanic ashfalls, Davis Lake, southwestern Washington [abs.]: American Quaternary Association, Biennial Conference, 7th, Seattle, June 28–30, p. 87.

Defant, M.J., and Drummond, M.S., 1993, Mount St. Helens—Potential example of the partial melting of the subducted lithosphere in a volcanic arc: Geology, v. 21, p. 547–550.

Diefenbach, A.K., Crider, J.G., Schilling, S.P., and Dzurisin, D., 2012, Rapid, low-cost photogrammetry to monitor volcanic eruptions—an example from Mount St. Helens, Washington, USA: Bulletin of Volcanology, v. 74, p. 579–587, http://dx.doi.org/10.1007/s00445-011-0548-y.

Endo, E.T., Malone, S.D., Noson, L.L., and Weaver, C.S., 1981, Locations, magnitudes, and statistics of the March 20–May 18 earthquake sequence, *in* Lipman, P.W., and Mullineaux, D.R., eds., The 1980 eruptions of Mount St. Helens, Washington: U.S. Geological Survey Professional Paper 1250, p. 93–107.

Fink, J.H., Malin, M.C., and Anderson, S.W., 1990, Intrusive and extrusive growth of the Mount St. Helens lava dome: Nature, v. 348, p. 435–437.

Fisher, R.V., Glicken, H.X., and Hoblitt, R.P., 1987, May 18, 1980, Mount St. Helens deposits in South Coldwater Creek, Washington: Journal of Geophysical Research, v. 92, no. B10, p. 10267–10283.

Forterre, Y., and Pouliquen, O., 2003, Long-surface-wave instability in dense granular flows: Journal of Fluid Mechanics, v. 486, p. 3640.

Gardner, J.E., Carey, S., Rutherford, M.J., and Sigurdsson, H., 1995, Petrologic diversity in Mt St. Helens dacites during the last 4,000 years—implications for magma mixing: Contributions to Mineralogy and Petrology, v. 119, p. 224–238.

Gaunt, H.E., Bernard, B., Hidalgo, S., Proaño, A., Wright, H., Mothes, P., Criollo, E., and Kueppers, U., 2016, Juvenile magma recognition and eruptive dynamics inferred from the analysis of ash time series—The 2015 reawakening of Cotopaxi volcano: Journal of Volcanology and Geothermal Research, v. 328, p. 134–146, http://dx.doi.org/10.1016/j.jvolgeores.2016.10.013.

Gaunt, H.E., Sammonds, P.R., Meredith, P.G., Smith, R., and Pallister, J.S., 2014, Pathways for degassing during the lava dome eruption of Mount St. Helens 2004–2008: Geology, v. 42 no. 11, p. 947–950, http://dx.doi.org/10.1130/G35940.1.

Geschwind, C.-H., and Rutherford, M.J., 1992, Cummingtonite and the evolution of the Mount St. Helens (Washington) magma system—An experimental study: Geology, v. 20, p. 1011–1014.

Geschwind, C-H., and Rutherford, M.J., 1995, Crystallization of microlites during magma ascent—the fluid mechanics of 1980–1986 eruptions at Mount St. Helens: Bulletin of Volcanology, v. 57, p. 356–370.

Glicken, H., 1998, Rockslide avalanche of May 18, 1980, Mount St. Helens Volcano, Washington: Bulletin of the Geological Survey of Japan, v. 49, p. 55–106.

Greeley, R., and Hyde, J.H., 1972, Lava tubes of the Cave Basalt, Mount St. Helens, Washington: Geological Society of America Bulletin, v. 83, p. 2397–2418.

Hagstrum, J.T., Hoblitt, R.P., Gardner, C.A., and Gray, T.E., 2002, Holocene geomagnetic secular variation recorded by volcanic deposits at Mount St. Helens, Washington: Bulletin of Volcanology, v. 63, p. 545–556, http://dx.doi.org/10.1007/s00445-001-0178-x.

Halliday, A.N., Fallick, A.E., Dickin, A.P., MacKenzie, A.B., Stephens, W.E., and Hildreth, W., 1983, The isotopic and chemical evolution of Mount St. Helens: Earth and Planetary Science Letters, v. 63, p. 241–256.

Harrington, R.M., and Brodsky, E.E., 2007, Volcanic hybrid earthquakes that are brittle-failure events: Geophysical Research Letters, v. 34, 5 p., http://dx.doi.org/10.1029/2006GL028714.

Harris, D.M., Rose, W.I., Jr., Roe, R., and Thompson, M.R., 1981, Radar observations of ash eruptions, *in* Lipman, P.W., and Mullineaux, D.R., eds., The 1980 eruptions of Mount St. Helens, Washington: U.S. Geological Survey Professional Paper 1250, p. 323–333.

Hausback, B.P., 2000, Geologic map of the Sasquatch Steps Area, north flank of Mount St. Helens, Washington: U.S. Geological Survey Map I-2463, scale 1:4,000.

Hausback, B.P., and Swanson, D.A., 1990, Record of prehistoric debris avalanches on the north flank of Mount St. Helens volcano, Washington: Geoscience Canada, v. 17, no. 3, p. 142–145.

Heliker, C., 1984, Inclusions in the 1980–1983 dacite of Mount St. Helens, Washington: Bellingham, Western Washington University, Master's thesis, 185 p.

Heliker, C., 1995, Inclusions in Mount St. Helens dacite erupted from 1980 through 1983: Journal of Volcanology and Geothermal Research, v. 66, p. 115–135.

Hoblitt, R.P., 1986, Observations of the eruptions of July 22 and August 7, 1980, at Mount St. Helens, Washington: U.S. Geological Survey Professional Paper 1335, 44 p.

Hoblitt, R.P., 2000, Was the 18 May 1980 lateral blast at Mt St. Helens the product of two explosions?: Philosophical Transactions of the Royal Society of London, v. 358, p. 1639–1661.

Hoblitt, R.P., Crandell, D.R., and Mullineaux, D.R., 1980, Mount St. Helens eruptive behavior during the past 1,500 years: Geology, v. 8, p. 555–559.

Hoblitt, R.P., Miller, C.D. and Vallance, J.W., 1981, Origin and stratigraphy of the deposit produced by the May 18 directed blast, *in* Lipman, P.W., and Mullineaux, D.R., eds., The 1980 eruptions of Mount St. Helens, Washington: U.S. Geological Survey Professional Paper 1250, p. 401–419.

Hoblitt, R.P., and Harmon, R.S., 1993, Bimodal density distribution of cryptodome dacite from the 1980 eruption of Mount St. Helens, Washington: Bulletin of Volcanology, v. 55, p. 421–437.

Hoblitt, R.P., and Miller, C.D., 1984, Comments and Reply on "Mount St. Helens 1980 and Mount Pelée 1902—Flow or surge?": Geology, v. 12, p. 692–693.

Holasek, R.E., and Self, S., 1995, GOES weather satellite observations and measurements of the May 18, 1980, Mount St. Helens eruption: Journal of Geophysical Research, v. 100, no. B5, p. 8469–8487.

Hopson, C.A., and Melson, W.G., 1990, Compositional trends and eruptive cycles at Mount St. Helens: Geoscience Canada, v. 17, p. 131–141.

Hyde, J.H., 1975, Upper Pleistocene pyroclastic-flow deposits and lahars south of Mount St. Helens volcano, Washington: U.S. Geological Survey Bulletin 1383-B, 20 p.

Janda, R.J., Scott, K.M., Nolan, K.M., and Martinson, H.A., 1981, Lahar movement, effects, and deposits, *in* Lipman, P.W., and Mullineaux, D.R., eds., The 1980 eruptions of Mount St. Helens, Washington: U.S. Geological Survey Professional Paper 1250, p. 461–478.

Johnson, C.G., Kokelaar, B.P., Iverson, R.M., Logan, M., LaHusen, R.G., Gray, J.M.N.T., 2012, Grain-size segregation and levee formation in geophysical mass flows: Journal of Geophysical Research, v. 117, no. F1, 23 p.

Kendrick, J.E., Smith, R., Sammonds, P., Meredith, P.G., Dainty, M., and Pallister, J.S., 2013, The influence of thermal and cyclic stressing on the strength of rocks from Mount St. Helens, Washington: Bulletin of Volcanology, v. 75, 12 p., http://dx.doi.org/10.1007/s00445-013-0728-z.

Kieffer, S.W., 1981, Fluid dynamics of the May 18 blast at Mount St. Helens, *in* Lipman, P.W., and Mullineaux, D.R., eds., The 1980 eruptions of Mount St. Helens, Washington: U.S. Geological Survey Professional Paper 1250, p. 379–400.

Klug, C., and Cashman, K.V., 1994, Vesiculation of May 18, 1980, Mount St. Helens magma: Geology, v. 22, p. 468–472.

Kokelaar, B.P., Graham, R.L., Gray, J.M.N.T, and Vallance, J.W., 2014, Fine-grained linings of leveed channels facilitate runout of granular flows: Earth and Planetary Science Letters, v. 385, p. 172–180.

Kuntz, M.A., Rowley, P.D., and MacLeod, N.S., 1990, Geologic maps of pyroclastic-flow and related deposits of the 1980 eruptions of Mount St. Helens, Washington: U.S. Geological Survey Miscellaneous Investigations Map I-1950, 2 plates, scale 1:2,000.

Layer, P.W. and Gardner, J.E., 2001, Excess argon in Mount St. Helens plagioclase as a recorder of magmatic processes: Geophysical Research Letters, v. 28, p.4279–4282.

Leeman, W.P., Smith, D.R., Hildreth, W., Palacz, Z. and Rogers, N., 1990, Compositional diversity of late Cenozoic basalts in a transect across the southern Washington Cascades: implications for subduction zone magmatism: Journal of Geophysical Research, v. 95, no. B12, p. 19561–19582.

Lees, J.M., 1992, The magma system of Mount St. Helens—non-linear high-resolution P-wave tomography: Journal of Volcanology and Geothermal Research, v. 53, p. 103–116.

Lieuallen, A.E., 2010, Meeting of the magmas—the evolutionary history of the Kalama eruptive period, Mount St. Helens, Washington: Corvallis, Oregon State University, Master's thesis, 298 p.

Lipman, P.W., and Mullineaux, D.R., eds., 1981, The 1980 eruptions of Mount St. Helens, Washington: U.S. Geological Survey Professional Paper 1250, 844 p., 1 pl.

Layer, P.W., and Gardner, J.E., 2001, Excess argon in Mount St. Helens plagioclase as a recorder of magmatic processes: Geophysical Research Letters, v. 28, no. 22, p. 4279–4282.

Lisowski, M., Dzurisin, D., Denlinger, R.P., and Iwatsubo, E.Y., 2008, Analysis of GPS-measured deformation associated with the 2004–2006 dome-building eruption of Mount St. Helens, Washington, chap. 15 *of* Sherrod, D.R., Scott, W.E., and Stauffer, P.H., eds., A Volcano Rekindled—The Renewed Eruption of Mount St. Helens, 2004–2006: U.S. Geological Survey Professional Paper 1750, p. 301–333, https://pubs.usgs.gov/pp/1750/.

Major, J.J., and Scott, K.M., 1988, Volcaniclastic sedimentation in the Lewis River Valley, Mount St. Helens, Washington; processes, extent, and hazards: U.S. Geological Survey Bulletin 1383–D, 38 p., 1 map.

Major, J.J., Pierson, T.C., Dinehart, R.L., and Costa, J.E., 2000, Sediment yield following severe volcanic disturbance—a two-decade perspective from Mount St. Helens: Geology, v. 28, p. 819–822.

Mastin, L.G., Lisowski, M., Roeloffs, E., and Beeler, N., 2009, Improved constraints on the estimated size and volatile content of the Mount St. Helens magma system from the 2004–2008 history of dome growth and deformation: Geophysical Research Letters, v. 36, 4 p., http://dx.doi.org/10.1029/2009GL039863.

Moore, J.G., and Albee, W.C., 1981, Topographic and structural changes, March–July 1980—photogrammetric data, *in* Lipman, P.W., and Mullineaux, D.R., eds., The 1980 eruptions of Mount St. Helens, Washington: U.S. Geological Survey Professional Paper 1250, p. 123–134.

Moore, J.G., and Rice, C.J., 1984, Chronology and character of the May 18, 1980, explosive eruptions of Mount St. Helens, *in* Geophysics Study Committee, Explosive Volcanism—Inception, Evolution, and Hazards: Washington, D.C., National Academy Press, p. 133–142.

Moore, J.G., and Sisson, T.W., 1981, Deposits and effects of the May 18 pyroclastic surge, *in* Lipman, P.W., and Mullineaux, D.R., eds., The 1980 eruptions of Mount St. Helens, Washington: U.S. Geological Survey Professional Paper 1250, p. 421–438.

Moran, S.C., Malone, S.D., Qamar, A.I., Thelen, W.A., Wright, A.K., and Caplan-Auerbach, J., 2008, Seismicity associated with the renewed dome building at Mount St. Helens, 2004–2005, chap. 2 *of* Sherrod, D.R., Scott, W.E., and Stauffer, P.H., eds., A Volcano Rekindled—The Renewed Eruption of Mount St. Helens, 2004–2006: U.S. Geological Survey Professional Paper 1750, p. 27–60, https://pubs.usgs.gov/pp/1750/.

Mullineuax, D.R., 1986, Summary of pre-1980 tephra-fall deposits erupted from Mount St. Helens, Washington State, USA: Bulletin of Volcanology, v. 48, p. 17–26.

Mullineuax, D.R., 1996, Pre-1980 tephra-fall deposits erupted from Mount St. Helens, Washington: U.S. Geological Survey Professional Paper 1563, 99 p.

Newhall, C.G., 2000, Mount St. Helens, master teacher: Science, v. 288, p. 1181–1183.

Pallister, J.S., Cashman, K.V., Hagstrum, J.T., Beeler, N.M., Moran, S.C., and Denlinger, R.P., 2013, Faulting within the Mount St. Helens conduit and implications for volcanic earthquakes: Geological Society of America Bulletin, v. 125, p. 359–376.

Pallister, J.S., Heliker, C., and Hoblitt, R.P., 1991, Glimpses of the active pluton below Mount St. Helens [abs.]: Eos (American Geophysical Union Transactions), v.72, no. 44, supp., p. 576.

Pallister, J.S., and Hoblitt, R.P., 1985, Magma mixing at Mount St. Helens [abs.]: Eos (American Geophysical Union Transactions), v. 66, p. 1111.

Pallister, J.S., Hoblitt, R.P., Crandell, D.R., and Mullineaux, D.R., 1992, Mount St. Helens a decade after the 1980 eruptions—magmatic models, chemical cycles, and a revised hazards assessment: Bulletin of Volcanology, v. 54, p. 126–146.

Pallister, J.S., Thornber, C.R., Cashman, K.V., Clynne, M.A., Lowers, H.A., Mandeville, C.W., Brownfield, I.K., and Meeker, G.P., 2008: Petrology of the 2004–2006 Mount St. Helens lava dome—Implications for magmatic plumbing and eruption triggering, chap. 30 *of* Sherrod, D.R., Scott, W.E., and Stauffer, P.H., eds., A Volcano Rekindled—The Renewed Eruption of Mount St. Helens, 2004–2006: U.S. Geological Survey Professional Paper 1750, p. 648–702, https://pubs.usgs.gov/pp/1750/.

Pierson, T.C., 1985, Initiation and flow behavior of the 1980 Pine Creek and Muddy river lahars, Mount St. Helens, Washington: Geological Society of America Bulletin, v. 96, p. 1056–1069.

Porter, S.C., Pierce, K.L., and Hamilton, T.D., 1983, Late Wisconsin mountain glaciation in the western United States, *in* Porter, S.C., ed., Late Quaternary Environments of the United States—Volume 1, The Late Pleistocene: Minneapolis, University of Minnesota Press, p. 71–111.

Rea, J., Wallace, P.J., and Clynne, M.A., 2012, Pre-eruptive volatile content of mafic magma from the 2.0–1.7 ka Castle Creek eruptive period, Mount St. Helens [Abs.]: American Geophysical Union Fall Meeting 2012 Abstracts, abstract no. V53C-2853, available at http://abstractsearch.agu.org/meetings/2012/FM/V53C-2853.html.

Reid, M.E., Keith, T.E.C., Kayen, R.E., Iverson, N.R., Iverson, R.M., and Brien, D.L., 2010, Volcano collapse promoted by progressive strength reduction—new data from Mount St. Helens: Bulletin of Volcanology, v. 72, p.761–766, http://dx.doi.org/10.1007/s00445-010-0377-4.

Riker, J.M., Blundy, J.D., Rust, A.C., Botcharnikov, R.E., and Humphries, M.C.S., 2015, Experimental phase equilibria of a Mount St. Helens rhyodacite—a framework for interpreting crystallization paths in degassing silicic magmas: Contributions to Mineralogy and Petrology, v. 170, no. 6, 22 p. http://dx.doi.org/10.1007/s00410-015-1160-5.

Rowley, P.D., Kuntz, M.A., and Macleod, N.S., 1981, Pyroclastic flow deposits, *in* Lipman, P.W., and Mullineaux, D.R., eds., The 1980 eruptions of Mount St. Helens, Washington: U.S. Geological Survey Professional Paper 1250, p. 489–512

Rutherford, M.J., and Devine, J.D., 1988, The May 18, 1980, Eruption of Mount St. Helens—3. Stability and chemistry of amphibole in the magma chamber: Journal of Geophysical Research, v. 93, no. B10, p. 11949–11959.

Rutherford, M.J., and Devine, J.D., III, 2008, Magmatic conditions and processes in the storage zone of the 2004–2006 Mount St. Helens dacite, chap. 31 *of* Sherrod, D.R., Scott, W.E., and Stauffer, P.H., eds., A Volcano Rekindled—The Renewed Eruption of Mount St. Helens, 2004–2006: U.S. Geological Survey Professional Paper 1750, p. 703–725, https://pubs.usgs.gov/pp/1750/.

Rutherford, M.J., and Hill, P.H., 1993, Magma ascent rates from amphibole breakdown—An experimental study applied to the 1980–1986 Mount St. Helens amphibole: Journal of Geophysical Research, v. 98, no. B11, p. 19667–19685.

Rutherford, M.J., Sigurdsson, S., Carey, S., and Davis, A., 1985, The May 18, 1980, Eruption of Mount St. Helens—1. Melt composition and experimental phase equilibria: Journal of Geophysical Research, v. 90, no. B4, p. 2929–2947.

Scandone, R., and Malone, S.D., 1985, Magma supply, magma discharge and readjustment of the feeding system of Mount St. Helens during 1980: Journal of Volcanology and Geothermal Research, v. 23, p. 239–262.

Scandone, R., Cashman, K.V., Malone, S.D., 2007, Magma supply, magma ascent and the style of volcaanic eruptions: Earth and Planetary Science Letters, v. 253, no. 3, p. 513–529.

Schilling, S.P., Carrara, P.E., Thompson, R.A., and Iwatsubo, E.Y., 2004, Posteruption glacier development within the crater of Mount St. Helens, Washington, USA: Quaternary Research, v. 61, p. 325–329.

Schilling, S.P., Thompson, R.A., Messerich, J.A., and Iwatsubo, E.Y., 2008, Use of digital aerophotogrammetry to determine rates of lava dome growth, Mount St. Helens, Washington 2004–2005, chap. 8 *of* Sherrod, D.R., Scott, W.E., and Stauffer, P.H., eds., A Volcano Rekindled—The Renewed Eruption of Mount St. Helens, 2004–2006: U.S. Geological Survey Professional Paper 1750, p. 145–167, https://pubs.usgs.gov/pp/1750/.

Scott, K.M., 1988a, Origins, behavior, and sedimentology of lahars and lahar-runout flows in the Toutle-Cowlitz River system: U.S. Geological Survey Professional Paper 1447–A, 74 p.

Scott, K.M., 1988b, Origin, behavior, and sedimentology of prehistoric catastrophic lahars at Mount St. Helens, Washington: Geological Society of America Special Paper 229, p. 23–36.

Scott, W.E., Sherrod, D.R., and Gardner, C.A., 2008, Overview of the 2004 to 2006, and continuing, eruption of Mount St. Helens, Washington, chap. 1 *of* Sherrod, D.R., Scott, W.E., and Stauffer, P.H., eds., A Volcano Rekindled—The Renewed Eruption of Mount St. Helens, 2004–2006: U.S. Geological Survey Professional Paper 1750, p. 3–22, https://pubs.usgs.gov/pp/1750/.

Sherrod, D.R., Scott, W.E., and Stauffer, P.H., eds., 2008, A Volcano Rekindled—The Renewed Eruption of Mount St. Helens, 2004–2006: U.S. Geological Survey Professional Paper 1750, 856 p., https://pubs.usgs.gov/pp/1750/.

Sisson, T.W., 1995, Blast ashfall of May 18, 1980 at Mount St. Helens, Washington: Journal of Volcanology and Geothermal Research, v. 66, p. 203–216.

Smith, D.R., and Leeman, W.P., 1987, Petrogenesis of Mount St. Helens dacitic magmas: Journal of Geophysical Research, v. 92, no. B10, p. 10313–10334.

Smith, D., and Leeman, W.P., 1993, The origin of Mount St. Helens andesites: Journal of Volcanology and Geothermal Research, v. 55, p. 271–303.

Sparks, R.S.J., Moore, J.G., and Rice, C.J., 1986, The initial giant umbrella cloud of the 18 May, 1980, explosive eruption of Mount St. Helens: Journal of Volcanology and Geothermal Research, v. 28, p. 257–274.

Sun, S.-S., and McDonough, W.F., 1989, Chemical and isotopic systematics of oceanic basalts—implications for mantle composition and processes, *in* Saunders, A.D., and Norry, M.J., eds., Magmatism in the Ocean Basins: Geological Society Special Publication No. 42, p. 313–345.

Swanson, D.A., and Holcomb, R.T., 1990, Regularities in growth of the Mount St. Helens dacite dome, 1980–1986, *in* Fink, J.H., ed., Lava flows and domes. Springer Berlin Heidelberg, p. 3–24.

Swanson, D.A., Dzurisin, D., Holcomb, R.T., Iwatsubo, E.Y., Chadwick, W.W., Jr., Casadevall, T.J., Ewert, J.W. and Heliker, C.C., 1987, Growth of the lava dome at Mount St. Helens, Washington, (USA), 1981–1983, Geological Society of America Special Paper 212, 16 p.

Vallance, J.W., Schneider, D.J., and Schilling, S.P., 2008, Growth of the 2004–2006 lava-dome complex at Mount St. Helens, Washington, chap. 9 *of* Sherrod, D.R., Scott, W.E., and Stauffer, P.H., eds., A Volcano Rekindled—The Renewed Eruption of Mount St. Helens, 2004–2006: U.S. Geological Survey Professional Paper 1750, p. 169–208.

Van Eaton, A.R., Muirhead, J.D., Wilson, C.J.N., and Cimarelli, C., 2012, Growth of volcanic ash aggregates in the presence of liquid water and ice—an experimental approach: Bulletin of Volcanology, v. 74, no. 9, p. 1963–1984.

Voight, B., 1981, Time scale for the first moments of the May 18 eruption, *in* Lipman, P.W., and Mullineaux, D.R., eds., The 1980 eruptions of Mount St. Helens, Washington: U.S. Geological Survey Professional Paper 1250, p. 69–86.

Voight, B., Glicken, H., Janda, R.J., and Douglass, P.M, 1981, Catastrophic rockslide avalanche of May 18, *in* Lipman, P.W., and Mullineaux, D.R., eds., The 1980 eruptions of Mount St. Helens, Washington: U.S. Geological Survey Professional Paper 1250, p. 347–377.

Volpe, A.M., and Hammond, P.E., 1991, ^{238}U- ^{230}Th- ^{226}Ra disequilibria in young Mount St. Helens rocks—time constraint for magma formation and crystallization: Earth and Planetary Science Letters, v. 107, p. 475–486.

Waite, G.P., Chouet, B.A., and Dawson, P.B., 2008, Eruption dynamics at Mount St. Helens imaged from broadband seismic waveforms—Interaction of the shallow magmatic and hydrothermal systems: Journal of Geophysical Research, v. 113, no. B2, 22 p., http://dx.doi.org/10.1029/2007JB005259.

Waite, G.P., and Moran, S.M, 2009, VP Structure of Mount St. Helens, Washington, USA, imaged with local earthquake tomography: Journal of Volcanology and Geothermal Research, v. 192, p. 113–122.

Waitt, R.B., Jr., 1981, Devastating pyroclastic density flow and attendant air fall of May 18—Stratigraphy and sedimentology of deposits, *in* Lipman, P.W., and Mullineaux, D.R., eds., The 1980 eruptions of Mount St. Helens, Washington: U.S. Geological Survey Professional Paper 1250, p. 439–458.

Waitt, R.B., Jr., 1985, Case for periodic, colossal jökulhlaups from Pleistocene glacial Lake Missoula: Geological Society of America Bulletin, v. 96, p. 1271–1286.

Waitt, R., 2015, In the path of destruction—Eyewitness chronicles of Mount St. Helens: Pullman, Wash., Washington State University Press, 384 p.

Waitt, R.B., Pierson, T.C., MacLeod, N.S., Janda, R.J., Voight, B. and Holcomb, R.T., 1983, Eruption-triggered avalanche, flood, and lahar at Mount St. Helens—effects of winter snowpack: Science, v. 221, p. 1394-1397.

Wanke, M., Bachmann, O., Ellis, B.S., Guillong, M., Clynne, M.A., and Pallister, J.S., 2016, Insights into the Mount St. Helens magma plumbing system from coarse-grained, crystal-rich enclaves: American Geophysical Union Fall Meeting 2016 Abstracts, abstract no. V33B-3127, available at https://agu.confex.com/agu/fm16/meetingapp.cgi/Paper/173787.

Weaver, C.S., Grant, W.C., and Shemeta, J.E., 1987, Local crustal extension at Mount St. Helens, Washington: Journal of Geophysical Research, v. 92, no. B10, p. 10170–10178.

Wells, R.E., 1990, Paleomagnetic rotations and the Cenozoic tectonics of the Cascade Arc, Washington, Oregon, and California, Journal of Geophysical Research: Solid Earth, v. 95, no. B12, p. 19409–19417.

Wells, R.E., Weaver, C.S., and Blakely, R.J., 1998, Fore-arc migration in Cascadia and its neotectonic significance: Geology, v. 26, p. 759–762.

Williams, D.L., Abrams, G., Finn, C., Dzurisin, D., Johnson, D.J., and Denlinger, R., 1987, Evidence from gravity data for an intrusive complex beneath Mount St. Helens: Journal of Geophysical Research, v. 92, no. B10, p. 10207–10222.

Wright, H.M., Cashman, K.V., Rosi, M., and Cioni, R., 2007, Breadcrust bombs as indicators of Vulcanian eruption dynamics at Guagua Pichincha volcano, Ecuador: Bulletin of Volcanology, v. 69, p. 281–300.

Yamaguchi, D.K., 1983, New tree-ring dates for Recent eruptions of Mount St. Helens: Quaternary Research, v. 20, p. 246–250.

Yamaguchi, D.K., 1985, Tree-ring evidence for a two-year interval between recent prehistoric explosive eruptions of Mount St. Helens: Geology, v. 13, p. 554–557.

Yamaguchi, D.K., and Hoblitt, R.P., 1995, Tree-ring dating of pre-1980 flowage deposits at Mount St. Helens: Geological Society of America Bulletin, v. 107, p. 1077–1093.

Yamaguchi, D.K., Hoblitt, R.P., and Lawrence, D.B., 1990, A new tree-ring date for the “floating island” lava flow, Mount St. Helens, Washington: Bulletin of Volcanology, v. 52, p. 545–550.

Menlo Park Publishing Service Center, California
Manuscript approved June 6, 2017
Edited by Regan Austin
Illustrations by Linda Masonic
Layout by Cory Hurd

ISSN 2328-0328 (online)
https://doi.org/10.3133/sir20175022D